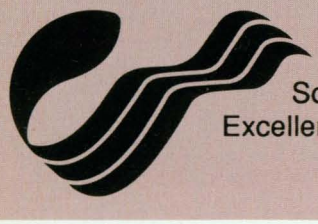

Scientific Excellence • Resource Protection & Conservation • Benefits for Canadians
Excellence scientifique • Protection et conservation des ressources • Bénéfices aux Canadiens

PERD Workshop on Coastal Current Models for Continental Shelves, Kelowna, B.C. June 1-2 1995.

W.R. Crawford and M.G.G. Foreman, Editors

Department of Fisheries and Oceans
Institute of Ocean Sciences
P. O. Box 6000
Sidney, British Columbia, V8L 4B2

1995

Canadian Technical Report of Hydrography and Ocean Sciences 169

Fisheries and Oceans Pêches et Océans

Canada

Canadian Technical Report of Hydrography and Ocean Sciences

Technical reports contain scientific and technical information that contributes to existing knowledge but which is not normally appropriate for primary literature. The subject matter is related generally to programs and interests of the Ocean Science and Surveys (OSS) sector of the Department of Fisheries and Oceans.

Technical reports may be cited as full publications. The correct citation appears above the abstract of each report. Each report is abstracted in *Aquatic Sciences and Fisheries Abstracts* and indexed in the Department's annual index to scientific and technical publications.

Technical reports are produced regionally but are numbered nationally. Requests for individual reports will be filled by the issuing establishment listed on the front cover and title page. Out of stock reports will be supplied for a fee by commercial agents.

Regional and headquarters establishments of Ocean Science and Surveys ceased publication of their various report series as of December 1981. A complete listing of these publications is published in the *Canadian Journal of Fisheries and Aquatic Sciences*, Volume 39: Index to Publications 1982. The current series, which begins with report number 1, was initiated in January 1982.

Rapport technique canadien sur l'hydrographie et les sciences océaniques

Les rapports techniques contiennent des renseignements scientifiques et techniques qui constituent une contribution aux connaissances actuelles, mais qui ne sont pas normalement appropriés pour la publication dans un journal scientifique. Le sujet est généralement lié aux programmes et intérêts du service des Sciences et levés océaniques (SLO) du ministère des Pêches et des Océans.

Les rapports techniques peuvent être cités comme des publications complètes. Le titre exact paraît au-dessus du résumé de chaque rapport. Les rapports techniques sont résumés dans la revue *Résumés des sciences aquatiques et halieutiques*, et ils sont classés dans l'index annuel des publications scientifiques et techniques du Ministère.

Les rapports techniques sont produits à l'échelon régional, mais numérotés à l'échelon national. Les demandes de rapports seront satisfaites par l'établissement auteur dont le nom figure sur la couverture et la page du titre. Les rapports épuisés seront fournis contre rétribution par des agents commerciaux.

Les établissements des Sciences et levés océaniques dans les régions et à l'administration centrale ont cessé de publier leurs diverses séries de rapports en décembre 1981. Une liste complète de ces publications figure dans le volume 39, Index des publications 1982 du *Journal canadien des sciences halieutiques et aquatiques*. La série actuelle a commencé avec la publication du rapport numéro 1 en janvier 1982.

Canadian Technical Report of
Hydrography and Ocean Sciences No. 169

1995

PERD Workshop on Coastal Current Models for Continental Shelves Kelowna, B.C. June 1–2 1995

Department of Fisheries and Oceans
Institute of Ocean Sciences
P.O. Box 6000
Sidney, B.C. V8L 4B2

Cat. No. FS 97-18/169E ISSN 0711-6764

Correct citation for this publication:

Crawford, W.R. and M.G.G. Foreman, eds. 1995. PERD Workshop on Coastal Current Models for Continental Shelves. Can. Tech. Rep. Hydrog. Ocean Sci. No. 169: 85 pp.

CONTENTS

Preface

We thank the Panel for Energy Research and Development (PERD), Dick Stoddart of the Department of Fisheries and Oceans (DFO), and Duncan Hardie of Environment Canada for the funding to organize the workshop whose extended abstracts are included in this volume.

This workshop brought together PERD-funded scientists who are applying numerical models of coastal currents to a variety of applications for the oil and gas industry: ice dynamics, wave forecasting, oil spills, and even search and rescue. The workshop included scientists studying any aspect of the shelf circulation and was held as a session at the Annual Congress of the Canadian Meteorological and Oceanographic Society, in order to encourage participation from the entire oceanographic community. For two days in sunny Kelowna, British Columbia, in June 1995, we discussed the flow of normally cold and ice-covered seawater over various Canadian continental shelves, including the St. Lawrence Estuary and the Strait of Georgia.

Our invited speakers, Keith Thompson and Dan Lynch, described two very distinct approaches. We wish we had allotted them more time to present their ideas. Keith Thompson has improved the accuracy of his current predictions on the Scotian Shelf by using near-real-time sea level data to modify the inflow currents at the open boundary of his barotropic, finite-difference, time stepping model. Dan Lynch has developed a fully non-linear, fully baroclinic, time stepping, finite-element model to simulate currents in the Gulf of Maine and on Georges Bank. It is a more sophisticated model, in that it includes more physical processes directly; however, it is more expensive to run, and has not yet been adapted to include near-real-time oceanographic data. Within our community there is a need for both models. Indeed, a combination of the two approaches, namely a baroclinic finite-element model to define a generic background circulation, and a coarser barotropic model to predict storm-driven currents, is already under development on both the Pacific and Atlantic coasts.

The study of coastal currents brings together two completely different processes: tides and turbulence. The prediction of tidal elevations and barotropic tidal currents is one of the most successful applications of computer modelling to oceanography. Tides are regular, and the motion of tides through coastal oceans can be simulated very accurately today, on even small computers. Turbulence is something else! By its nature it is chaotic. Yet even in this chaos there is just enough order to entice us to simulate and predict. Among the scientific computer-intensive activities today, some of the largest computers are devoted to simulating stratified turbulent flows around complex topography. Within the coastal waters of Canada, we have all combinations of tides and turbulence. The highest tides are in the Bay of Fundy while the fastest tidal currents are in coastal British Columbia. An amazing combination of tides, internal waves, and turbulence is found in the St. Lawrence Estuary. The combination of tidal flow and turbulence in Juan de Fuca Strait sets up a two-layer flow that exceeds the Amazon River in volume. The ice dynamics on the Labrador Shelf can sometimes defy any predictive scheme, and yet at other times appear quite regular.

Our challenge is not just to use our skills to probe the science of these complexities. We also have a responsibility to explain our findings to the larger community of engineers and navigators, so that they can appreciate why it is that we can provide accurate predictions (a) everywhere some of the time, (b) somewhere all of the time, but not (c) everywhere all of the time.

W.R. Crawford,
M.G.G. Foreman,

DFO, Institute of Ocean Sciences,
Sidney, B.C.
December 1995

Abstract

Crawford, W.R. and M.G.G. Foreman, eds. 1995. Proceedings of Workshop on Coastal Current Models for Continental Shelves. Can. Tech. Rep. Hydrogr. Ocean Sciences No. 169: 85 pp.

The Panel on Energy Research and Development (PERD)-sponsored Workshop was held on June 1 and 2, 1995 within the Annual Congress of the Canadian Meteorological and Oceanographic Society. The workshop brought together Canadian and non-Canadian scientists undertaking research into the modelling of ocean currents on Canadian continental shelves. Much of the workshop was devoted to the presentation of these studies by the scientists, and discussion of the methods and results. Extended abstracts of these presentations are reported here.

Within these twenty abstracts are descriptions of current models of the Atlantic and Pacific coasts, the Labrador Sea, the Strait of Georgia, Hudson and James Bays, and portions of the Canadian Arctic Archipeligo. Details of flow along cross-shelf canyons, around isolated seamounts, and of internal wave representations are also presented. One paper describes the application of turbulence closure methods to numerical models. Finite-difference models, finite-element models and data assimilation were applied to the prediction of coastal currents. As well, several studies investigated the best representation of open boundary conditions, and surface forcing, and the application of acoustic Doppler measurements to predictions of currents.

Keywords: ocean currents, coastal oceanography, ocean modelling.

Sommaire

Crawford, W.R. and M.G.G. Foreman, eds. 1995. Proceedings of Workshop on Coastal Current Models for Continental Shelves. Can. Tech. Rep. Hydrogr. Ocean Sciences No. 169: 85 pp.

L'atelier sur l'initiative du Comité de la recherche sur l'énergie et du développement (PERD), fut tenu le 1 et le 2 juin, 1995, sous les auspices du Congrès annuel de la Société canadienne de météorologie et d'océanographie.

L'atelier mit en contact des scientifiques canadiens et non-canadiens étudiant les modèles de courants océaniques sur les plateaux continentaux canadiens. Une bonne partie de l'atelier fut consacrée à la présentation de ces recherches par les scientifiques, et au débat sur les méthodes et sur les résultats. Des résumés détaillés des présentations sont inclus ci-après.

Les vingt résumés contiennent des descriptions des modèles de courants au large des côtes du Pacifique et de l'Alantique, dans la mer du Labrador, dans le détroit de Georgia, dans les baies d'Hudson et James, et dans des parties de l'Archipel arctique canadien. Des détails concernant les courants qui longent les cañons à travers le plateau continental et des courants qui tournent autour de monts soumarins isolés sont présentés, ainsi que sur les ondes de gravité internes. Un article décrit l'application des méthodes de fermeture de turbulence dans les modèles numériques.

Des modèles mathématiques aux différences finies et aux éléments finis et l'assimilation des données furent appliqués à la prédiction des courants côtiers. Aussi, plusieurs études examinèrent la représentation des conditions aux frontières ouvertes, des forces à la surface, et de l'application des mesures acoustiques Doppler à la prédiction des courants.

Mot-clés: courants océaniques, océanographie côtière, modèles océaniques.

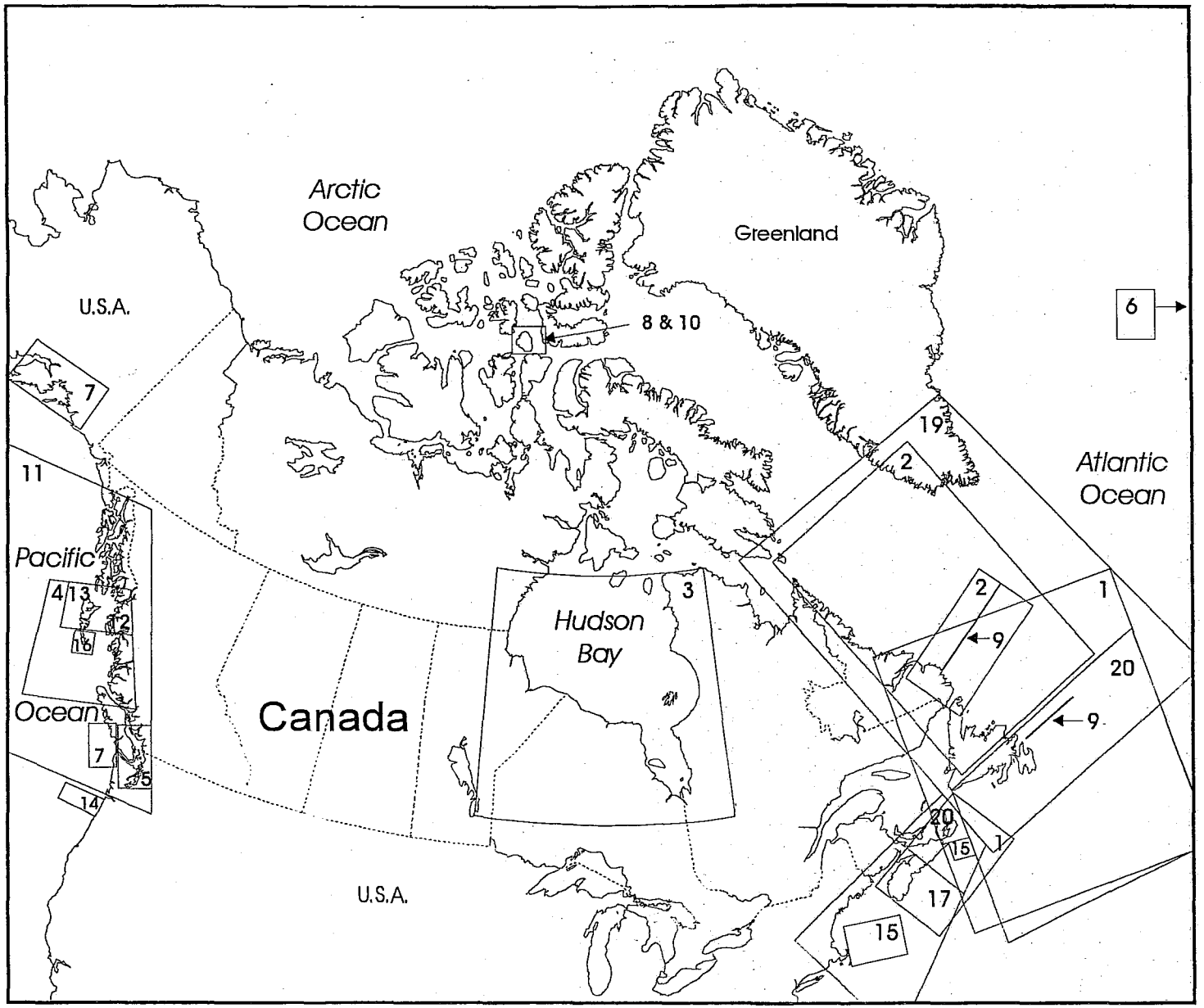
Arctic Ocean
Greenland
U.S.A.
8 & 10
6
7
19
2
11
Atlantic Ocean
Pacific
4
13
12
16
3
Hudson Bay
2
1
9
20
Ocean
Canada
7
5
9
14
20
15
1
U.S.A.
17
15

Study Areas

Towards an Operational Model of the Circulation on the Eastern Canadian Continental Shelf

Keith R. Thompson, Jinyu Sheng, Michael G. Dowd and Joško Bobanović
Department of Oceanography
Dalhousie University
Halifax, Nova Scotia
Canada, B3H 4J1

The continental shelf off Canada's east coast is wide and rugged with numerous deep basins and banks. Beyond the shelf break are two major western boundary currents: the Gulf Stream and the Labrador Current. It is therefore perhaps not surprising that the subtidal circulation on the middle and outer shelf is complex in comparison to other North American shelves. In particular, typical horizontal scales are less than 35 km, in contrast, for example, to the Mid-Atlantic Bight where scales can exceed 600 km.

The difficulty in modelling the circulation has led us to the use of inverse methods to infer open boundary conditions for limited area models. In the talk I will (i) describe how we infer open bounday conditions using data assimilation (ii) assess predictive skill, an important issue given the model is in a sense driven by the available observations (iii) discuss what can, and what cannot, be inferred about circulation from coastal sea-level, and (iv) how the circulation models may be improved.

(i) To infer open boundary conditions we first define a cost function, J, which is essentially the mean square difference between the observations and model predictions. It can also include regularization terms that penalize, for example, total kinetic energy and enstrophy. The next step is to develop a scheme for minimizing J with respect to quantities that are considered adjustable i.e. the controls. We take the flows through the open boundaries as controls and use an adjoint model to calculate the gradient of J with respect to them. A conventional numerical algorithm (linear conjugate gradients in our case) is then used to minimize J. We have used a simplified version of this approach to infer the barotropic component of the seasonal circulation on the Newfoundland Shelf and Grand Banks as shown in Figure 1.

We have used a similar assimilation scheme on the Scotian Shelf to infer the time-varying open boundary conditions in the so-called "meteorological band". To illustrate we show in Figure 2 a test of the assimilation method during the winter of 1985-6 using data collected during the Canadian Atlantic Storms Program (CASP). The model is initially forced in non-assimilation mode by local wind stress and coastal sea-level from Louisbourg on the eastern end of the shelf. (It provides the time-varying open boundary condition at the eastern end of the model domain.) It captures the variability quite well at the current meter shown. We then assimilate coastal sea-level and currents from several locations. The improvement in predicted currents at the validation site (data were not assimilated from this location) is significant.

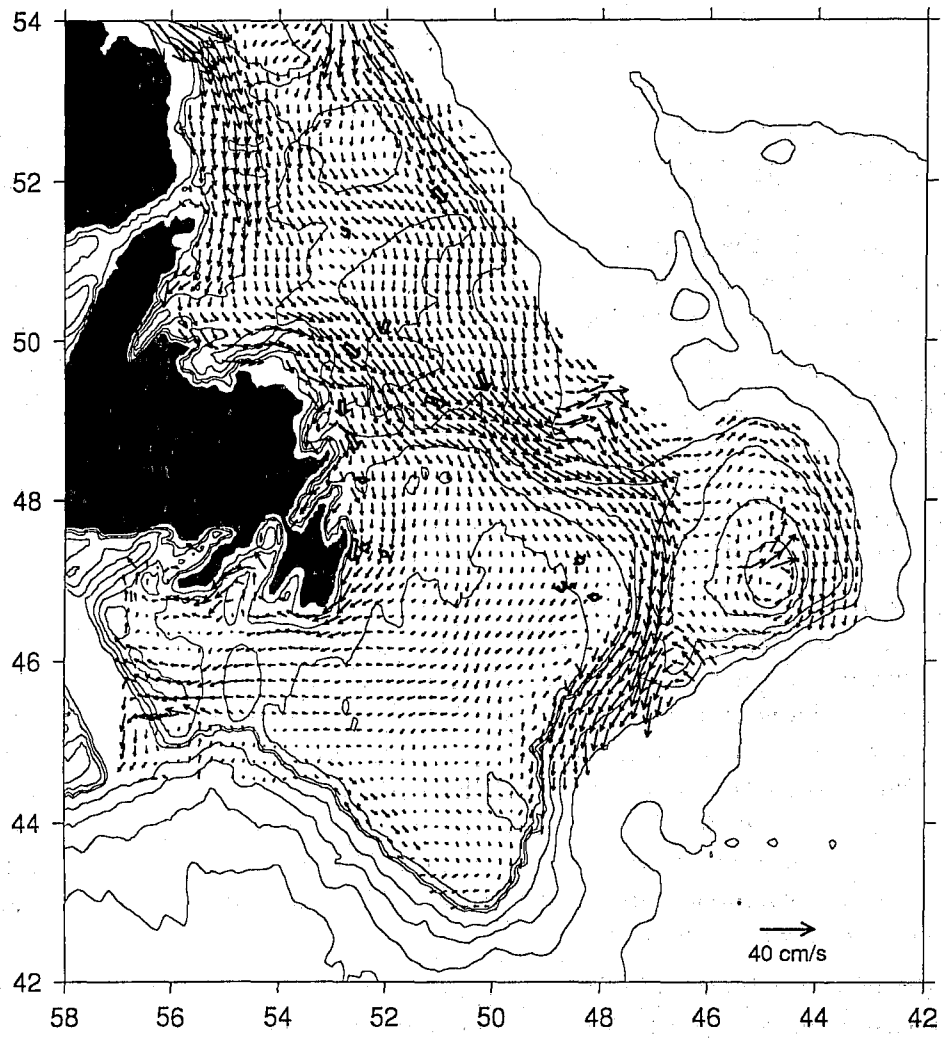

Figure 1: Mean summer surface circulation on the Newfoundland Shelf and Grand Banks. The gridded velocity field was calculated using a diagnostic method and an assimilation procedure to infer the optimal barotropic transports across the open boundaries to best fit the observations (also shown).

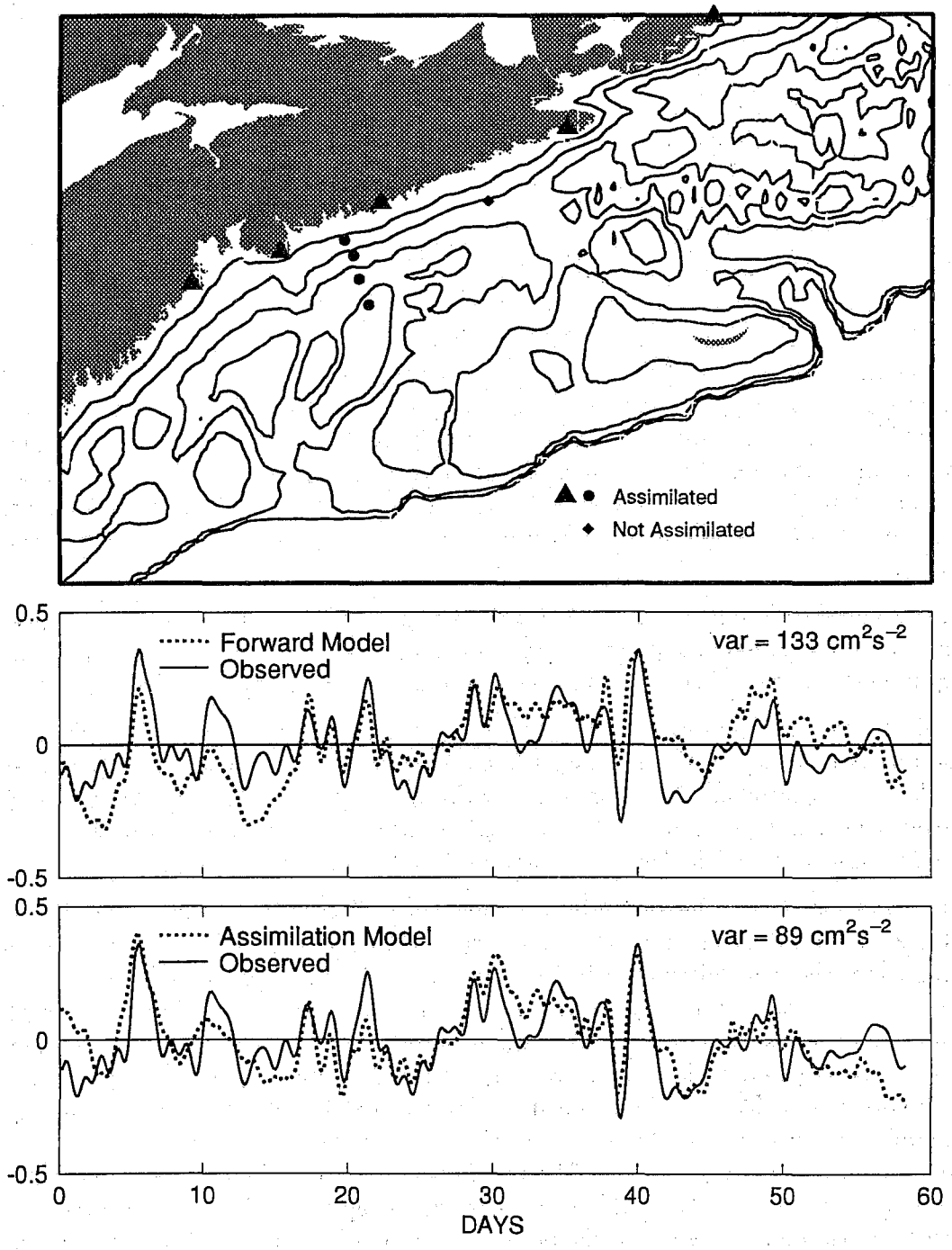

Figure 2: Validation of the Scotian Shelf assimilation model. The model was forced by Sable Island wind stress and Louisbourg sea-level (the most easterly gauge). An assessment of the predictive skill of the conventional model (laballed Forward Model, it does not asimilate data) is shown in the middle panel. The improvement in skill resulting from the assimilation of additional sea-levels and currents is clearly demonstrated in the bottom panel.

(ii) To fit the skill of our circulation model into context, we also predict the currents with a linear statistical model in which the dependent variable is expressed as a convolution of lagged coastal sea-level and wind with time-invariant weights. (The same independent variables were used to drive the circulation model in non-assimilation mode.) The statistical model is optimal in the sense that no other linear model with time-invariant weights can provide a better fit to the observations.

To quantify predictive skill we introduce the ratio (γ^2) of the variance of the prediction errors of the circulation model to the variance of the observations. For transport along the inner third of the shelf $\gamma^2 = 0.4$, indicating the model has significant predictive skill for this variable. For currents the model is most effective within about 40km of shore where γ^2 ranges between 0.51 and 0.66. At about half of the meters on these inshore moorings the performance of the circulation model rivals that of the statistical model. At the mooring deployed in the Nova Scotia Current, a primarily baroclinic jet with its center about 50km from shore, both the statistical and circulation model fail to capture the bulk of the variance. We explain the poor model fits through the effect of horizontal shifts of the Nova Scotia Current. At the deepest mooring, in about 200m of water and 65km from shore, the variance of the predictions errors is similar to the variance of the observations ($\gamma^2 \approx 1$).

(iii) To illustrate what can and what cannot be detected in coastal sea-level we present in Figure 3 the first mode of variation, and its associated time varying amplitude, for the observed currents on the Halifax Line, and the residuals from the statistical model.

This figure shows that even though the statistical model accounts for a significant part of the observed variance, there remains a mode of current variation which is incoherent with the local wind at all frequencies and with no sea-level expression (the right panel). However it does have an expression in alongshore head and part of it can be captured by the circulation model with the assimilation of data from more coastal gauges.

(iv) One reason for the suboptimal performance of the circulation model driven by coastal sea-level and local wind stress is the assumption of a spatially uniform wind field. Driving the model with observed wind fields available for one Intense Observation Periods during CASP we were able to demonstrate the improvement possible in both alongshore transport and nearshore currents. We suggest another reason for the suboptimal performance of the circulation model, particularly at the offshore mooring, is the form of the open boundary condition. We assumed sea-level drops linearly with distance along the open boundary upstream in the sense of shelf wave propagation, ranging from the observed value at the coast to zero at the shelf break. This leads to low frequency currents that are underestimated close to shore, and overestimated in deep water. We speculate the form of the upstream boundary condition should be a function of frequency with a uniform inflow across the whole shelf in the so-called meteorological band, and an inflow trapped closer to shore at longer periods. This can be readily accommodated within the framework of data assimilation.

To conclude the talk I cover our plans, including the extension of the model domain to include the Gulf of St. Lawrence and Gulf of Maine, and the inclusion of a density field that is allowed to evolve with the flow.

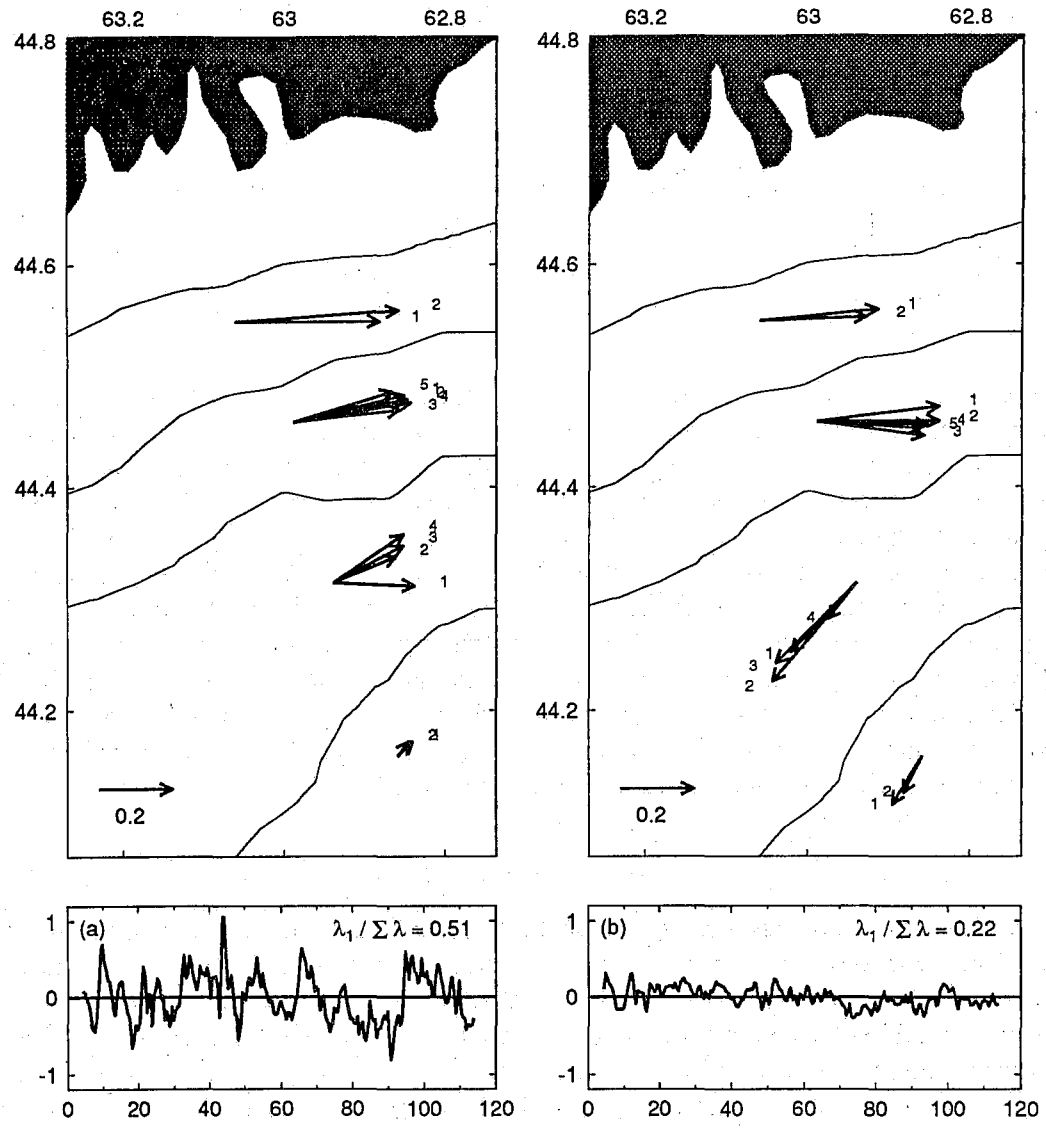

Figure 3: Principal component analysis of the (a) observed currents and (b) residuals from the statistical model. (Data cover a 110d period in the winter of 1985-6. They have been low-pass filtered to remove tidal variations.) The top panels show the eigenvectors (modes) associated with the largest eigenvalues (λ_1) of the 26×26 uv covariance matrix of observed or residual currents. The numbers associated with each vector indicate the postion of the current meter in the vertical. The smaller the number, the closer the meter to the sea-surface. The lower panels show the time variation in modal amplitude in ms^{-1}. The proportion of total current variance accounted for by each mode is shown in the top right corner.

A MODEL COMPARISON OF BAROCLINIC INSTABILITY IN THE PRESENCE OF TOPOGRAPHY

by

Catherine Griffiths, Moto Ikeda, Jia Wang and Peter C. Smith
Ocean Sciences Division, Bedford Institute of Oceanography
P.O. 1006, Dartmouth, Nova Scotia B2Y 4A2

Background

Present day numerical models are generally successful in reproducing the gross features of the oceans' circulation, but often fail to simulate some of the finer mesoscale processes accurately. Two possible reasons for this are: 1) the neglect of important mesoscale physics, and 2) numerical errors associated with the discretization process of the model. Here we focus on the ability of several eddy-resolving primitive equation models to simulate inherent instability of a strong baroclinic current in the presence of topography. The primary motivation for this work is to understand the nature of mesoscale variability and cross-shelf exchange associated with the Labrador Current off the east coast of Canada. Ultimately, we wish to assess the role of mesoscale eddies in transporting sea ice onto the northern Grand Bank in the vicinity of the Hibernia oil field. This model intercomparison is considered to be a necessary first step in this evaluation. It is particularly relevant since one of the primitive equation models studied is the Bryan-Cox model, whose modular form (MOM) is a leading candidate for the ocean component of ECIC's community ice-ocean forecast system.

Methods

Observations of the Labrador Current on the northern Grand Banks, including satellite imagery, moored current meter records and shipborne acoustic-doppler-current-profile (ADCP) transects, suggest that baroclinic mesoscale eddies with spatial and temporal scales of 30-50 km and 2-4 days, respectively, are ubiquitous along the inshore edge of the Current. To simulate this situation, three eddy-resolving primitive equation (PE) models and a quasigeostrophic (QG) model were formulated for a narrow (50 km) two-layer, baroclinic current (lower layer initially at rest) in a periodic channel with variable cross-channel topography. Instability of this system was investigated by perturbing the surface layer and measuring the growth rate of the resulting disturbance while the eddy kinetic energy was still small (5-15%) with respect to the mean. This technique was repeated for channels of different lengths in order to map instability growth rates as a function of wave number (2π/channel length).

The models used for this study are Ikeda's (1981) QG model, the Bryan-Cox z-coordinate model [BC; Bryan (1969), Cox (1985)], the Bleck-Boudra isopycnal-coordinate model [BB; Bleck and Boudra (1986)], and the Blumberg-Mellor σ-coordinate model [BM; Blumberg and Mellor (1987)]. All models had the same background state and horizontal resolution (order 5 km), but some minor differences in model physics [e.g. rigid lid (BC,BB) vs. free surface (BM)]. However, the computational schemes (e.g. vertical discretization, grids, temporal integration and smoothing) were all quite different. Also of particular relevance, the parametrizations of friction and diffusion varied among the models, both in terms of functional form and coefficient. For example, the QG model is frictionless, the BC and BB models have variants of Laplacian friction on horizontal and isopycnal surfaces (ν_h=50 m^2s^{-1}), respectively, and BM has an additional term proportional to the horizontal divergence (ν_h=65

m^2s^{-1}). [The larger friction coefficient for the BM model is required to counteract implicit negative viscosity associated with its predictor-corrector integration scheme].

Results

Over a flat bottom, instability diagrams (Fig. 1a) indicate that the maximum growth rates for the QG model exceed those of the PE models by at least 15% and that the peak rates for the PE models are shifted toward higher wavenumber ("blue shift") with respect to the QG model. Furthermore, the BM growth rates are suppressed by order 15% with respect to those of BC and BB. Sensitivity tests indicate that these differences are primarily caused by differences in frictional parametrizations within the models, rather than discretization or other variations in the computational schemes.

The effect of prograde topography (bottom slopes in the same sense as the density interface) is to stabilize all models, as indicated by the reduced growth rates in Fig. 1d vs. Fig. 1a. Furthermore, all models show a slight shift of the peak growth rate toward lower wavenumber ("red shift") with increasing prograde topography. In spite of greater reductions in the QG growth rates, the qualitative relationships among the models is the same as in the flat-bottom case. Moreover, all models are effectively stable at prograde slopes of $5x10^{-3}$ or greater.

Retrograde topography (bottom slopes in the opposite sense to the density interface) slightly amplifies peak growth rates in the QG model and shifts them to higher wavenumber ("blue shift"; compare Fig. 1b,c to Fig. 1a). The PE models also exhibit "blue shifts" of the peaks, but the growth rates are generally reduced over the flat-bottom case, particularly for the BC model. Furthermore, the amount of the shift is smaller for the BM than for the other models (e.g. compare positions of QG and BM peaks in Figs. 1c vs. 1a). Again, sensitivity tests show that the enhanced suppression of BC growth rates by retrograde topography is not a result of coarse vertical resolution, but the true cause remains unknown.

Finally, a study of energy conversions in the Bryan-Cox model has indicated that the nature of the instabilities varies with wavelength. The dominant energy source for all instabilities is the available potential energy of the basic state, but for short waves (e.g. 88 km), eddy kinetic energy feeds the mean ("pure" baroclinic instability) whereas for longer waves (e.g. 143 km), the mean kinetic energy partially fuels the eddies, indicating that the instability is mixed barotropic/baroclinic.

In conclusion, a model intercomparison of baroclinic instability in the presence of topography has shown that characteristics of the unstable waves (e.g. growth rates, peak wavelengths) are sensitive to differences in parametrizations and computational schemes. Consequently, care should be exercised in using these models to simulate important mesoscale phenomena.

References

Bleck, R. and D. Boudra. 1986. Wind-driven spin-up in eddy-resolving ocean models formulated in isopycnic and isobaric coordinates. *J. Geophys. Res., 91*, 7611-7621.

Blumberg, A.F. and G. Mellor. 1987. A description of a three-dimensional coastal ocean circulation model. In *Three-dimensional Coastal Ocean Models (ed. N. Heaps)*, Washington, D.C., AGU (Coastal and Estuarine Sciences, 4), 1-16.

Bryan, K. 1969. A numerical method for the study of the circulation of the world ocean. *J. Comput. Phys. 4*, 347-376.

Cox, M.D. 1985. An eddy-resolving numerical model of the ventilated thermocline. *J. Phys. Oceanogr., 15*, 1312-1324.

Ikeda, M. 1981. Meanders and detached eddies of a strong eastward-flowing jet using a two-layer quasigeostrophic model. *J. Phys. Oceanogr., 11*, 526-540.

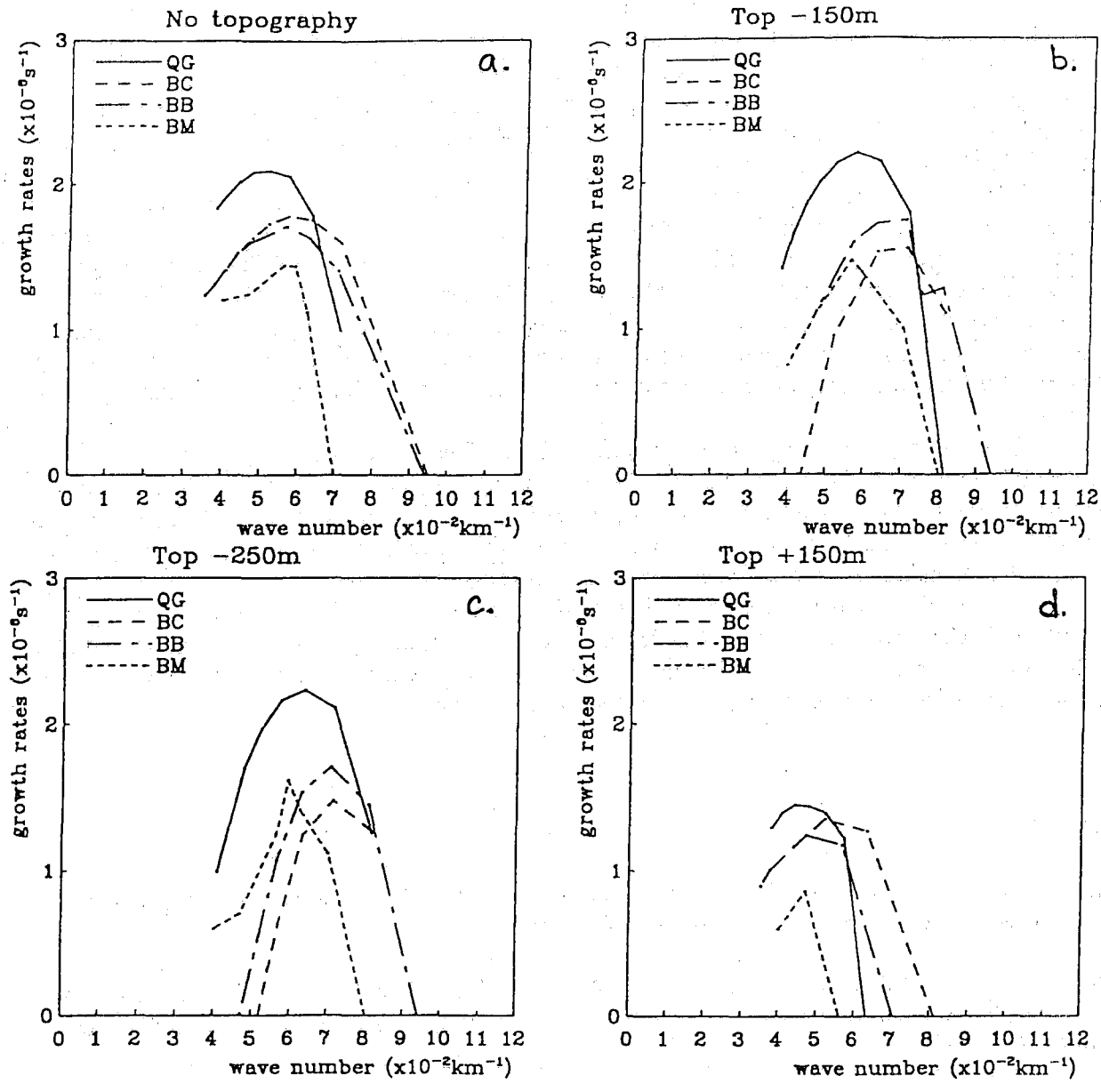

Fig. 1

MODELLING THE ICE-OCEAN SEASONAL CYCLE AND TIME-DEPENDENT CLIMATE RESPONSE TO ATMOSPHERIC FORCING AND RUNOFF IN HUDSON BAY

François J. Saucier[1] and Jacques Dionne[2]

1. Modelling and Climate Section, Maurice Lamontagne Institute, Department of Fisheries and Oceans, 850, Route de la Mer, Mont-Joli, Qc Canada G5H 3Z4. e-mail: saucier@nordet.qc.dfo.ca

2. Department of Oceanography, University of Quebec at Rimouski, Rimouski, Qc Canada G5L 3A1

This paper investigates the ice-ocean climate of Hudson and James Bays (herein labelled together HB), controlling the intermediate fate of 700 km^3 of freshwater flowing each year to the North Atlantic through Hudson Strait (HS) and the atmosphere. It attempts to quantify, through the application of a fully coupled ice-ocean model, the seasonal cycle of the ice-ocean system and the ways by which this one responds to external forcings.

As HB is relatively well sheltered from the oceans, its ice-ocean climate is controlled by the atmosphere and is not strongly influenced by the advection of ice or water from other basins. The Bay obeys weather patterns caused by the variability of the Icelandic low, and to a lesser extent the weather as far as the equatorial Pacific [Ikeda, 1990; Wang *et al.*, 1994]. A review of the known physical oceanography of HB can be found in Prinsenberg [1991] and Martini [1986]. The role of sea ice in the Bay's climate is strong; it covers the Bay eight to nine months of the year, mobilizes more freshwater than the yearly input from runoff, and requires annually more heat to melt than that transferred by the water column. A strong interannual variability is observed in the ice extent [Markham, 1986; Mysak and Manak, 1989; Ikeda, 1990; Wang *et al.*, 1994], in the timing of ice breakup [Catchpole, 1981; Etkin, 1991; Prinsenberg, 1991] and in the ice thickness [Loucks and Smith, 1989]. We have presently a limited and mostly empirical knowledge of the processes linking those Bay's responses to external forcings. Global warming, man-made changes in runoff from hydro-electric developments or natural interdecadal oscillations in the North Atlantic, for instance, produce or will produce effects yet difficult to detect or anticipate [e.g., Prinsenberg, 1991; Etkin, 1991; Wang *et al.*, 1994]. This is caused by the lack of observations and our inability to correctly model the complex sea-ice-atmosphere interactions. The models presented here help quantify detailed processes at work in the climate response of the Bay. It offers a means for characterizing anomalies that may be identified in the observations.

The Blumberg and Mellor [1987] coastal ocean model reproduces the ocean properties, albeit with a low lateral resolution of 40 km, a flat bottom fixed at 80 m depth (the approximate maximum mixed layer depth) and a vertical resolution defined by 21 levels. Embedded in this model is the 2½ turbulence closure model from Mellor and Yamada [1982]. The time-dependent prognostic ocean variables are 3D fields of salinity, temperature, velocities, and turbulent mixing coefficients K_M and K_H. The thermodynamic ice model is developed from Mellor and Kantha [1989]; the prognostic variables are mean ice thickness h_i, ice concentration A and ice velocity. The ice-ocean coupling is accomplished through consistent boundary conditions and source terms in the salt and heat equations accounting for frazil ice formation and penetrating radiation in the water column. The coupled model we formulate can reproduce seasonal and interannual equilibrium steady and unsteady solutions for an ocean with first year ice such as Hudson Bay, reproducing the ice cover properties as well as the ocean properties in a fully consistent manner.

The atmospheric forcing is described in the form of gridded monthly means of observations from 1951 to 1980 computed by the Canadian Environment Service. Eight stations distributed around the Bay were used to generate wind, precipitation, humidity and air temperature grids. Cloud cover and runoff were generated from shorter records [Danielson, 1971; Prinsenberg, 1977]. The sub-models for snow depth and conductivity, albedo, wind stresses and evaporation take detailed forms discussed in Saucier and Dionne [1995].

The Seasonal Cycle

Figure 1 illustrates a multi-year equilibrium solution driven from the 1951-80 climatology. We identified this solution as our control run because it reproduces well the available observations on ice thickness, concentration, mixed-layer depth, ocean salinity and temperature. Vertical fluxes are well balanced and a nearly steady state is reached after three years. Note that models of storms, snow depth and conductivity, as well as albedo were all required to render the solution accurate and very few degrees of freedom existed at the end of the calibration process, all variables being highly coupled. Density solutions support the previous models from Barber [1967], Danielson [1969] and Prinsenberg [1983]. The new pycnocline is formed in May at the onset of melt and deepens during summer from wind mixing and reduced freshwater inflow. In the fall, the mixed layer deepens under the effects of wind and from surface heat loss. When the ice season starts, the deepening accelerates and surface heat loss associated with salt rejection now dominate the vertical mixing. The pycnocline reaches a depth of approximatly 40 m on the average, more than 80 m in the northwestern part of the Bay and about 20 m in the southeastern region. Figure 1f shows the laterally averaged vertical mixing coefficient K_H. It rises to values above 10^{-2} m^2/s only during winter with a maximum of 0.1 m^2/s near 20 m depth in the January-February period when ice growth rate and salt rejection are maximum.

Stability is always minimum in northern Hudson Bay because relatively less heat enters the water column in summer and the locally produced ice is advected southward during freezing and melting seasons under the influence of dominant winds. Hence southeastern HB is partly covered in the early winter from ice produced in the north, before local ice production has started. But since the water column its more stable and the mixed layer thinner there, significant heat is left even when the ice concentration locally approaches one. This residual heat influences against local ice growth in the following months, when it is mobilized by convection penetrating from salt rejection. This suggests that the pre-conditioning of the mixed-layer (or the heat content of the water column at the onset of ice) is an important factor controlling the ice growth rate in the early winter. This process is similar to the one proposed by Malmberg [1969] and demonstrated through a series of sensitivity experiments described below.

Figure 3 shows the net oceanic heat and salt fluxes (including river runoff). The net computed annual oceanic heat flux is 0.1 W/m^2, as expected near zero. The model reproduces monthly heat fluxes close to estimates from Danielson [1969]. The mean daily heat flux reaches magnitudes of more than 100 to 150 W/m^2 but for relatively short periods of time around days 200 (negative peak) and 300 (positive peak). Anomalous weather conditions during these periods can have

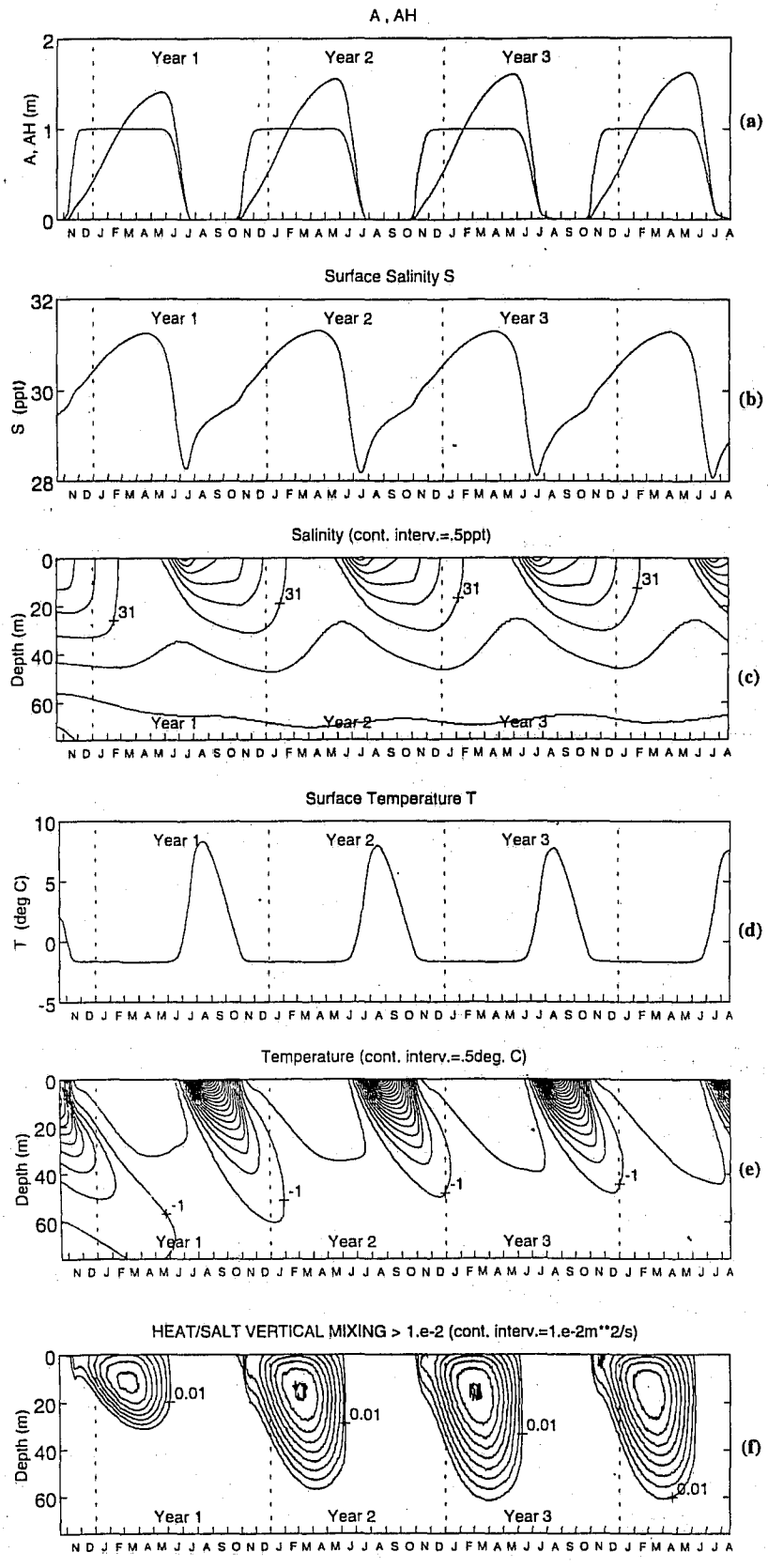

Fig. 1. First four years area-averaged solution for the 1951-80 climatology. (a) Times series of ice thickness Ah_i and concentration A; (b) Sea surface salinity; (c) Salinity isopleths; (d) Sea surface temperature; (e) Temperature isopleths; (f) Vertical heat and salt mixing coefficient K_H.

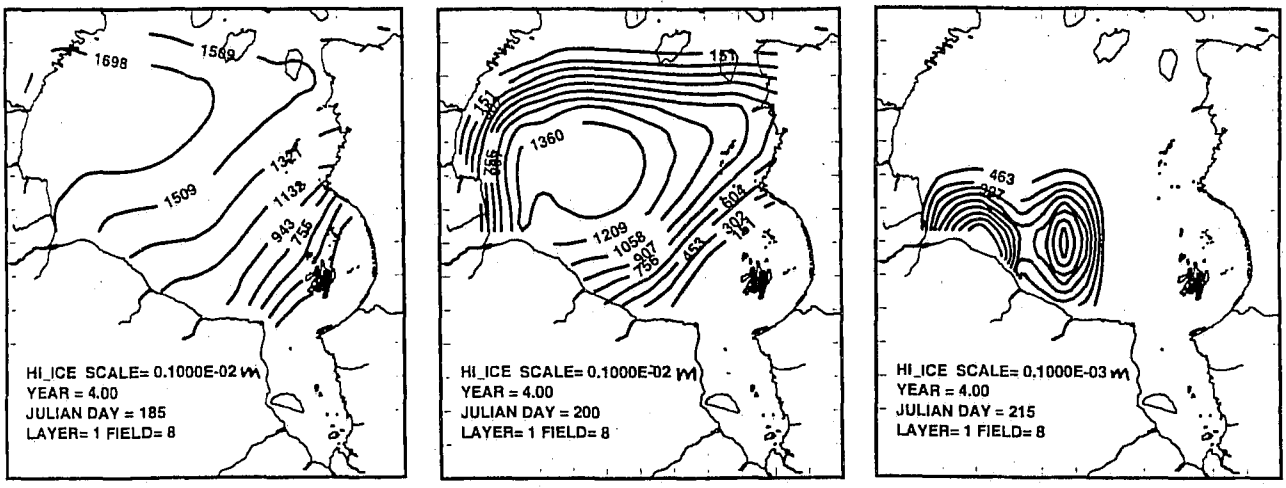

Fig. 2. Sea-surface thickness Ah_i during melt. July 5, July 20 and August 5 of the fourth year control run solution.

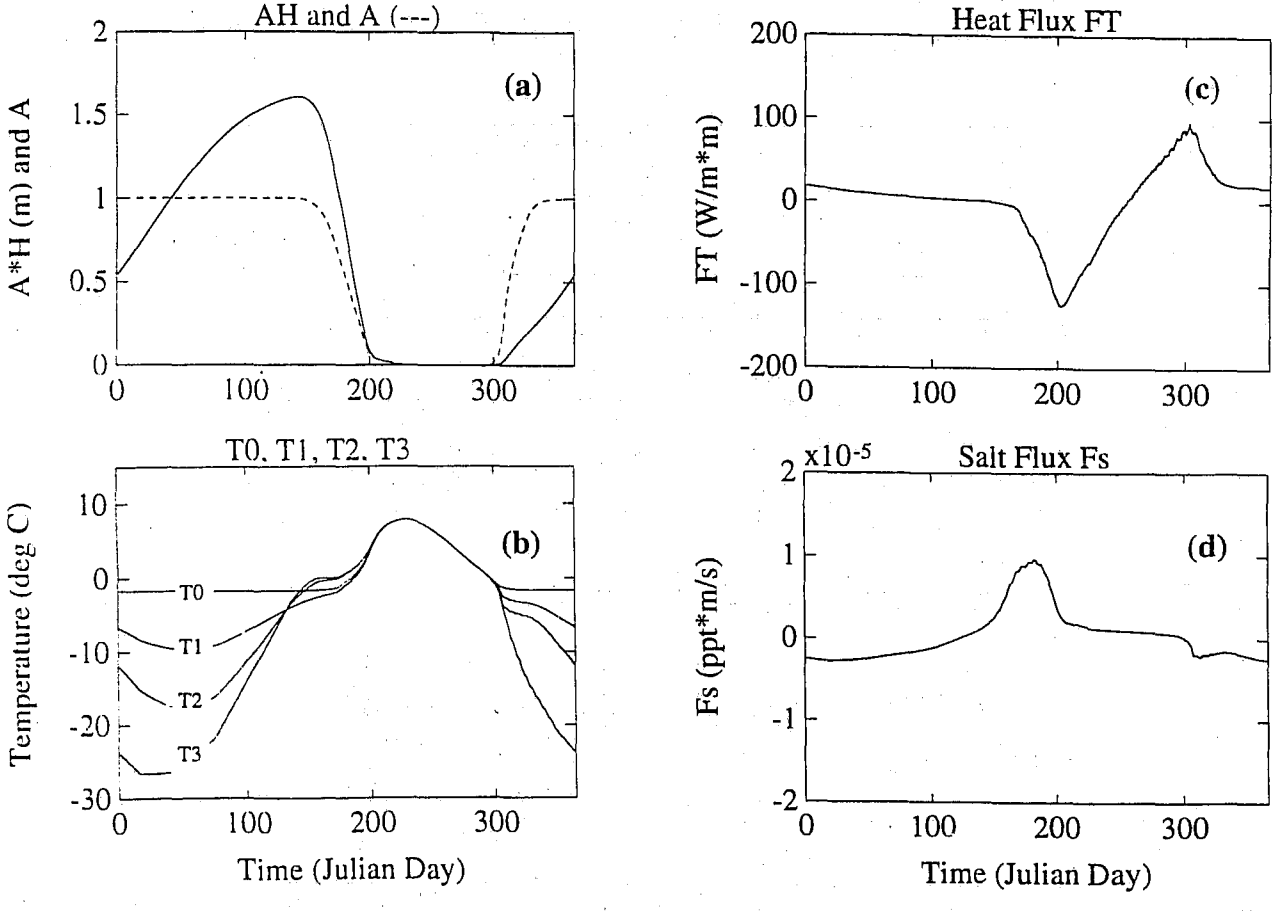

Fig. 3. The fourth year seasonal cycle of the control run solution. (a) Ice thickness and concentration; (b) Internal and ice-boundary temperatures T_0, T_1, T_2 and T_3; (c) Area-averaged oceanic heat flux; (d) Area-averaged oceanic salt flux.

important effects on the net yearly heat loss or gain of the Bay. For example, reduced cloud cover during peak radiation (June) modify F_T and the ice-ocean conditions significantly. Also, decreased storm intensities during fall can produce a net annual heat gain by several W/m^2.

The oceanic salt flux (Figure 3d) is controlled by precipitation, evaporation, runoff and ice production. The mean value obtained for F_S has also been estimated from the freshwater budget independently. It corresponds to the salt deficit that we compensate from a basal flux representing exchanges at the northern boundary.

Sensitivity Experiments

Multi-year transient solutions, sensible to perturbations in the external forcing, were examined:

(1) A strong westerly event from the North Atlantic Oscillation. A surface air temperature anomaly of -1.5°C over HB during winter produces rapidly a layer of 4 cm of ice. The sea surface temperature decreases by 2°C in the summer but the anomaly reduces to -0.04°C in the fall. The ice production anomaly is resorbed at 90% in the following year if normal conditions apply.

(2) Anomalous runoff year. An anomalous year with high runoff (+30% in the first half of the year) produces an ice thickness anomaly of ~8 cm in southeastern HB but only 4 mm overall. This is directly a result of stability enhancement. Early in the following winter, ocean stability enhancement and fall precondioning oppose each other to produce a damped and complex sea ice anomaly, negative in southeastern HB but positive on the average. Stability enhancement increases ice production but the residual heat stored in the water column is expelled more slowly than normal. However, stability enhancement effects dominate that next year, producing a positive ice thickness anomaly.

(3) Regulated runoff. Planned man-made changes to runoff in HB control ice conditions in the conterminous estuary/eastern coastal region. Sea-ice thickness is enhanced by more than 7 cm in James Bay/southeastern HB but less than 7 mm over the Bay, in immediate response to excess runoff during the winter months. However, the equivalent of more than 90% of the excess freshwater runoff remains liquid. Only short-lived but relatively important negative sea surface temperature anomaly (-0.4°C in southeastern HB) is computed at the end of the melting season.

(4) High wind or negative fall surface air temperature anomaly. These experiments demonstrate the importance of late summer heat flux and water column pre-conditioning at the onset of ice in HB. Under normal summer conditions, the heat stored below the mixed layer is later trapped beneath the complete ice cover. When transferred through the ice cover from the mixed-layer to the atmosphere, it negatively influences the ice growth. In this experiment, for a surface air temperature decreased by 2°C or a storm intensity doubled during a two month fall period, the ice thickness anomaly is about 6 cm all through the following ice season. This is larger than that modeled for a strong westerly winter event or regulated runoff conditions.

(5) Warm conditions. A 3°C step in air temperature has important effects reducing the annual ice produced in HB by 20% within 4 years. The summer sea surface temperature increases by more than 4°C; delay and advance of two weeks are computed for the freeze and breakup dates, respectively.

The models proposed here do not resolve important aspects that should be introduced in future work. A next step is to increase resolution to obtain eddy and plume resolving models with variable topography and more realistic northern boundary conditions. These models will allow more detailed descriptions of local effects associated with sea ice and oceanic conditions near river estuaries. Models should also be run for many more years and further coupled to real high frequency atmospheric changes, rather than normals. This would provide transient self-consistent solutions that could be directly compared to observations. Other improvements to the present models include considering further coastal lead effects, heat import from rivers, tidal effects, and ice rheology.

Acknowledgements. This work was supported by the Panel on Energy and Resources Development (PERD) and the Canadian Department of Fisheries and Oceans.

References

Barber, F. G., *Manuscript Report Series No.4*, Dept. of Energy, Mines and Resources, Ottawa, 69 pp. 1967.

Blumberg, A. F., and G. L. Mellor, *Coastal and Estuarine Sciences, 4,* 1-16, 1987.

Catchpole, A. J. W., and T. F. Ball, in: Climatic Change in Canada 2, Edited by C. R. Harington, *Syllogeus No. 33*, National Museums of Canada, 48-96, 1981.

Danielson, Jr. E. W., *Marine Sci. Manuscript Rep. No.9,* McGill University, Montréal, 196 pp. 1969.

Danielson, E. W., Hudson Bay ice conditions, *Arctic, 24*, 90-107, 1971.

Dickson, R. R., E. M. Gmitrowicz, and A. J. Watson, *Nature, 344*, 848-850, 1990.

Etkin, D. A., *Climatological Bull., 25*, 21-34, 1991.

Ikeda, M., *Atmosphere-Ocean, 28(1),* 106-139, 1990.

Loucks, R. H., and R. E. Smith, *Can. Contractor Rep. Hydrogr. Ocean Sci, 34,* BIO, 48 pp., 1989.

Markham, W. E., in: Canadian Inland Seas, I. P. Martini Ed., Elsevier Oceanography Series, 44, 101-116, 1986.

Martini, I. P. (Ed.), Canadian Inland Seas, Elsevier Oceanography Series, 494 pp., 1986.

Malmberg, S. A., *Joekull, 19*, 30-43, 1969.

Mellor, G. L., and T. Yamada, *Reviews of Geophysics and Space Physics, 20*, 4, 851-875, 1982.

Mellor, G. L., and L. Kantha, *J. Geophys. Res., 94* (C8) 10,937-10,954, 1989.

Mysak, L. A., and D. K. Manak, *Atmosphere-Ocean, 27* (2), 376-405, 1989.

Prinsenberg, S., Ocean and Aquatic Sciences, Fisheries and Environment Canada, Unpublished manuscript, 71 pp., 1977.

Prinsenberg, S. J., *Atmosphere-Ocean, 21* (4), 418-430, 1983.

Prinsenberg, S. J., Potential Environmental Impacts Series No. 2, North Wind Information, Montréal, 8 pp., 1991.

Saucier, F. J. and J. Dionne, in review, *J. Geophys. Res.*, 1995.

Semtner, A. J. Jr, *J. Phys. Oceanogr., 6*, 379-389, 1976.

Wang, J., L. A. Mysak, and R. G. Ingram, *Atmosphere-Ocean 32* (2), 421-447, 1994.

Simulation of the Climatological Seasonal Cycle of Northern B.C. Waters with the Princeton Ocean Model

P.F. Cummins
Institute of Ocean Sciences
P.O. Box 6000
Sidney, B.C., V8L 4B2, Canada

L.Y. Oey
Sayre Hall, Forrestal Campus
Princeton University
Princeton, NJ 08544-0710, U.S.A.

(Abstract only)

Abstract

Preliminary results from an application of the Princeton Ocean Model (POM) to the coastal waters off northern British Columbia are discussed. The initial objective of the study is simulation of the climatological seasonal cycle of the region including Dixon Entrance, Hecate Strait and Queen Charlotte Sound. A numerical experiment with wind and buoyancy forcing derived from standard climatological atlases shows reasonable agreement with observations on several points. This includes the occurrence of a cyclonic eddy in Dixon Entrance, seasonally varying flow in Hecate Strait and a surface outflow at Cape St. James. The results show considerable differences with previouus shallow water modelling of the region, although significant topographic control of the flow is still evident.

Three-dimensional Prognostic Modelling of the Georgia-Fuca Basin Using GF8

James A. Stronach and Donald O. Hodgins
Seaconsult Marine Research Ltd.
Vancouver, B.C. V6P 4G1
PHONE: (604) 266-9135
FAX: (604) 266-8855

GF8 is a fully-prognostic, three-dimensional baroclinic numerical model of hydrodynamics in coastal seas. It has been used in both engineering studies of geographically limited areas and in oceanographic research for larger regions, extending to continental shelf scales. In this paper, the model is described and examples from its validation and application to engineering and oceanographic situations are presented.

GF8 represents mature modelling technology, having been used in various forms since the early 1980's. It's origin was a model developed by Jan Backhaus at the University of Hamburg. That code was modified by Dr. J. Stronach of Seaconsult Marine Research Ltd. to accommodate the complex and energetic waters of the Georgia/Fuca system using a 2-km grid (Stronach et al., 1993). The resulting new model was named GF8, in accord with a numbering scheme initiated by Dr. Pat Crean of IOS for models of the Georgia/Fuca system. Subsequent use of the model for research and engineering studies at Seaconsult Marine Research Ltd. has led to further enhancements to the modelling technology. The present configuration of the model is robust and accurate, and has been used successfully with grid sizes extending from 9.3 m to 5 km. As well, the accuracy and efficiency of the GF8 hydrodynamic model has led to the development of various integrated applications including simulation of the fate of dissolved contaminants, hindcasting of three-dimensional temperature distributions and hindcasting phytoplankton and herbivore populations. The key to these applications lies in the accuracy and speed of the hydrodynamic model.

Model geometry is schematized using a rectangular grid of square meshes overlain on a Mercator chart. In the vertical, the water column is resolved into a number of fixed levels, with the number of active layers adjusted to local water depth. The lowest layer in each cell is allowed to have a depth differing from the nominal depth of that layer, thus preserving depths for bottom flushing and for determining the local wave speed. Time stepping is semi-implicit, so that the severe restrictions of the CFL criterion on time step and grid size don't apply. Thus, time steps as much as 20 times larger than the timestep required for an explicit model can be used. The implicit aspects of the model are solved using a successive over-relaxation technique for the continuity equation and a Crank Nicholson scheme for vertical eddy viscosity and diffusivity.

An essential requirement for engineering applications is that the hydrodynamic model include all relevant physical forces, so that the computed flow field is as close as possible to the naturally-occurring one. This approach has proven highly effective, allowing simulations of surface currents in response to tide, river and wind forcing; simulation of bottom water renewal in Juan de Fuca Strait, and general simulation of the complete three-dimensional structure of the current field in an estuarine setting. To incorporate the complete set of physical processes, GF8 includes the following features:

- forcing by tidal water level at open boundaries;
- cross channel dynamics at open boundaries are constrained to Kelvin wave behaviour;
- river flow may enter at any cell, with variable river mouth width and depth and river flow tidally modulated by local water level;
- adjustable grid cross-sectional and surface areas, to allow specification of narrow passes;
- friction enhancement factors for user-specified grids;
- surface wind stress resolved on an hourly and grid-scale basis;
- automatic provision for long-term changes in the density field at open boundaries to simulate seasonal cycles;
- Mellor-Yamada second order turbulence closure;
- Mellor-Yamada bottom friction coefficient;
- Smagorinsky formulation of horizontal eddy viscosity, depending on local rate of strain.

The above elements, particularly the inclusion of narrow grid cells, were found to be essential in order that GF8 provide a reliable description of a complex region such as the Georgia-Fuca system using the limited resolution afforded by a 2-km grid.

A separate transport-diffusion (TD) model based on a flux-corrected formulation is used for the simulation of the advection and diffusion of passive scalars such as wastewater from a submerged outfall. The flux-corrected algorithm provides accurate solutions in which numerical dispersion is well-controlled, a prime concern when the source function is of limited spatial extent such as a submerged outfall. The TD model has been proven to replicate the dispersion observed in dye studies, and also provides realistic distributions in response to such flow features as eddies and fronts.

The combined hydrodynamic and TD models have been extensively validated using a number of different approaches. The first validations were done by comparing the reproduction of tidal water levels and tidal currents with observations, using the network of tide gauges and current meter observations readily available in the Georgia-Fuca-Puget system. The model successfully reproduced all features of the system, including the extensive modifications that the semi-diurnal tide undergoes as it passes through the system. For instance, the M2 tidal amplitude had a 6% rms error throughout the system, and the rms error in M2 currents was of similar magnitude.

For modelling the movement of contaminants and naturally-occurring substances such as phytoplankton, a more important validation is to compare the observed evolution of scalar fields with the modelled evolution. This has been done in several dye-tracing studies, which are described later. First, a validation with respect to the advection of denser water from the Pacific Ocean into Juan de Fuca Strait will be discussed. The process to be simulated is the annual renewal of bottom water in the system. An early investigation of the process was discussed in Crean et al. (1988), based on measurements between March 5 and April 16, 1973. It was observed that over this 6-week period, denser water which was originally at depths of 200 m in the offshore moved up onto the sill at the inner end of Juan de Fuca Strait.

A severe test of a three-dimensional model is to determine to what extent it can simulate this density intrusion. Based on the 6 CTD sections obtained near the entrance to Juan de Fuca Strait over this 6-week period, a time-series of sigma-t sections was generated to provide boundary conditions for a GF8 simulation. The boundary conditions for density are implemented so that the slowly-varying signal from approximately weekly boundary data such

as the CTD observations can be smoothly blended with the tidally-varying processes occurring in GF8. In addition to the density data at the mouth of Juan de Fuca, winds from a network of coastal lighthouses including Cape Beale and Race Rocks were also used in the simulation. Water levels were obtained from harmonic constants at the open boundaries.

Figure 1 presents a comparison of the observed and modelled intrusion at the end of the observation period. In both cases, water with a salinity of 33 ppt was original located at depths greater than 200 m off Cape Flattery, but has ultimately moved up over the sill at Victoria. The agreement between model and observations is excellent, especially considering that there were no observations between March 16 and April 13, so the model relied on linear interpolation in time over this interval. This close agreement lends considerable credibility to the use of GF8 for long-term simulations. It is remarkable that this process was simulated without the use of observed water level data, the water level boundary condition being derived solely from tidal harmonic constants. This realistic simulation illustrates that the intrusion process is primarily baroclinic, and information on the density field at the mouth is essential for its complete description.

GF8 and TD are powerful tools to evaluate the operation of a wastewater disposal system. Although a number of packaged models are available to estimate the initial dilution from a submerged outfall, they cannot adequately describe the spatial distribution of contaminants in the far field, nor are they suited to determining long-term chronic conditions. The combined GF8 and TD system are well-suited to these tasks, and are particularly useful when used at two different spatial scales. Typically, a high resolution grid is embedded within the overall 2-km grid, so that conditions in the immediate vicinity of the outfall are simulated with a grid scale commensurate with gradients in the contaminant distribution field. The overall model provides much better boundary condition data for the high-resolution model than could be obtained observationally. Moreover, by carrying the contaminant distribution from the high resolution model into the overall model, effects in the extreme far field can be calculated as well.

A study of the wastewater distribution in Ganges Harbour on Salt Spring Island provides an good example of these concepts. Sewage from the surrounding area is treated in a sewage treatment plant in Ganges and discharged through a submerged outfall extending about 1.8 km into Ganges Harbour. The sewage treatment plant presently discharges only on a falling tide. Considerable savings in capital and operating costs in the future would be obtained if the plant switched to a continuous discharge mode, but concerns about increased contamination on flooding tides had to be investigated. Seaconsult addressed the problem using a combination of observations and modelling. First, a dye study was conducted at the existing outfall. Dye was injected in the holding tanks at the treatment plant and tracked as it emerged from the outfall. Maps of dye concentration at about 3-hourly intervals were prepared, and the dilution and advection of the contaminant cloud were described. Next, a version of GF8 with a 166-m grid was used to simulate the dye experiments. Close agreement was found, both in terms of advection and dilution of the dye cloud. Calibration of the hydrodynamic model was also done against a moored current meter in the harbour, and showed good agreement. The final step was to operate two parallel versions of the model over an extended time period. One version discharged on an ebb tide only, and the other used a continuous release mode of operation. Maps of maximum and average contaminant level for the two modes of operation were prepared. The conclusion was that, as expected, contaminant levels in Ganges Harbour rose with the continuous release mode of operation, but the dilution was still large enough that contaminant levels remained about two orders of magnitude below health standards. This

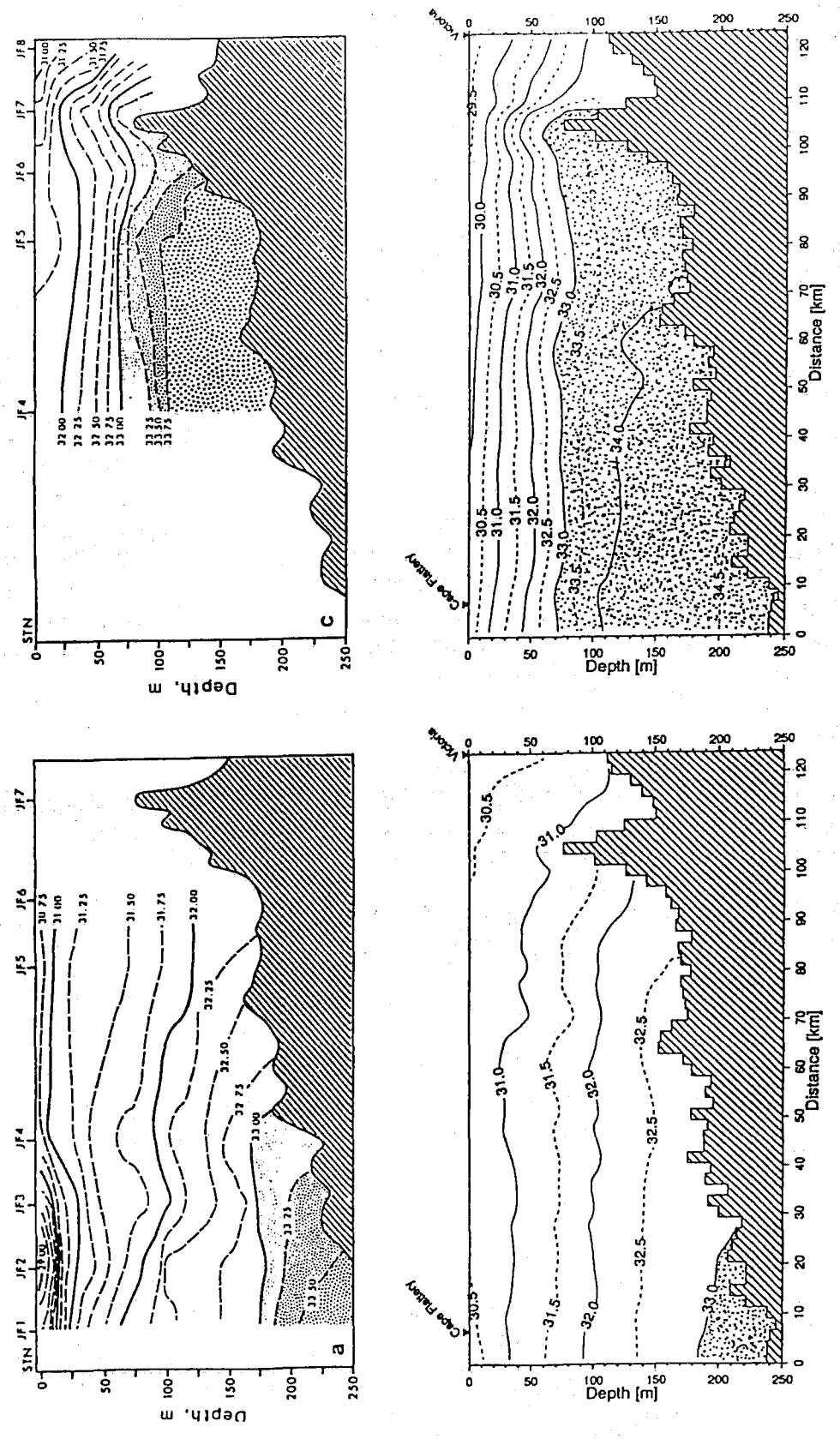

Figure 1

application shows how three-dimensional numerical modelling can be used to address the concerns of government agencies and citizens in the management of valued coastal resources. Model output provides quantitative data for engineering calculations, and can also be used, through flow visualization tools, as a major part of public presentations.

Other applications have been the use of a 5-km grid version of GF8 to simulate currents in the Gulf of St. Lawrence, including generation of features such as the Gaspe Current. GF8 was also used with a grid size of 9.3 m to simulate the flow around the Hibernia production platform. That simulation was dominated by the generation of an oscillatory wake in the lee of the platform, the frequency of which satisfied Strouhal number scaling.

The examples above illustrates GF8's utility in a wide range of situations. Observations using HF radar in both Juan de Fuca Strait and the Strait of Georgia indicated that a 2-km model under-resolves some flow features. Early results from a 1-km model indicate that a number of flow field characteristics such as eddies, fronts and sinuous stream lines which have been observed in the Seasonde observations are now appearing in modelled surface currents. Figure 2 illustrates an instantaneous velocity field in the southern Strait of Georgia. Notable features include the various eddies and jets which form throughout the system, as well as the Fraser River plume. To the south, a starburst feature in the flow emerging from Boundary Pass is evident. This feature is likely part of the dynamics of internal wave generation in the southern Strait of Georgia. Future comparison of the computed velocity fields and SAR image data will assist in both interpreting SAR images and in validating aspects of the 1-km hydrodynamic model.

References

Stronach, J.A, J. O. Backhaus and T.S. Murty. 1993. An update on the numerical simulation of oceanographic processes in the waters between Vancouver Island and the mainland: the GF8 model. Oceanogr. Mar. Biol. Annu. Rev., 31, 1-86.

Crean, P.B., T.S. Murty and J.A. Stronach, 1988. Mathematical Modelling of Tides and Estuarine Circulation. Springer-Verlag. New York. 471 pp.

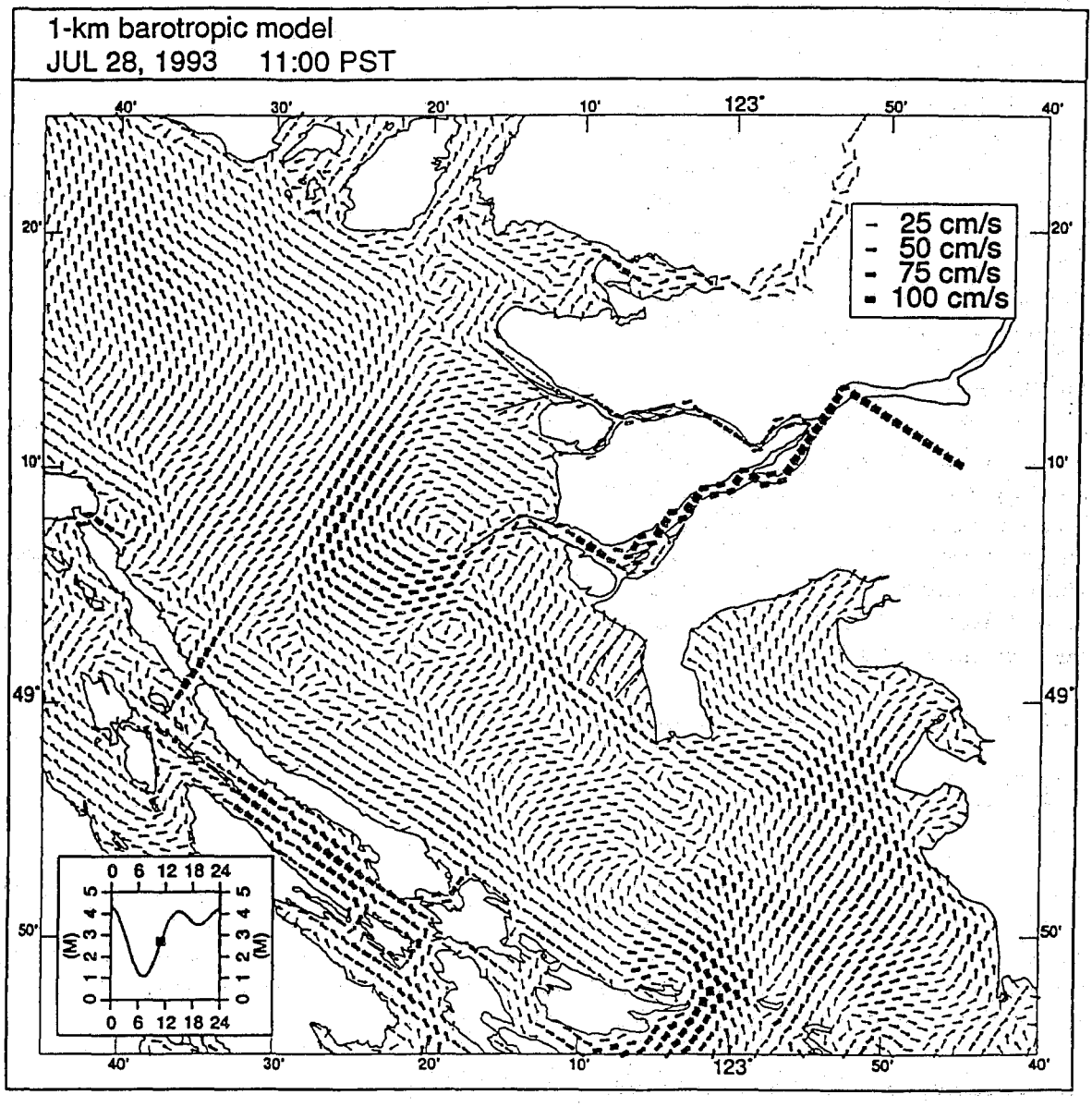
1-km barotropic model
JUL 28, 1993 11:00 PST
40'
30'
20'
10'
123°
50'
40'
20'
10'
49°
50'
25 cm/s
50 cm/s
75 cm/s
100 cm/s
0 6 12 18 24
0 1 2 3 4 5
(M)

Figure 2

The Vertical Structure of Turbulent Dissipation in Shelf Seas

J.H. Simpson, W.R. Crawford*, T.P. Rippeth, A.R. Campbell and J.V.S. Cheok

University of Wales, Bangor
School of Ocean Sciences
Menai Bridge, Gwynedd, LL59 5EY

*Canadian Hydrographic Service
Institute of Ocean Sciences,
Sidney, B.C. V8L 4B2

Models of Turbulent Dissipation

A central part of the current agenda in physical oceanography of shelf seas is to understand the interactions of the processes which control the vertical structure and diffusion of properties throughout the water column. First order accounts of the evolution of the density structure have been given in terms of "prescriptive models", which are based on the energy arguments and simplified assumptions about the efficiency of mixing processes. Such models do not deal with dynamics of tidal and density driven flow explicitly, but rely on combining analytical solutions for each component of the flow. Our strategy here is to test the models by comparing measurable aspects of the turbulence with model simulations. We use a set of observations of the rate of dissipation of turbulent kinetic energy in several tidal flow regimes in the Irish Sea.

The flow properties, both mean and turbulent, are compared with hindcasts of the flow using point models of the dynamics and vertical diffusion with different closure schemes. Initially we shall use the 1-D dynamics model (Simpson and Sharples, 1992) with a Mellor-Yamada level 2 closure scheme, arguably the simplest type of scheme needed to integrate the equations of motion. The bottom boundary condition is a quadratic stress law; wind stress at the sea surface is also given in terms of a quadratic drag prescription using observed hourly wind vector data. The horizontal pressure gradient consists of two terms. The first is an oscillating sea surface slope which provides the tidal forcing, derived from a 2-D vertically integrated model (Proctor and Smith, 1991). A second term represents the mean surface slope.

The vertical diffusion of heat and salt in the equations takes the form

$$\frac{\partial(s,T)}{\partial t} = \frac{\partial}{\partial z}\left(K_z \frac{\partial(s,T)}{\partial z}\right)$$

where K_z is the coefficient of vertical eddy diffusivity. A level 2 turbulence closure scheme is used to calculate vertical profiles of K_z as functions of local stability and the local gradient Richardson number. The equation for the time-rate-of-change of turbulent kinetic energy is determined by a local production term, a local dissipation term, and a buoyancy term. In the level 2.2 closure scheme the vertical diffusion of turbulent kinetic energy is also present.

Measurements of Turbulent Dissipation.

The observations over one or two tidal cycles were made at three sites in the Irish Sea during March and July 1993. The two strongly mixed sites M1 and M3 were the focus of the March campaign, while in July we made contrasting observations at M1, and the low energy site S1 where strong seasonal stratification prevailed. The measurements of dissipation were made using the FLY II profiler (Dewey et al., 1987) which is equipped with a guard ring which allows measurements to be made to within 15

cm of the seabed. The measurements thus cover almost the entire water column. The profiler falls freely at a speed of 0.70 to 0.80 m s^{-1} and measures components of the horizontal velocity with a turbulence shear probe. Dissipation ε is computed from shear measurements using the isotropic turbulence equation.

Results

We present results from the mixed regime M1 and the stratified regime S1. Figures 1 and 2 illustrate the measurements at M1 and S1 respectively over a 25-hour period, in the form of $\log_{10} \varepsilon$. At M1 the mean depth is 60 m and the tidal stream at surface has M_2 amplitude of about 1 m s^{-1}. At S1 these numbers are 90 m and 0.45 m s^{-1}. At M1 dissipation generally decreases with height by three orders of magnitude from peak values of $\varepsilon = 0.1$ watts m^{-3} close to the seabed. At all levels the intensity of the dissipation is clearly related to the phase of the current so that there is a marked quarter-diurnal variation in ε, with a phase lag which increases with height. At S1 the peak values of ε near the seabed are about 0.03 watts m^{-3}. At mid depths there is an extensive region of low dissipation where ε is about 1×10^{-5} watts m^{-3}. This rate of dissipation of turbulent kinetic energy is about one and a half decades above the noise level for FLY II measurements. In contrast to the well mixed cases, the pronounced quarter-diurnal variation of ε at S1, while marked near the bottom boundary, only extends upwards to a height of about 40 m above the bed. Within this boundary layer region there is again an increasing delay in the time of maximum dissipation with height above the seabed.

The corresponding model simulations are plotted below the contours of measured dissipation. The bottom panel present the level 2.0 closure scheme, and the next panel up presents the level 2.2 results. These predictions have been made using the tidal forcing directly from the 2-D model, and without tuning the Mellor-Yamada closure parameters from the Simpson and Sharples (1991) values. The models reproduce all the main features of the observed ε distribution at M1, although the fit is somewhat better for the MY2.2 version.

At S1 the model reproduces the principle characteristics of the observed behavior in most respects, but the model values of ε in mid-water, in the thermocline, are significantly lower than observed. The model essentially shuts down any turbulence and associated dissipation and mixing, whereas the measurements clearly show significant turbulence levels within the thermocline. These results indicate that any parametrization of turbulence using the Mellor Yamada scheme should have a background turbulence level within the thermocline.

References

Dewey, R.K., W.R. Crawford, A.E. Gargett and N.S. Oakey, 1987. A microstructure instrument for profiling oceanic turbulence in coastal bottom boundary layers. *J. Atmospheric and Oceanic Technology*, **4**, 288-297.

Proctor, R. and J.A. Smith 1991. The depth-averaged residual circulation on the North West European Shelf. Proudman Oceanographic Laboratory, Report 20.

Simpson, J.H. and J. Sharples 1992. Dynamically active models in the prediction of estuarine stratification., in *Dynamics and Exchanges in Estuaries and the Coastal Zone*, ed by D. Prandle, AGU, 101-113.

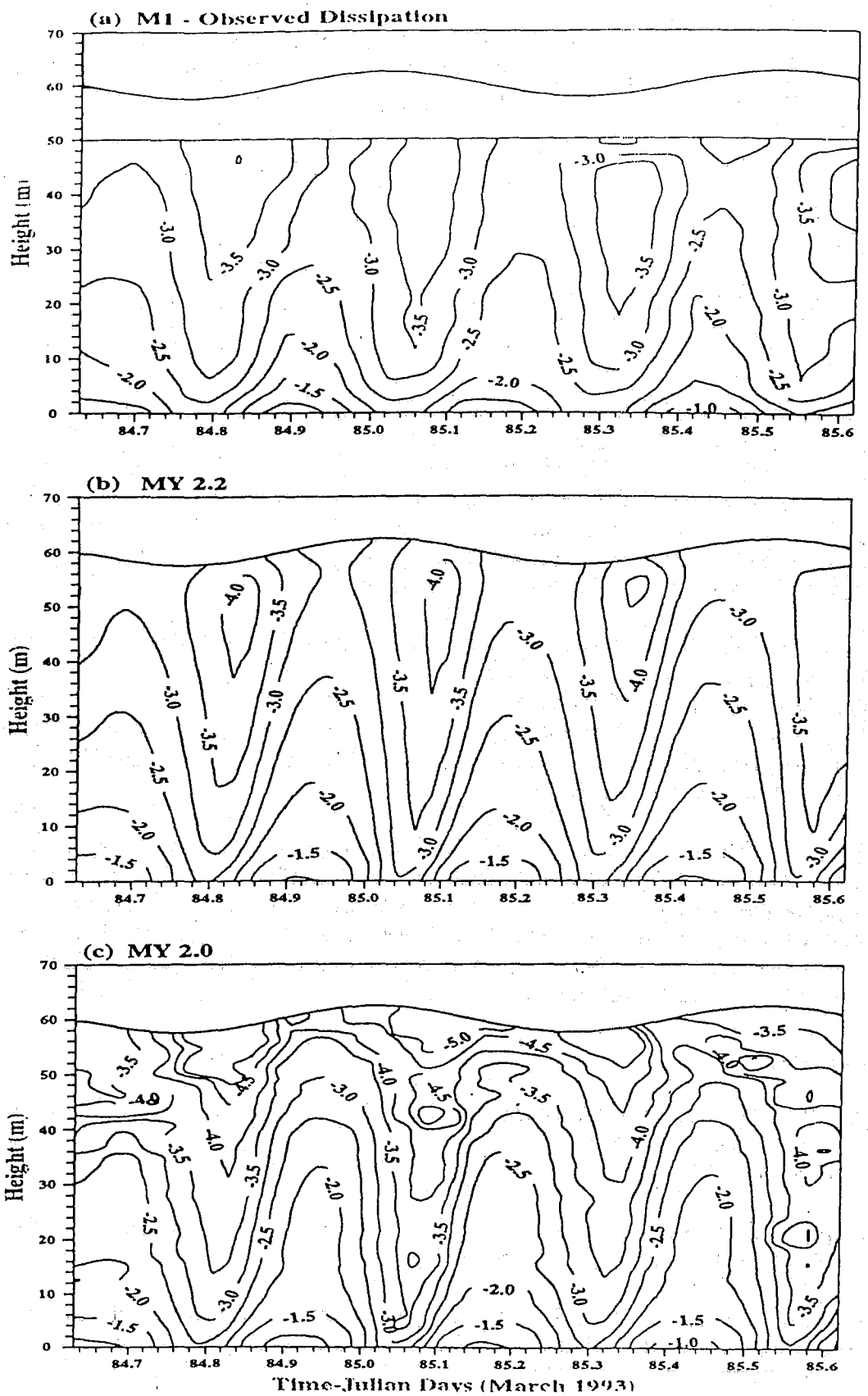
(a) M1 - Observed Dissipation
(b) MY 2.2
(c) MY 2.0
Height (m)
Time-Julian Days (March 1993)

Figure 1.

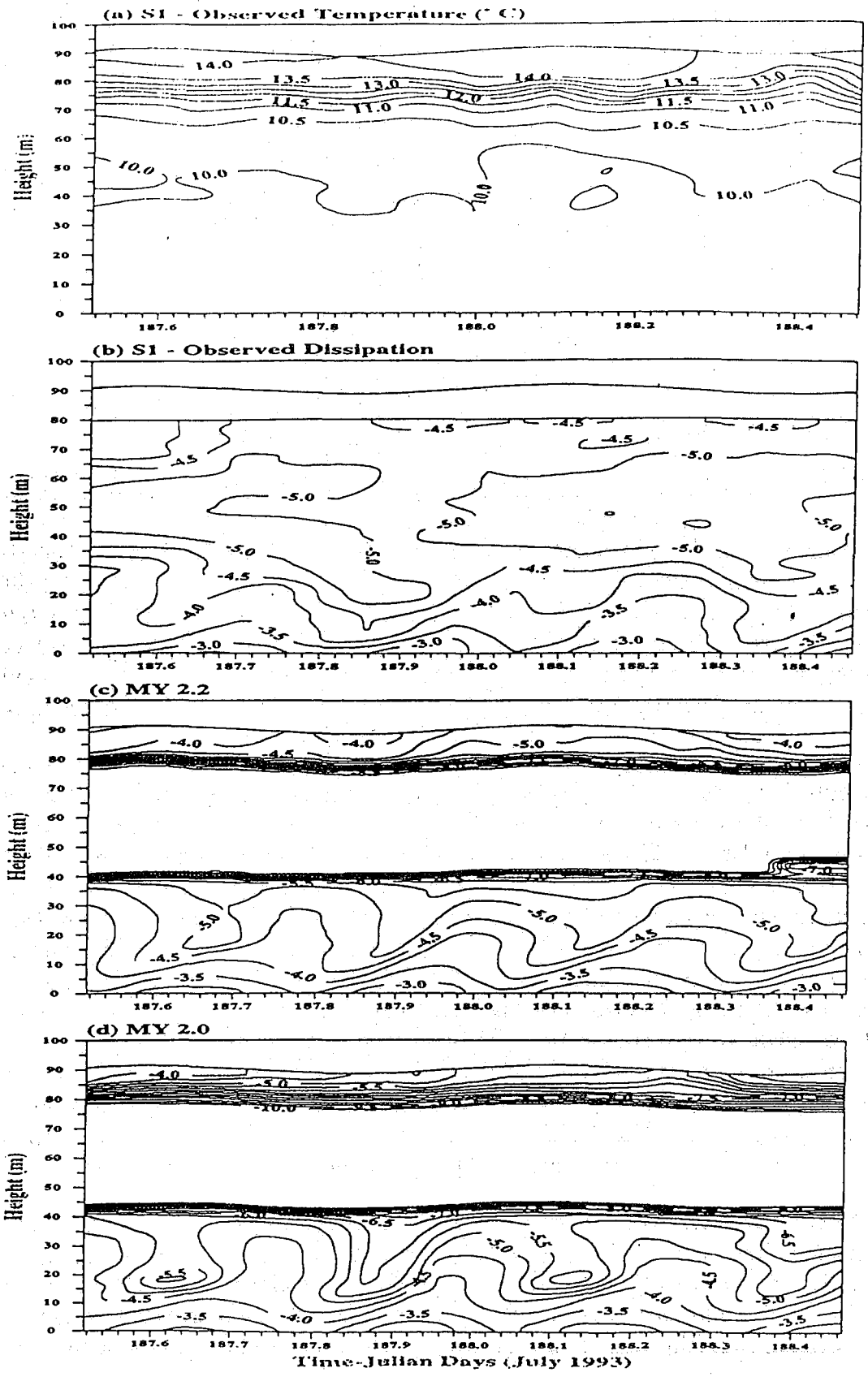
(a) S1 - Observed Temperature (° C)
(b) S1 - Observed Dissipation
(c) MY 2.2
(d) MY 2.0
Height (m)
Time-Julian Days (July 1993)

Figure 2.

OIL SPILLS IN OPEN AND ICE-INFESTED WATERS: A COMPARATIVE NEED FOR DATA ON WATER CURRENTS

S. Venkatesh
Atmospheric Environment Service
4905 Dufferin Street
Downsview, Ontario M3H 5T4

Spread and Drift of Oil in Open and Ice-infested Waters

When oil is spilled on water, it spreads to a thin film with thickness of the order of a few micro-meters. The spreading behaviour of oil on open water has been described by Fay (1969). If the air and water temperatures are warm enough (>15°C), then the spreading behaviour is not very sensitive to the viscosity of the oil and is reflected in the formulations developped by Fay. In an uncontained oil spill in open waters the oil spreads over a rather large area. Depending on this areal extent different portions of the slick will be subject to non-uniform meteorological and oceanographic influences. The water currents, in particular, can vary over short distances and can have a significant impact on the drift of the oil slick.

In ice-infested waters the spreading of spilled oil is very much dependent on the type and concentration of ice in the vicinity of the spill (Venkatesh et al., 1990). In near-freezing waters the mean thickness of the oil can be two to four times that in warmer waters. In particle (slush) ice the oil thickness is further enhanced by a factor of four. Thus for a given volume of oil the areal spread can vary by a factor of 8-16 depending on whether the spill occurs in warm water or in cold water with slush ice present. The spread of oil can also be affected by ice concentration. Greater the ice concentration, greater is the oil contaminated area. However, beyond an ice concentration of around 80% the ice floes are touching each other (see Venkatesh et al., 1990) and any newly spilt oil will be trapped between ice floes and may build to thicknesses as high as that of the ice floes themselves. Such trapping results in a dramatic reduction in the lateral spread of the oil. Under such ice concentration conditions, assuming ice thickness of 1 m, a 100000 m^3 spill can be trapped in an area as little as 0.15 km^2. As a comparison of the spill volume, the Exxon Valdez spill (Venkatesh (1990), Galt et al. (1991)) was about 40000 m^3 and the Braer spill (Spaulding et al., 1994) was 85000 m^3.

The large variations possible in the areal extent of spread of spilt oil necessitates the need for ice information on a rather fine scale. Present day SAR-derived ice data have a high enough resolution (down to 20 m) to provide the necessary details of the ice conditions in the vicinity of the spill. In the absence of such detailed satellite data in a timely manner, however, one will need to employ other means to collect such data, e.g., through aircraft reconnaissance.

With the large variations possible in the oil contaminated area for a given volume of oil spilled in ice-infested waters, the forces affecting the drift of the oil may not always be spatially uniform over the contaminated area. An additional problem to be dealt with for spills in ice-infested waters is the movement of oil trapped under the ice. Depending on the ice concentration and the roughness of the underside of the ice, large quantities of oil can be stored under the ice. From laboratory experiments it has been found that a certain minimum water current speed is required to pull the oil out of the cavities on the underside of the ice (Cox, 1980).

The Exxon Valdez and the Tenyo Maru Oil Spills - Sensitivity to Winds and Water Currents

In the previous section we have discussed the need for information on spatial variations in the meteorological and oceanographic data that affect the drift of an oil slick. This need is especially evident in the case of spills, from a stationary source, for extended periods of time so that the leading edge of oil is far from the spill source. In order to quantify the impact of spatial variations in the driving forces, particularly the water currents, one can examine the results from the model simulations of the *Exxon Valdez* and the *Tenyo Maru* oil spills. The details of the model used in these studies are given in Venkatesh (1988).

The *Exxon Valdez* oil spill occurred near Bligh Reef within Prince William Sound (PWS) on March 24, 1989 spilling nearly 11 million gallons of Alaskan crude oil. Figure 1 shows the distribution of residual water currents in PWS and the Gulf of Alaska. The Alaska coastal current hugging the coast line is an important feature that affects oil drift. Figure 2a and 2b show the model simulated drift of oil with and without the residual currents. Not only is the impact of the Alaska coastal current evident on spill motion, but also is the impact of the weak currents within PWS (see panels corresponding to 12 and 6 day movements respectively). The oil exits PWS much sooner with the currents included than without them. The wind effects are the same in both cases. Once the oil gets out into the Gulf of Alaska, it is pushed towards the coast by the coastal current. Without this coastal current the oil travels directly southward under the influence of only the winds. Other details of the model simulations can be found in Venkatesh (1990)

The *Tenyo Maru* oil spill which occurred on July 22, 1991 off the coast of Vancouver Island, has been examined in detail by Venkatesh and Crawford (1993). They found that the Tully eddy, a semi-permanent feature (induced by bathymetric features) in the area of the spill, had a very significant impact on spill motion. Figure 3 shows the water current features in the area of the spill. Figures 4a and 4b show the spill motion after 3 days from start of spill, with and without the residual water currents. Given that the winds were very light during the period of the spill, the spill motion was negligible when the residual currents were set to zero. This case clearly shows the need for a detailed knowledge of the spatial variations in the water currents over even a relatively small area as that covered by the *Tenyo Maru* oil spill.

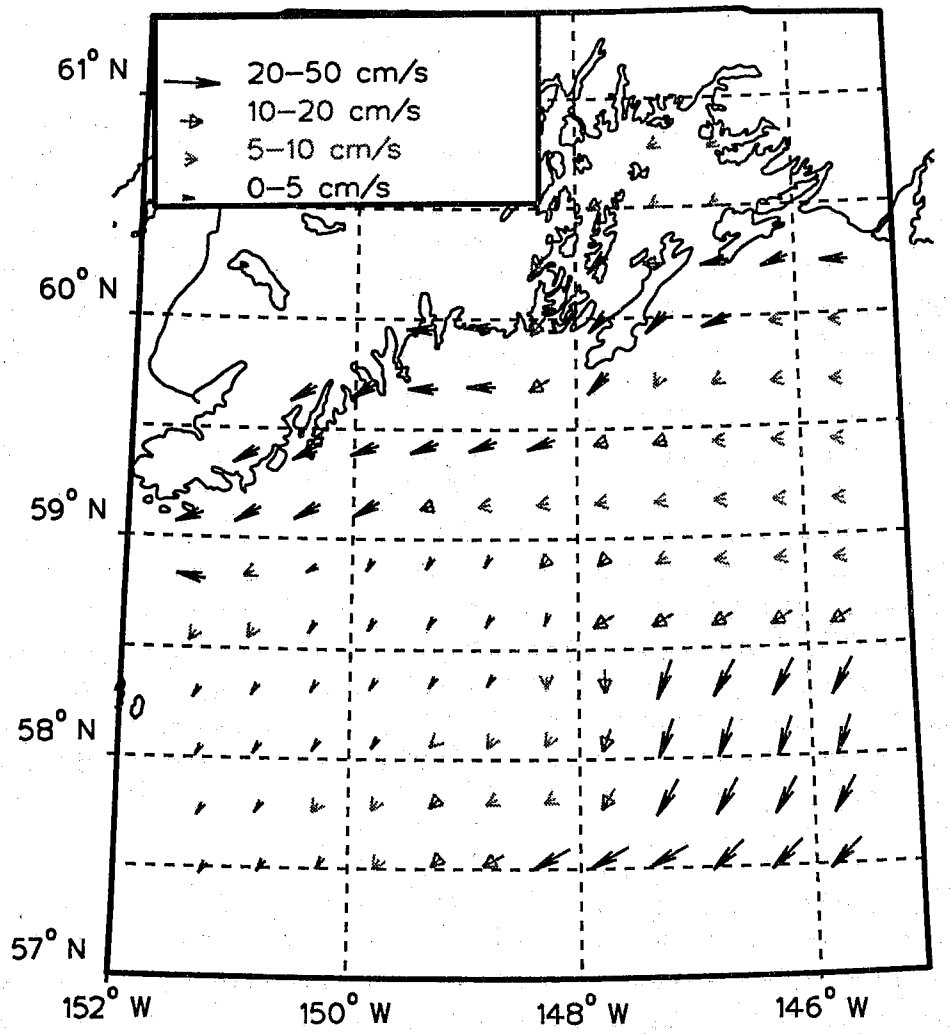

Figure 1: Residual currents used in the model simualtions of the *Exxon Valdez* oil spill.

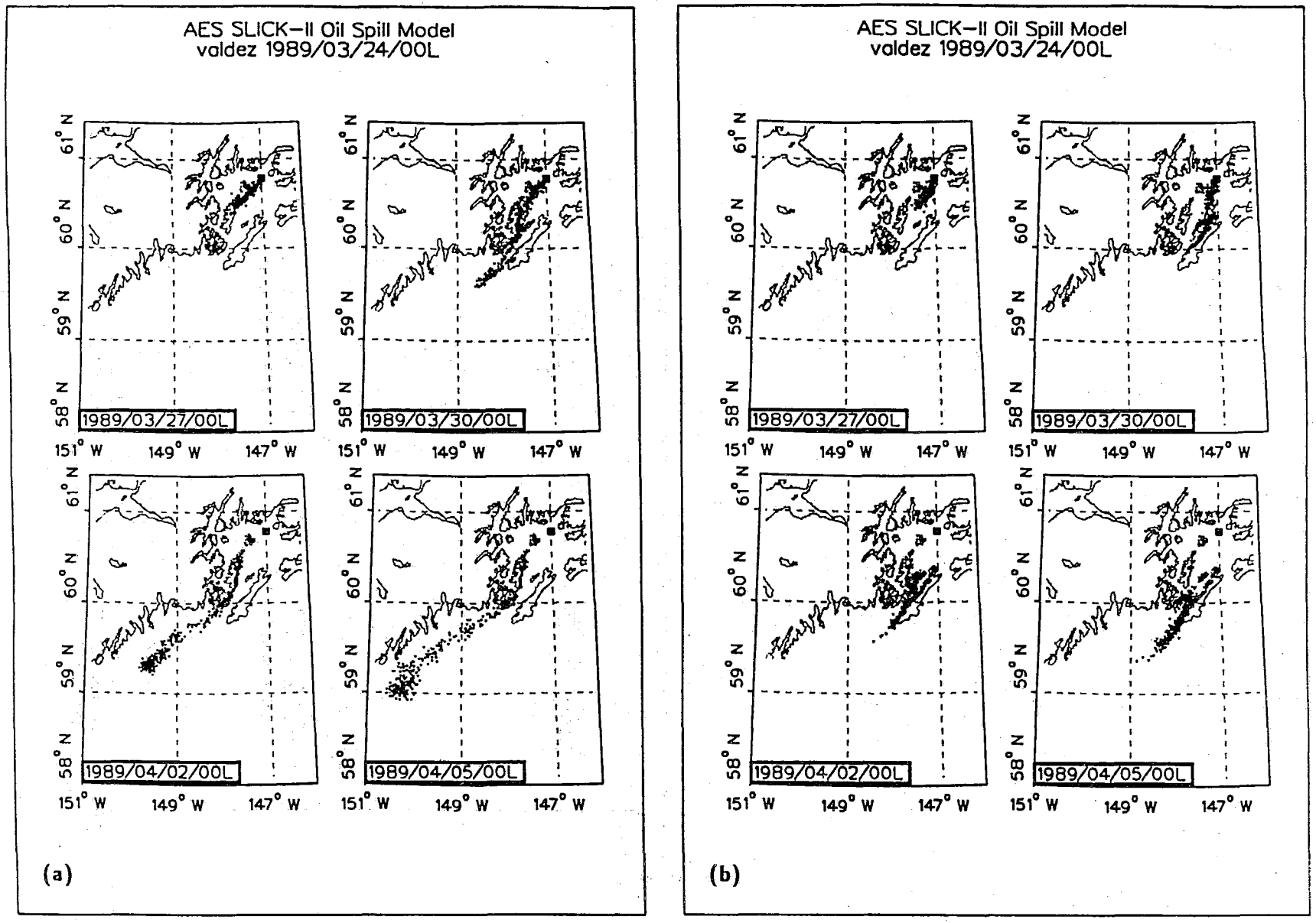

Figure 2: Model simulations of the *Exxon Valdez* oil spill with (Fig. 2a) and without (Fig. 2b) residual currents.

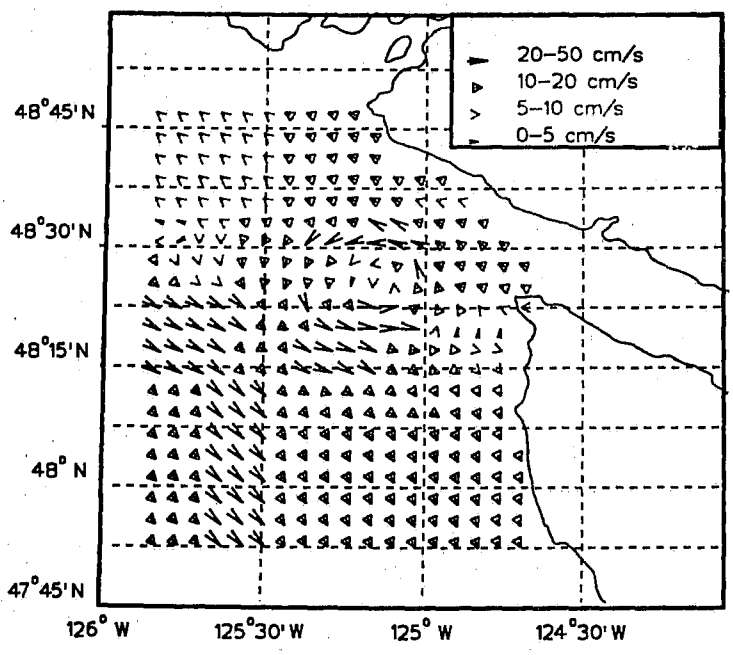

Figure 3: Residual currents in the vicinity of the *Tenyo Maru* oil spill.

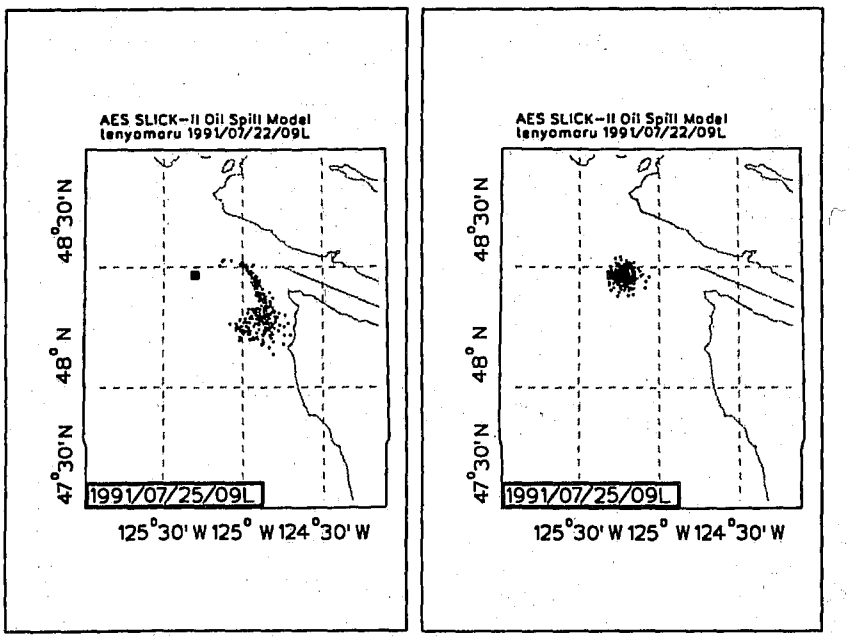

(a) **(b)**

Figure 4: Model simulations of the *Tenyo Maru* oil spill with (Fig. 4a) and without (Fig. 4b) residual currents.

Discussion

Given the higher oil thicknesses that can be expected in an oil spill in ice-infested waters than one in open warm waters, as much as a 16 fold difference in some specific situations, one can generally expect the oil contaminated area in a warm water spill to be larger than that for spills in ice-infested waters. Hence one can expect to have a greater need for a definition of spatial variations in the driving forces (wind and water currents) in the case of oil spills in open waters. But as has been noted in the *Tenyo Maru* case above, the spatial variations in water currents can be substantial even over relatively small distances.

In the case of spills in ice-infested waters, there may be many instances where the oil is embedded in or trapped between floes. Under these conditions the oil will move with the ice and detailed ice dynamics models can be utilized for describing the ice and hence oil movement.

References

Cox, J.C., 1980: "The transport and behaviour of oil spilled in and under sea ice". Arctec Inc., Rep. No. 460, Columbia, Md.

Fay, J.A., 1969: The spread of oil slicks on a calm sea. In: *Oil on the Sea*, D.P. Hoult (Ed.), Plenum Press, pp 53-63.

Galt, J.A., W.J. Lehr and D.L. Payton, 1991: "Fate and transport of the Exxon Valdez oil spill". Environ. Sci. Tech., Vol. 25, pp202-209.

Spaulding, M.L., V.S. Kolluru, E. Anderson and E. Howlett, 1994: "Application of three-dimensional oil spill model (WOSM/OILMAP) to hindcast the Braer spill". Spill Science and Technology Bull., Vol. 1, pp23-35.

Venkatesh, S., 1988: "The oil spill behaviour model of the Canadian Atmospheric Environment Service - Part I: Theory and model evaluation". ATMOSPHERE-OCEAN, Vol. 26, pp93-108.

Venkatesh, S., 1990: "Modelling the behaviour of oil spills in ice-infested waters". ATMOSPHERE-OCEAN, Vol. 28, pp303-329.

Venkatesh, S. and W.R. Crawford, 1993: "Spread of oil from the *Tenyo Maru*, off the southwest coast of Vancouver island". Natural Hazards, Vol. 8, pp75-91.

Venkatesh, S., M. El-Tahan, G. Comfort and R. Abdelnour, 1990: "Modelling the behaviour of oil spills in ice-infested waters". ATMOSPHERE-OCEAN. Vol. 28, pp303-329.

Tidally Forced Under-Ice Ekman Layers Observed by an Acoustic Doppler Current Profiler

R.F. Marsden *
R.G. Ingram †
F. Milinazzo ‡
A.G. Buckley ‡

* Physics Department
Royal Military College
Kingston, Ont.
Canada
K7K 5L0

† Department of Atmospheric and Oceanic Sciences
McGill University
805 Sherbrooke Street West
Montreal, Quebec
Canada
H3A 2K6

‡ Mathematics Department
Royal Roads Military College
FMO
Victoria, B.C.
Canada
V0S 1B0

Estimates of the turbulent transport of nutrients through the pycnocline to the ice–water interface are required to assess potential phytoplankton growth. Since the eddy diffusivity and eddy viscosity are essentially model parameterizations to account for sub-grid scale mixing described by the non-linear terms in the equations of motion, a common approach for their calculation has been to minimize differences between observations and model output. Maas and van Haren (1987), for example, use a simple tidally forced, constant eddy viscosity model which was fit 'by face value' to near-bottom current meter observations in the North Sea. Yu and O'Brien (1991) estimate the air–sea drag coefficient and oceanic eddy viscosity using data assimilation and a simple wind forced Ekman model.

Data assimilation techniques have assumed an increasingly important role as a mechanism for fitting model output to data. A cost function is normally defined as the squared differences between model output and measured data, and is minimized through the variation of model parameters such as eddy viscosity, drag coefficient (Yu and O'Brien, 1991), and internal wave phase speeds (Smedstad and O'Brien, 1991).

The primary purpose of this paper is to estimate directly the eddy diffusivity in order to determine the potential of the background tidal flow to mix nutrients to the ice–water interface. Estimates of the depth dependant M_2 and K_1 tidal contituents, produced from a harmonic analysis of ADCP data sampled through land-fast ice in the Canadian Arctic Archipelago, will be compared to a simple, tidally forced, Ekman model. The eddy viscosity, ice–water and bottom drag coefficients will be determined in a manner similar to that proposed by Maas and van Haren (1987). A novel feature of this paper is that the gradients of the cost function will be calculated directly from the model without having to resort to using Lagrangian multipliers.

Assuming a viscous, linear, barotropic fluid with orthogonal horizontal velocities $u(x,y,z,t)$ and $v(x,y,z,t)$, it can be shown for a harmonic time dependence (e.g. Maas and van Haren, 1987) that a complex horizontal velocity $w(x,y,z,t) = u(x,y,z,t) + iv(x,y,z,t)$ can be formed which satisfies

$$i(f \pm \omega)w^{\pm} - A_z \frac{\partial^2 w^{\pm}}{\partial z^2} = \alpha^{\pm} \qquad (1)$$

where w^+ and w^- are the counter-clockwise and clockwise rotating tidal constitutents respectively, f is the Coriolis parameter, $i = \sqrt{-1}$. $\alpha = -\frac{1}{\rho_*}(\frac{\partial p}{\partial x} - i\frac{\partial p}{\partial y})$ is the pressure gradient, and A_z is the eddy viscosity, both assumed to be independent of depth. Linearized 'slip' boundary conditions will be applied:

$$A_z \frac{\partial w^\pm}{\partial z} + C_{d1} w^\pm = 0 \quad \text{at} \quad z = 0 \tag{2a}$$

and

$$A_z \frac{\partial w^\pm}{\partial z} - C_{d2} w^\pm = 0 \quad \text{at} \quad z = -H \tag{2b}$$

where $C_{dj}, j = 1, 2$ are linearized drag coefficients, $z = 0$ is the ice–water interface and $z = -H$ is the bottom. The z axis is defined as positive upward from the ice–water interface. Two different drag coefficients were used, recognizing that the ice may present a smoother resistance to the flow than the bottom.

The model was cast in finite difference form with derivatives in the mesh approximated by centered differences, the surface boundary condition approximated by forward differences and the bottom boundary condition approximated by backward differences. The grid was 100 points spaced 0.5 m apart for the K_1 calculations and 1.35 m apart for the M_2 calculations, where the entire water column was modelled.

The drag coefficients C_{dj}, eddy viscosity A_z and pressure gradients $\alpha^\pm$ were fit to the data in a modified version of the technique outlined by Yu and O'Brien (1991). Consider a set of model output $w^\pm(z)$ and data values $\tilde{w}^\pm(z)$. We wish to minimize a cost function J defined as the squared differences between the model output and the data

$$J = \int_{-H_o}^{0} (w(z)^+ - \tilde{w}(z)^+)^*(w(z)^+ - \tilde{w}(z)^+) + (w(z)^- - \tilde{w}(z)^-)^*(w(z)^- - \tilde{w}(z)^-)dz \tag{3}$$

where * represent complex conjugation. The cost function can be expanded around an initial guess $J_0(A_{z0}, C_{d0}, \alpha_0^\pm)$

$$J(A_z, C_d, \alpha^\pm) = J_o(A_{z0}, C_{d0}) + \frac{\partial J}{\partial A_z}\delta A_z + \frac{\partial J}{\partial C_d}\delta C_d + \frac{\partial J}{\partial \alpha_x^\pm}\delta\alpha_x^\pm + \frac{\partial J}{\partial \alpha_y^\pm}\delta\alpha_y^\pm + \ldots \tag{4}$$

where $\alpha^\pm = \alpha_x^\pm + i\alpha_y^\pm$. Given accurate estimates of the partial derivatives of J, the control parameters can be updated until a sufficiently small improvement in the residual error is achieved, or until successive iterations result in small changes in their values.

For the implicit finite difference scheme used here, the gradients of the cost function can be calculated directly from the variational problem. For example, the gradient with respect to A_z is evaluated as

$$\frac{\partial J}{\partial A_z} = 2.0 * Re \int_{-H_o}^{0} (w^+(z) - \tilde{w}^+(z))^* \frac{\partial w^+}{\partial A_z} + (w^-(z) - \tilde{w}^-(z))^* \frac{\partial w^-}{\partial A_z} dz \tag{5}$$

The variational problems for the derivatives of $w^\pm$ with respect to the control parameters are obtained by differentiating eqs 1 and 2 with respect to each of the control parameters. Expressed in terms of the differential operator $D^\pm = i(f \pm w) - A_z \frac{\partial^2}{\partial z^2}$, the result is

$$D^\pm w_\Gamma^\pm = \begin{cases} \frac{\partial^2 w^\pm}{\partial z^2} & \Gamma = A_z, \\ 0 & \Gamma = C_{dj}, \\ 1 & \Gamma = \alpha_x^\pm, \\ i & \Gamma = \alpha_y^\pm, \end{cases} \tag{6}$$

with boundary conditions

$$A_z \frac{\partial w_\Gamma^\pm(0)}{\partial z} + C_{d1} w_\Gamma^\pm(0) = \begin{cases} -\frac{\partial w^\pm(0)}{\partial z} & \Gamma = A_z, \\ -w^\pm(0) & \Gamma = C_{d1}, \\ 0 & \Gamma = C_{d2}, \alpha_x^\pm, \alpha_y^\pm, \end{cases} \tag{7a}$$

and

$$A_z \frac{\partial w_\Gamma^\pm(-H)}{\partial z} - C_{d2} w_\Gamma^\pm(-H) = \begin{cases} -\frac{\partial w^\pm(-H)}{\partial z} & \Gamma = A_z, \\ -w^\pm(-H) & \Gamma = C_{d2}, \\ 0 & \Gamma = C_{d1}, \alpha_x^\pm, \alpha_y^\pm, \end{cases} \tag{7b}$$

where the subscript Γ denotes partial differentiation with respect to the control variables.

The differentiated governing equations and boundary conditions can now be solved. When recast in implicit finite difference form, all the variates, including w and its derivatives with respect to the control parameters, obey tridiagonal systems given by

$$\mathbf{A}\vec{x} = \vec{r} \tag{8}$$

which require solution. In order to perform the required minimizations, the BBVSCG algorithm of Buckley and LeNir (1985), as revised by Buckley (1989), was used.

Harmonic analysis of the entire data set showed that the K_1 and M_2 tidal constituents were of nearly identical amplitude (10–14 cm s^{-1}). A Fourier transform of the vertical velocities indicated that the K_1 component is barotropic while the M_2 component has a depth dependent pressure gradient, not modeled in this study. During the first 15 sampling days, CTD casts indicated a sharp pycnocline between 10 and 20 m depth. In the second 15 days of sampling (after 5 May), the pycnocline was no longer evident. Consequently, the data were partitioned into two 15-day groups which will be referred to as period I, from 21 Apr–5 May, 1992 and period II, from 5–20 May. The ADCP sampled in 2-min intervals and at 2-m depth increments from 3 to 53 m. A harmonic analysis, based on Foreman (1979), was calculated for the horizontal velocities at each depth, separately on each 15-day period. The model was then fit to the rotary amplitudes and phases.

The data complex rotary velocity components obtained from the harmonic analysis were spline fit and interpolated to 0.5-m increments for the K_1 component and to 1.35-m increments for the M_2 component to match the model grid. Six parameters were fit for K_1 (A_z, C_{d1}, and the real and imaginary components of $\alpha^\pm$) and seven parameters for M_2 (same as K_1 with the addition of C_{d2}).

Figure 1 shows the results for the K_1 constituent for period I, when a strong pycnocline between 10 to 20 m depth was present. The solid line represents the interpolated data, the dashed line the model initial guess and the dot-dashed line the iterated model solution. The model appears to represent the data quite accurately in the top 10 m of the water column for both amplitude and phase in both the counter-clockwise and clockwise solutions.

Figure 2 shows the fit for the M_2 component for period II. Overall, the counter-clockwise amplitude and phase and the clockwise amplitude fit the data reasonably well. In no instance were the model clockwise phases in agreement with the data. The poorest fit is for period I when the water column was stratified. Table I indicates a larger eddy viscosity during the stratified period than during the unstratified period, in disagreement with the results from the analysis of the diurnal constituents and contrary to expectations.

Overall, the fitting procedure proved to be marginally successful. The reduction in amplitude and phase lead approaching the ice–water interface was well reproduced for both components of the K_1 and the counter-clockwise component of the M_2 tide. The variation in amplitude was well reproduced for the clockwise component of the M_2 tide. However, the model clockwise phase, nearly constant with depth,

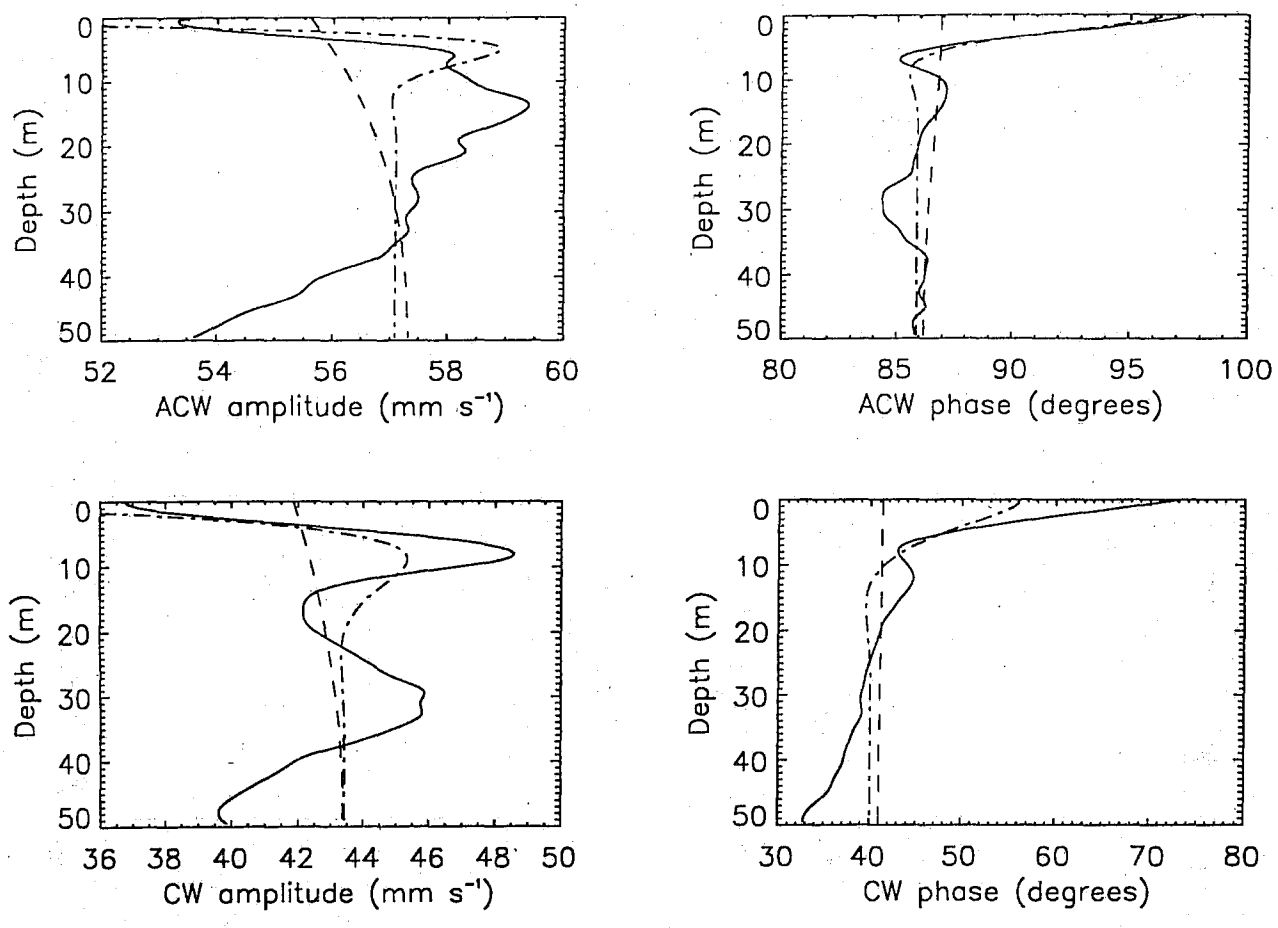

Figure 1. Results of the data assimilation for the K_1 tide for period I (21 Apr to 5 May 1992). The solid line is the data interpolated from the 2 m sampling increments to the model grid. The dashed line is the initial guess, described in the text, while the dashed-dot line is the iterated least squares solution.

disagreed with the data phase, which showed considerable variability. Paquet (1993) shows that the semi-diurnal band of the power spectra of the vertical velocity was above the noise level, suggesting that the pressure gradient may have some vertical dependence, not considered in this analysis. This is further supported by anomalous results in eddy viscosity and drag coefficient for the M_2 frequency. Whereas the K_1 component showed the the expected increase in A_z during the second, unstratified period, the value for M_2 did not change between periods.

Marsden *et al.* (1994) assert that the major portion of the mixing in Resolute Passage was due to the frequent initiation of turbulence associated with the passage of high frequency internal waves and that 'During quiescent periods (i.e. in the absence of high frequency waves), the background tidal velocities were not large enough to induce shear instabilities across the pycnocline, essential to promote mixing ...'. This assertion is supported by the present results. Table I indicates that the maximum in A_z due to background tidal mixing is 4.75×10^{-3} m^2 s^{-1}. Turner (1973) gives the relation between K_z, the eddy diffusivity, and A_z to be

$$K_z = \left(\frac{R_f}{R_i}\right) A_z$$

where R_f and R_i are the flux and gradient Richardson numbers respectively. Britter (1974) suggests critical values of R_f of 0.18–0.20 for sustained turbulence, while Marsden *et al.* (1994) show that R_i is only sporadically < 0.25. Consequently, a maximum inferred value of K_z is about 3.8×10^{-3} m^2 s^{-1}. Using a maximum nutrient gradient indicated in Cota *et al.* (1987) of 0.3 mmol m^{-4}, when integrated

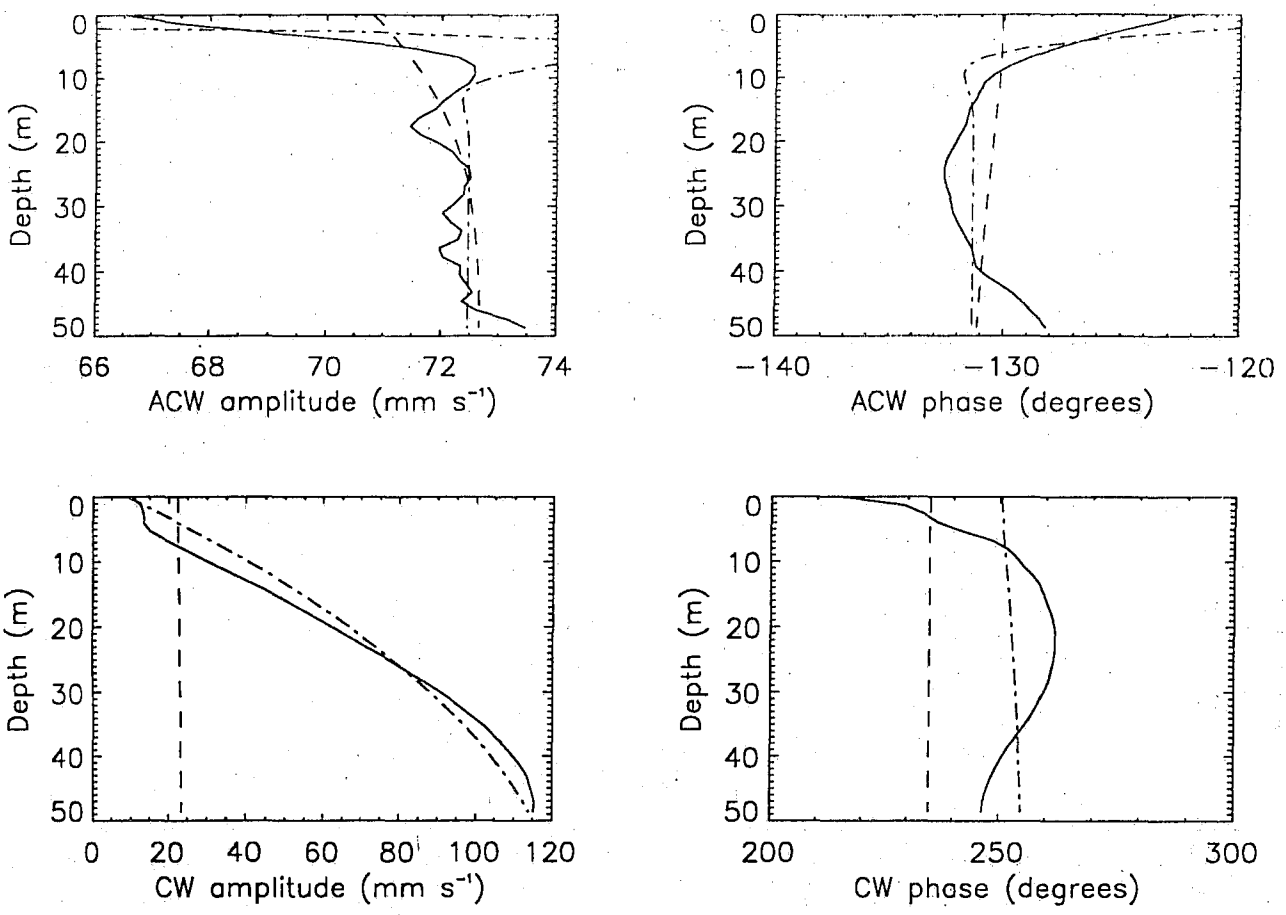

Figure 2. Same as Figure 1 for the M_2 tide for period II.

over a 60-day period gives a total flux of 0.6 mmol m^{-2} due to the average background tide. This is a factor of 50 less than the total nutrient requirements outlined by Cota *et al.* (1987), and a factor of 10 less than the flux inferred from turbulence associated with the passage of high frequency internal waves, discussed in Marsden *et al.* (1994). We must conclude that the mixing associated with the passage of high frequency internal waves is more important in supplying the ice–algae community with nutrients than mixing associated with the background tidal velocities.

Table 1. Results of the data assimilation. Period I is from 21 Apr to 5 May, 1992 while period II is from 5 May to 20 May, 1992. J is the cost function, A_z is the eddy viscosity while C_{d1} and C_{d2} are the drag coefficients at the ice–water interface and at the bottom respectively.

Constituent	Period	J $\times 10^{-3}$ $m^2 s^{-2}$	A_z $\times 10^{-3}$ m^2 s^{-1}	C_{d1} $\times 10^{-4}$ m s^{-1}	C_{d2} $\times 10^{-4}$ m s^{-1}
K_1	I	1.78	0.76	1.35	
K_1	II	2.72	4.75	2.80	
M_2	I	4.58	2.61	0.15	9.26
M_2	II	4.96	1.40	4.01	1.65

References

Britter, R.E., 1974. An Experiment on Turbulence in a Density-stratified Fluid. PhD. thesis, Monash University, Victoria, Austrialia.

Buckley, A.G., 1989. Remark on algorithm 630. *ACM Transactions on Mathematical Software*, 15, 262–274.

—, and A. Lenir, 1985. Algorithm 630, BBVSCG - A variable-storage algorithm for function minimization. *ACM Transaction on Mathematical Software*, 11, 105–119.

Cota, G.F., S.J. Prinsenberg, E.B. Bennett, J.W. Loder, M.R. Lewis, J.L. Anning, N.H.F. Watson and L.R. Harris, 1987. Nutrient fluxes during extended blooms of Arctic ice algae. *J. Geophys. Res.*, 92, 1951–1962.

Foreman, M.G.G., 1979. Manual for Tidal Currents Analysis and Prediction. Pacific Marine Science Report 78-6. Institute of Ocean Sciences, Sidney, B.C., 70 pp.

Maas, L.R.M. and J.J.M. van Haren, 1987. Observations on the vertical structure of tidal and inertial currents in the central North Sea. *J. Mar. Res.*, 45, 293–318.

Marsden, R.F., R.G. Ingram and L. Legendre, 1994. Currents under land-fast ice in the Canadian Arctic Archipelago: Part II: Vertical mixing. *J. Mar. Res.*, 52, 1037–1049.

Paquet J.R., 1993. Internal Solitary Waves with Acoustic Applications to the Canadian Arctic and the Scotian Shelf. M.Sc. thesis, Physics Department, Royal Roads Military College, 88 pp.

Smedstad, O.M. and J.J. O'Brien, 1991. Variational data assimilation and parameter estimation in an equatorial Pacific Ocean model. *Prog. Oceanogr.*, 26, 179–241.

Turner, J.S., 1973. *Buoyancy Effects in Fluids.* Cambridge Monographs on Mechanics and Applied Mathematics, Cambridge. 368 pp.

Yu, L. and J.J. O'Brien, 1991. Variational estimation of the wind stress drag coefficient and the oceanic eddy viscosity profile. *J. Phys. Oceanogr.*, 21, 709–719.

Vertical Structure of the Currents on the Newfoundland Shelf

by

S. Narayanan, E. Colbourne and J. Helbig

Physical Oceanography, Dept. of Fisheries and Oceans,
Northwest Atlantic Fisheries Centre
St. John's, NF, A1C 5X1

Abstract

Computer models used for ice and iceberg forecast, and oil spill trajectory simulation require realistic near-surface currents as input. The water currents data set mostly used for such studies on the Newfoundland and Labrador shelves was originally compiled by the International Ice Patrol (IIP) from drifter tracks and later modified to include more recent drifter information and limited amount of sub-surface currents data from moored instruments. Since 1991, vessel-mounted acoustic Doppler current profilers (ADCP) were used to collect velocity profiles from the continental shelves off Newfoundland and southern Labrador (Fig. 1) as part of the physical oceanographic components of cod ecosystem research under the Northern Cod Science Program (NCSP). This program also supported an extensive mooring program which provided velocity time series from a number of locations and depths over the same time period. These data sets will greatly enhance the spatial and temporal resolution of the current estimates thus providing a better understanding of the vertical structure of the currents over large spatial areas on the continental shelf.

The ADCPs were manufactured by the RD Instruments of San Diego, California USA. Each unit employs four acoustic transducers mounted at an angle of 30° to the vertical and 90° in the azimuth. The transducer assembly is either mounted on the hull of the vessel or on an over-the-side boom installed on the deck (Table 1). Water velocities are determined by measuring the Doppler shift of the backscattered portion of the transmitted acoustic pulse from each transducer, range gated into a maximum of 128 depth bins of selectable thickness. The pinging frequency is about 1 hz, however the acquisition software combines the backscattered signals into ensembles from a pre-selected number of pings to provide better estimates of the water velocity, usually 5 minutes. Typically, reliable velocities

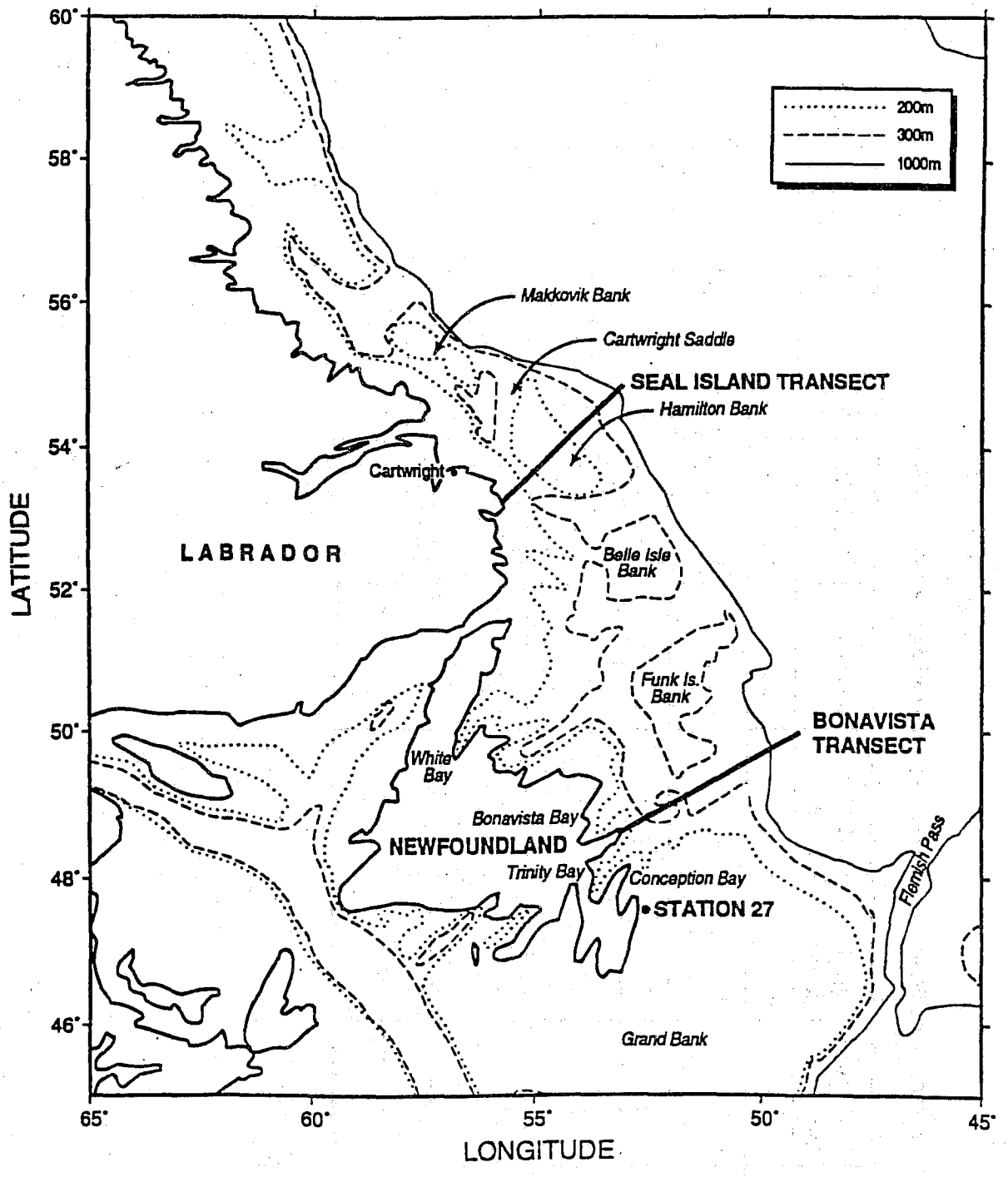

Fig. 1. Location map of the study area showing the position of standard Bonavista transect.

Table 1. ADCP deployment specifications on the vessels operating off the east coast of Canada.

Vessel	Size & draft (m)	Speed (knots)	ADCP model	Mounting	Freq. (Khz)	Profile range	Max bottom track depth	Survey period	Area
Shammok	22, 3.3	8	NB	boom[1]	153.4	6-300 m	500 m	90-94	CB
Lady Hamoond	58, 5	7	NB	boom[1]	153.4	9-300 m	500 m	91-92	shelf
Parizeau	65, 4.6	12	NB	hull	153.4	9-300 m	700 m	91-	shelf
Hudson	90, 6.3	12	NB	hull	153.4	10-300	700 m	93-96	shelf
Teleost[2]		10	BB	hull	153.4	14-280 m	500 m	95-	shelf
Petrel V	59, 5	9	NB	hull	300	9-280 m	400 m	93	shelf

[1] Colbourne et al. (1993)
[2] under evaluation

can be estimated from the second bin from the body of the vessel, to 85% of the water column or to the nominal range which is dependent on the frequency of the transducer, which ever is the lowest. The measured velocities are relative to the platform and on the continental shelf are compensated for by subtracting the velocity of the vessel which is determined by accurately measuring the speed of the vessel over ground by a separate, high intensity, bottom tracking signal. The orientation of the currents and geographical locations are determined from the ship's gyro compass and GPS systems.

Several factors influence the ADCP data quality and depth range, such as the operating frequency, water depth in the survey area, deployment mode (boom-mounted vs hull-mounted), and vessel specifications. For the data collected in the Newfoundland region some of these factors are summarized in Table 1. To process, quality control and archive this large data set in a semi-automated mode we are implementing an archival and processing software package based on the Common Oceanographic Data Access System (CODAS) developed by the University of Hawaii. So far a total of 22 cruises were quality controlled and archived (Fig. 2) using this package.

Earlier studies using a sub-set of this data have shown that the ADCP data can be quite useful to describe aspects of the mean circulation both on the shelf and in the inshore regions (Colbourne et al., 1995, Colbourne et al., 1993). Current measurements made from moving vessels using ADCPs include high frequency components, eddies, tides etc., the removal of which does not lend itself to simple harmonic analysis. An inspection of the M_2 tidal constituent from moored current meter data indicates however that the tides are weak on the Newfoundland Shelf generally less than 6.0 cm/s (Narayanan, 1994), which is small compared to the energetic Labrador current. To suppress some of the high frequency energy and to determine the mean flow we averaged about 50 along-shelf (-30° from north) transects along the east coast of Newfoundland within about 30 minutes of latitude of the standard Bonavista transect (Fig. 1). The current field revealed by this analysis show a broad inshore branch of the Labrador current with speeds ranging from 5 to 10 cm/s. The offshore branch is clearly evident near the edge of the continental shelf with average speeds over 20 cm/s in the upper layers (Fig. 3) (Colbourne et al., 1995). Comparison between the fixed current meter and ADCP measurements in the offshore and mid-shelf areas show good agreement, however they differ by a factor of 2 nearshore where the fixed current meter measurements are higher than the averaged ADCP measurements.

A typical profile of the vertical structure in the offshore branch of the Labrador current near the edge of the continental shelf is shown in Figure 4. This profile was acquired while station keeping for about 0.5 hours during a CTD cast. The error bars are ± 1 standard deviation of 5 minute ensembles. This short time scale profile shows a much stronger current compared to that shown in Figure 3 but is nevertheless representative of the current structure in the offshore regions. The profile shows a strong SSE current of the order of 40 to 50 ± 5 cm/s near the surface with significant shear in the upper layer (100 m depth). The current decreases to approximately 20 cm/s at about 300 m depth, the maximum range of the ADCP.

Work is underway to further examine this extensive data set to delineate the vertical structure of the circulation on the continental shelf along the east coast of Newfoundland at different time scales. In addition, the near-surface circulation deduced from this analysis will be compared with the current map for the same area compiled by the International Ice Patrol, and with the surface currents deduced from the drifter tracks collected under NCSP.

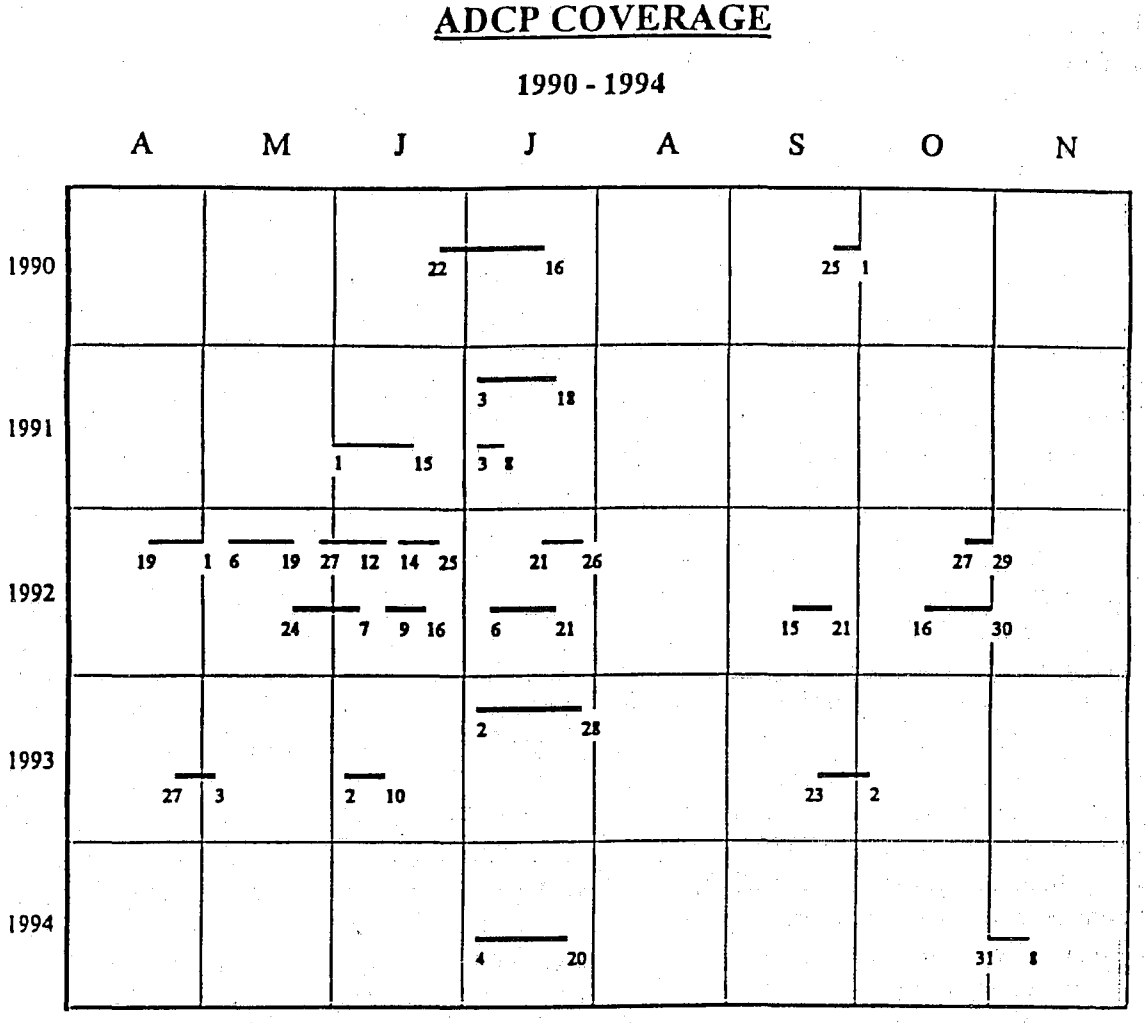

Fig. 2. The ADCP survey periods.

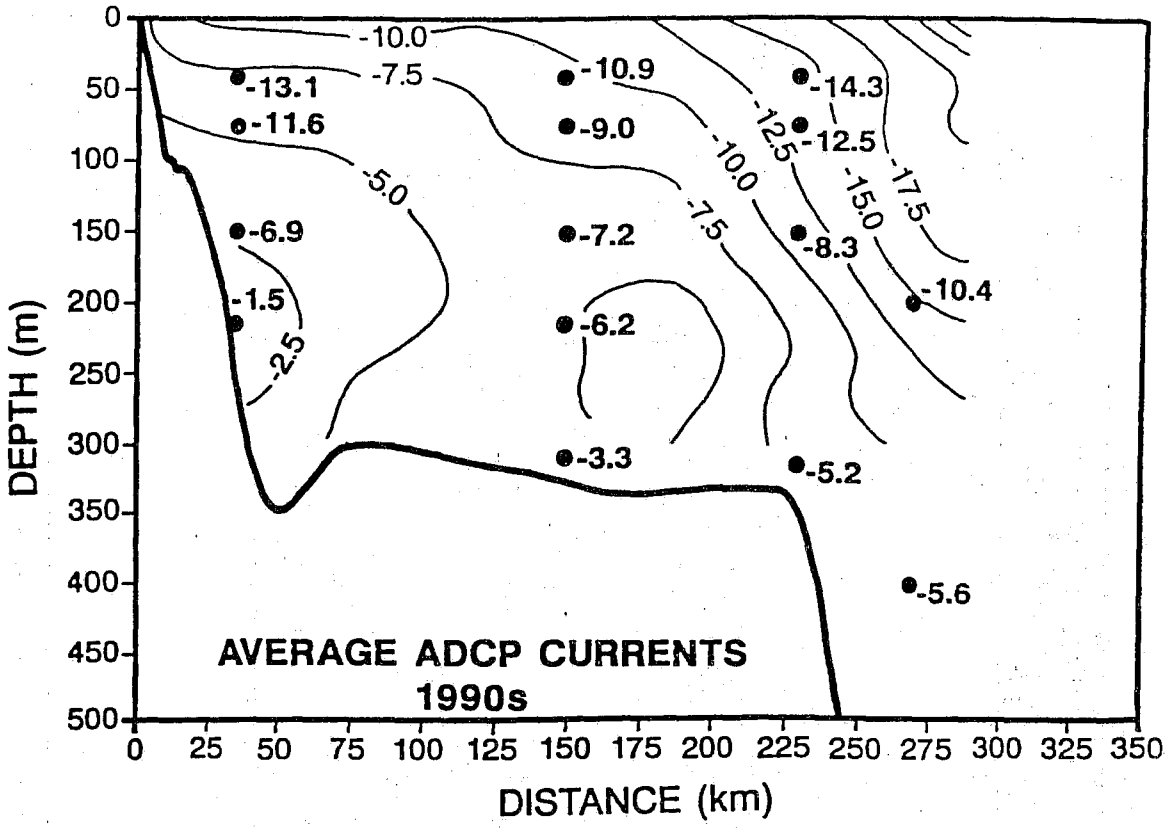

Fig. 3. The average current field derived from about 50 bottom tracked ADCP transects collected within about 30° latitude of the standard Bonavista transect between 1991-1993 with the current meter measurements superimposed (from Colbourne et al., 1995).

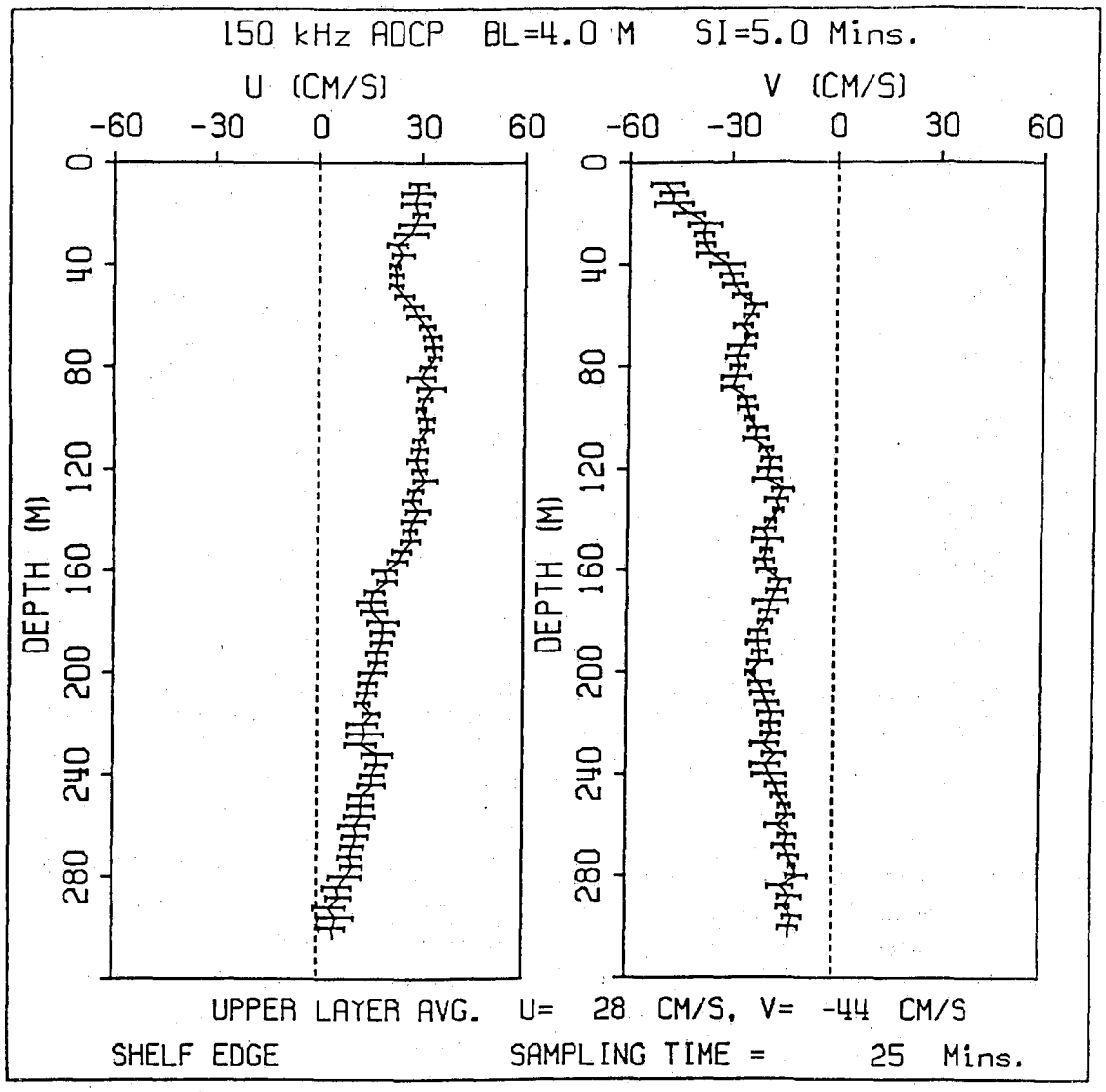

Fig. 4. Vertical profile of the u and v components of the offshore branch of the Labrador current.

REFERENCES

Colbourne, E. B., J. Helbig, and D. Cumming. 1993. Improved ADCP Performance Using a Hydrodynamically Designed Boom Mount. J. of Atmospheric and Oceanic Technology, Vol. 10, No.4. pp 629-636.

Colbourne, E., deYoung, B., Narayanan, S. and J. Helbig. 1995. Mean Hydrography and Circulation on the Newfoundland Shelf. Can. J. Fish. Aquat. Sci. (submitted)

Narayanan, S. 1994. Current meter observations from Hamilton Bank and NE Newfoundland Shelf, 1990 to 1993. Can. Tech. Rep. Hydrogr. Ocean Sci. 157: v + 184 p.

Internal Wave Directional Spectra Using an Acoustic Doppler Current Profiler

R.F. Marsden *,B.-A. Juszko †, R.G. Ingram ‡

* Physics Department, Royal Roads Military College, FMO, Victoria, B.C., V0S 1B0; † Juszko Scientific Services, 127 Cliff Dr. RR#4, Victoria, B.C., V9B 5T8; ‡ Department of Atmospheric and Oceanic Sciences, McGill University, 805 Sherbrooke Street West, Montreal, Quebec, H3A 2K6.

1. Introduction

Longuet-Higgins *et al.* (1963) first proposed that data from a buoy which measured surface displacement and wave slopes in the north and east directions, could be used to calculate surface gravity wave directional spectra. The technique offered the distinct advantage of producing wave direction information using a single sensor, rather than the multi-element array normally required to measure two dimensional wavenumber spectra.

The acoustic Doppler current profiler (ADCP) has taken an increasingly important role in the detection of internal waves and currents. Greenwood *et al.* (1993) showed that ship motion greatly decreased the signal-to-noise ratio and suggested that if the ADCP were mounted on a stable platform, marked improvement in instrument performance could be achieved. In April and May 1992, a 614 kHz ADCP was deployed through landfast ice near Resolute, Northwest Territories in the Canadian Archipelago (see Figure 1) as part of a joint Canadian-Japanese investigation of factors that control ice algal growth and related processes. Initial results were reported in Marsden *et al.* (1994) (henceforth MPI). They showed that the low theoretical noise levels advertised by the manufacturer were not exceeded, allowing for the detection of vertical velocities. For the mean, at tidal frequencies and at high frequencies (periods < 1 hr), MPI showed that the platform was stable and correctly aligned in the vertical, ensuring an accurate vertical velocity measurement. The high frequency velocity response was classified as either internal waves, occurring during neap tides, or internal solitons, occurring during spring tides.

A general technique for the calculation of internal wave directional spectra was presented initially by Schott and Willebrand (1973) (henceforth SW) and applied specifically to the internal tide. Where SW prescribes the directional distribution to be a $\cos^{2p}$ function, we use the high resolution techniques of surface gravity wave measurement theory to allow the data to determine the form of the directional distribution. Marsden and Juszko (1987) explicitly show that their eigenvector technique automatically allows for the detection of multi-directional waves and that, for surface gravity waves, the $\cos^{2p}(\frac{\theta}{2})$ distribution results in unacceptably large errors in the recalculation of the data cross-spectral matrix.

Between 1200 and 2200 on 24 April 1992 more than 30 oscillations in the vertical velocity, highly trapped to the pycnocline, having periods of 10 to 20 min with a 4 h modulation in wave amplitude were detected. We will show that, assuming linearity, the three velocity components recorded by the ADCP can be recast in terms of a pressure anomaly fluctuation which is analogous to the surface displacement and slope of the heave, pitch and roll buoy, permitting calculation of data adaptive internal wave directional spectra.

2. Theory

Let the measured wave amplitudes and slopes of a surface gravity wave field be described as $\eta_i(t)$ for $i = (1, 2, 3)$ where $i = 1$ is the surface displacement (η) from the undisturbed state, $i = 2$ is the east slope (η_x) and $i = 3$ is the north slope (η_y). Marsden and Juszko (1987) show that the eigenvector directional spectral estimate ($\mathbf{E}(\theta)$) is given by

$$\mathbf{E}(\theta) = \frac{1}{\sum_{m=2}^{3} \frac{1}{\lambda_m} |\vec{\beta} \cdot \vec{\phi^m}|^2} \tag{1}$$

where $\beta = (1, ik\cos\theta, ik\sin\theta)$, while λ and ϕ are the eigenvalues and eigenvectors of the cross-spectral matrix respectively.

For a linear, Boussinesq, irrotational and inviscid fluid, Leblond and Mysak (1979) show that the horizontal dependence in horizontal velocity can be separated to give

$$\tilde{u}_n(x,y) = \frac{\tilde{p}_n(x,y)_x}{\rho_*}$$

$$\tilde{v}_n(x,y) = \frac{\tilde{p}_n(x,y)_y}{\rho_*} \tag{2}$$

while the horizontal dependence in the vertical velocity is given by

$$\frac{\tilde{w}_n(x,y)}{k_n} = \frac{\tilde{p}_n(x,y)}{\rho_*} \tag{3}$$

In analogy with surface gravity wave theory, an internal wave data cross-spectral matrix can be formed where the pressure anomaly assumes the role of the surface displacement.

Following Long (1980), the wavenumber within each frequency band was estimated from the data as

$$k_{exp} = \sqrt{(\frac{\hat{C}o_{22} + \hat{C}o_{33}}{\hat{C}o_{11}})} \tag{4}$$

where k_{exp} is an experimental wavenumber and $\hat{C}o_{22}, \hat{C}o_{22}$ and $\hat{C}o_{33}$ are the spectral power densities of the displacement and two slope signals respectively. This recognizes the possibility that the effective wavenumber may differ from the theoretical value due to Doppler shifting and non-linear effects. For surface gravity waves, k_{exp} was found to give more stable estimates of the directional spectra than from those obtained through inversion of the dispersion relation. Since these effects are expected to be more severe for the slower internal waves, k_{exp} will also be used in this study.

3. Data Collection and Analysis

The study took place from 21 April to 25 May 1992 at 74°41.19′ N 95° 15.59′ W, approximately 10 km southeast of the village of Resolute Bay on land-fast ice in Resolute Passage. The water was 135 m deep and the ice was 1.8 m thick. A 1.2 m by 1.8 m hole was cut through the ice to allow for the deployment of equipment including an ADCP and a Conductivity, Temperature and Depth (CTD) probe. An insulated tent was erected over the hole and was kept at approximately 20° C for the duration of the study. The transducer head from our RDI VM 614 kHz ADCP was attached to a 2.5 m steel pole 10 cm in diameter and suspended from a steel frame through the center of the deployment hole. The assembly head was mounted parallel to the bottom of the ice and the pole was set to plumb using a carpenter's level.

Calculation of the directional spectrum was performed in four steps. First, MPI showed that there existed significant spectral power density in the vertical velocities only for frequencies less than 3.0×10^{-3} Hz. Consequently, it was decided to divide the data record into 9 ensembles of 32 data points each, giving a bandwidth of 2.6×10^{-4} Hz and 18 degrees of freedom for the calculation of spectral power densities and only the lowest 12 frequencies (2.6×10^{-4} to 3.12×10^{-3} Hz) were examined. Second, the vertical and horizontal dynamic modes and phase speeds were calculated and stored. Third, the fast Fourier transforms for the three velocity components at each depth were calculated, fit in the vertical to determine $\frac{\tilde{p}_n(x,y)}{\rho_*}$ (eq 3), $\frac{\tilde{p}_n(x,y)_x}{\rho_*}$ and $\frac{\tilde{p}_n(x,y)_y}{\rho_*}$ (eq 2) and then ensemble averaged to obtain modal cross-spectral matrices. Finally, the directional spectra for each mode and associated errors were calculated following the technique outlined in Marsden and Juszko (1987) for surface gravity waves.

The data and model spectral power density functions were calculated and compared to ensure that the fitting process was replicating the data in a reasonable fashion. The agreement is quite good except for the two lowest frequency bands ($< 5.2 \times 10^{-4}$ Hz). The cross-channel velocity (u) spectrum has maxima at 7 m depth and 1.0×10^{-3} Hz and at 3 m depth and 1.5×10^{-3} Hz. The along-channel velocity (v) spectrum has approximately one-half the power of that for u and shows a

broad maximum at 7 m depth between 7.0×10^{-4} and 2.0×10^{-3} Hz. The vertical velocity in both spectra show maxima from 10 to 20 m from 7.0×10^{-4} to 2.0×10^{-3} Hz.

Although the spectra were calculated in terms of the pressure anomaly, they were normalized to the more meaningful modal kinetic energy densities shown in Figure 2 under the assumption that the pressure and energy energy shared the same directional distribution. There is very little change in propagation direction with frequency and most of the energy is directed toward 240° to 300° or southwest across the channel, indicated by the arrows in Figure 1. Mode 1 has an intense peak at 1.5×10^{-3} Hz with a smaller peak at 7.3×10^{-4} Hz. Mode 2 shows two sharp peaks at 1.5×10^{-3} and 2.3×10^{-3} Hz with a third smaller peak at 1.0×10^{-4} Hz.

For surface gravity waves, the velocity field from surface currents and low frequency waves can Doppler shift the wave field in the high frequency wind-driven portion of the spectrum. The existance of a Doppler shifting can be verified by examining the ratio of experimental to theoretical wavenumber. The ratio was systematically greater than 1.0 for all but the lowest two frequency bands. Agreement was obtained by correcting the spectra for 3 cm s^{-1} Doppler shifted current in the wave direction.

An examination of the lowest two frequency bands indicated a mismatch between the model and data spectra as well as inordinately low ratios between the theoretical and experimental wavenumbers. An examination of the high pass filtered cross-channel velocity at the surface and at depth indicated that at 33 m there were three distinct pulses of water directed to the southwest, from the shelf on Allen Bay, which are clearly the source of these large spectral power densities. At 3 m there was an on-shelf flow corresponding to, but slightly time delayed from the first pulse detected at depth. There does not appear to be distinct surface flows corresponding to the second and third pulses at 33 m. The corresponding vertical velocities did not demonstrate these features. It was suggested that these could be pulses of water travelling along isopycnals due to salt excretion from Allen Bay.

4. Conclusions

We have demonstrated that, given reliable estimates of vertical velocities, and an internal wave field that can be described by linear dynamics, acoustic Doppler current profiler data can be recast in a form analogous to those obtained from a surface following, heave, pitch and roll buoy. We describe a method in which recent developments in data adaptive directional spectral techniques can be applied and high resolution spectra obtained for each of the significant vertical modes of propagation.

The technique, proposed here, has broader application than for the special condition of an ADCP deployed through landfast ice. It is directly applicable, within the limits of the linear theory, to any ADCP that is deployed in a fixed bottom-mounted configuration (i.e. not allowed to oscillate with the currents). Minor errors in vertical alignment could be compensated by internal pitch and roll measurements. It is expected that, in the future, direct measurements of the vertical velocity will be obtainable on a more regular basis as new 'broad band' ADCPs have an order of magnitude increase in signal-to-noise ratio. Our technique can also be readily extended to multi-element arrays. Assuming a sampling scheme sufficient to resolve all the vertical and horizontal modes, the Fourier coefficients are fit at all mooring locations, as described here, and the modal cross-spectral matrix is calculated based on all the (horizontal) separations between mooring sites. The directional vector $\vec{\beta}$ is then determined from the expected phase shifts of the velocity and surface displacements for a pure plane wave traveling in the look direction θ (see Davis and Regier, 1977).

Another objective of the study was to use the ADCP results to determine the propagation direction and spread of the high frequency internal wave field. The results indicate that the mode 1 wave field is highly directional, spread over only 50°. At all frequencies, the propagation direction is unequivocal, indicating a source to the north-east of the study site. The only topographic feature which could conceivably produce these waves is the shelf region of Allen Bay approximately 5 km away. There appears to be very little variation of wave direction with frequency.

The large anomalies in the low frequency across-channel flow were quite surprising. We suggest that because there is no significant vertical velocity and that the low frequency response is not due to

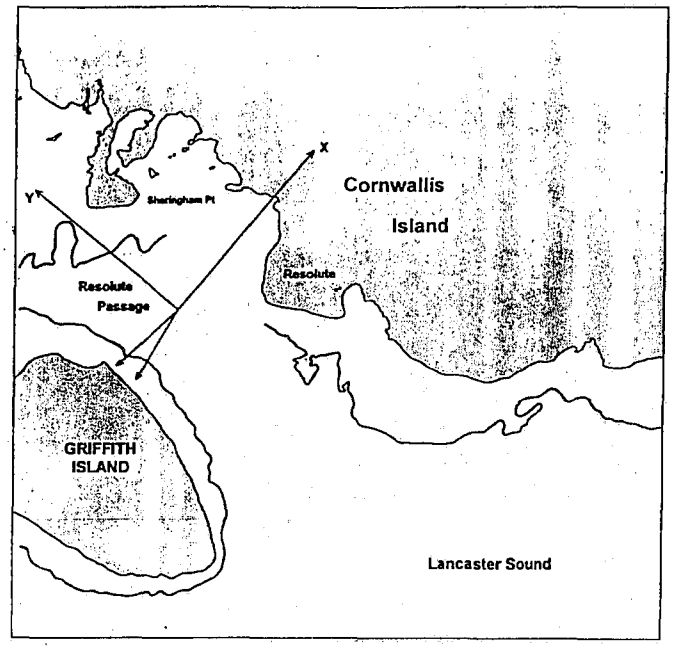

Figure 1. Chart of the study area showing the axes origin at the study location and the orientation used in the paper. The arrows indicate the direction *from which* the mode 1 internal wave field emanates.

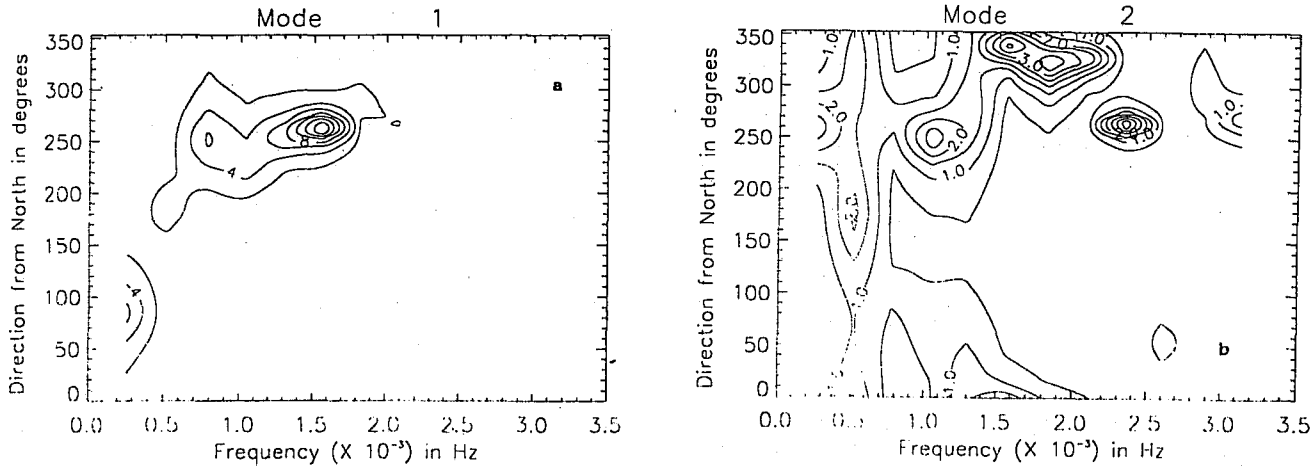

Figure 2. Directional spectra, indicating the direction *towards which* the waves propagate, taken clockwise from the positive y axis of Figure 1 (along-channel) and normalized to the total energy density for mode 1 (Figure 2a) and mode 2 (Figure 2b) using the eigenvector technique of Marsden and Juszko (1987). The contour interval is 2.0 $m^2(rad\ s)^{-1}$.

waves. Perkin and Lewis (1978) and Melling and Lewis(1982) have demonstrated that density flows caused by brine rejection in the shallow regions of Cambridge Bay and the Beaufort Sea can flow down the slope and along isopycnal surfaces in deep water creating substantial currents at depth. The depth and vertical extent of our observations match those reported by Melling and Lewis(1982) based on water mass analyses. We suggest that the observed velocity anomalies observed between 30 and 45 m depth may represent a density driven flow along isopycnal surfaces. The 3 m velocity anomaly could then be attributed to the return flow required to satisfy continuity.

References

Greenwood, K.C., R.F. Marsden, and J.R. Buckley, Intercomparison of an acoustic Doppler current profiler with Cyclesondes in Knight Inlet, British Columbia. *Atmosphere-Ocean* , 31 , 297-318, 1993.

Leblond, P.H., and L.A. Mysak. *Waves in the Ocean* . Elsevier, Amsterdam, 602 pp.

Long,R.B., The statistical evaluation of directional spectrum estimates, derived from pitch/roll buoy data. *J. Phys. Oceanogr.* , 10 , 944-952, 1980.

Longuet-Higgins, M.S., D.E. Cartwright and N.D. Smith, Observations of the directional spectrum of sea waves using the motion of a floating buoy. *Ocean Spectra* . Prentice-Hall, 111-136, 1963.

Marsden, R.F. and B.-A. Juszko, An eigenvector method for the calculation of directional spectra from heave, pitch and roll buoy data. *J. Phys. Oceanogr.* , 17 , 2157-2167, 1987.

—, J.R. Paquet, and R.G. Ingram, Currents under land-fast ice in the Canadian Arctic Archipelago. Part I: Vertical velocities. *J. Mar. Res.* , (Accepted), 1994.

Melling H. and E.L. Lewis, Shelf drainage flows in the Beaufort Sea and their effect on the Arctic Ocean pycnocline. *Deep-Sea Res.*, 29 , 967-985, 1982.

Perkin, R.G. and E.L. Lewis, Mixing in an Arctic fjord, *J. Phys. Oceanogr.* , 8 , 873-880, 1978.

Schott, F and J. Willebrand, On the determination of internal-wave directional spectra from moored instruments. *J. Mar. Res.*, 31 , 116-134, 1973.

Comparison between buoy and COADS wind and wind stress data for the West Coast of Canada

Josef Y. Cherniawsky, William R. Crawford and Robin M. Brown
Institute of Ocean Sciences, Sidney, B.C., Canada V8L 4B2

Introduction

Offshore weather buoys are currently operated along the Pacific Coast of Canada by the Atmospheric Environment Service, Canadian Coast Guard, Department of Fisheries and Oceans and AXYS Environmental Consulting of Sidney, British Columbia (Wood and Wells 1988). The number of buoys has gradually increased from an initial deployment of 2 in September of 1987 to 16 in the fall of 1993. Ten nearshore buoys are of the 3-m discus design and are located as follows: 1 in Dixon Entrance, 2 in Hecate Strait, 2 in Queen Charlotte Sound, 2 about 60 km west of Graham and Moresby Islands, 2 about 35 km west of Vancouver Island and 1 buoy about 10 km southwest of Cape St James (south end of Moresby Island). Three buoys are of the 6-m NOMAD design and are located farther offshore, about 400 km west of the British Columbia Coast. The remaining three buoys are inshore (2 in the Strait of Georgia and 1 in Douglas Channel near Kitimat) and are not part of this study. We used hourly observations of wind speed and direction from two anemometers at each buoy (located at 4.9 and 4.1 m height on NOMADs and 4.9 and 3.7 m on 3-m discus) to calculate surface wind stress from 1990–1994. We describe here buoy wind data processing and wind stress calculations and compare monthly mean vectors of wind and wind stress from buoys with the ship-derived Comprehensive Ocean-Atmosphere Data Set (COADS) for this area. Daily mean buoy wind stress values are mapped onto a regular grid for driving a coastal ocean circulation model.

Processing of buoy wind data

Hourly buoy data were obtained from the Pacific Weather Centre in Vancouver and reformatted from dBASE to portable ASCII, with quality flags marking obvious outliers or suspect data records. Wind speed and direction from suspect records were then compared to adjacent "good" records and the quality flag for each anemometer was reset to "good" (1) from "suspect" (0) if certain continuity criteria were satisfied over a short period (less than 12 hours). Remaining data gaps shorter than 2 days were subsequently "filled" by linear interpolation. While 2 days may seem too long, only a very small fraction of these "short" gaps were longer than a few hours. We used wind data from the top anemometer (at $z = 4.9$ m), unless only the bottom one had valid data. If both anemometers were working but disagreed significantly (e.g., due to a faulty compass), we chose the one that showed a reasonable agreement in direction and synoptic wind changes with other nearby buoys.

Calculation of wind stress

We assumed neutral stability, as stability-dependent calculations (cf. the Monin-Obukhov length) require simultaneous humidity data not available at buoy locations. We calculated friction velocity u_* by equating definition of the drag coefficient, $C_D = u_*^2/U^2$, with its value for neutral stratication, $C_{DN} = [K/\ln(z/z_0)]^2$. $K = 0.4$ is the von Karman constant. Surface roughness length z_0 has contributions from two terms, which are due to short gravity waves and aerodynamic viscosity at low wind speeds: $z_0 = au_*^2/g + 0.11\nu/u_*$, with $a = 0.012$ (cf. Smith 1988). This gave us hourly stress $\boldsymbol{\tau} = \rho u_*^2 \mathbf{U}/U$ and wind $\mathbf{U}_{10}$ extrapolated to 10 m height. A similar procedure was applied to COADS pseudostress $U\mathbf{U}$, with $z = 10$ m and $U_{10} = |U\mathbf{U}|^{1/2}$.

Comparison to COADS data

COADS monthly trimmed data statistics are available on a 2×2 degrees grid for the period 1946–1992 (Slutz et al. 1985). Fig. 1 shows two examples of COADS monthly mean surface wind vectors off the West Coast, for January (left) and July (right) 1992, together with monthly mean 10-m wind vectors from the weather buoys (thick arrows). Typical winter and summer winds show in both data sets, except buoy winds seem to have lower speeds than COADS winds, even if we ignore COADS data that were based on

few ship observations (number in lower-right corner of each square). Notably, there are much fewer ship observations along the North Shore. Fig. 2a shows a scatterplot of COADS versus buoy wind speed for 13 buoys in 36 months from 1990–1992. COADS winds were collocated with buoy winds by calculating weighted mean $\mathbf{U}_C$ at each buoy location from 4 or less (near the coast) $\mathbf{U}_{Ci}$, $\mathbf{U}_C = \sum w_i \mathbf{U}_{Ci} / \sum w_i$, where $w_i = N_i/\alpha_i$ and N_i and α_i are the number of COADS observations and angular distance in degrees from the buoy location. $\sum w_i$ is therefore representative of a total number of observations in the 4 nearest squares. We excluded from Fig. 2 COADS winds with $\sum w_i < 100$. Fig. 2b shows differences in direction (COADS–buoys), also as a function of buoy wind speed.

Discussion

It is clear from Fig. 2a that most COADS monthly mean wind speeds are higher than the corresponding buoy wind speeds by up to $1\,\mathrm{m\,s^{-1}}$ for all buoy wind speed bins. There also seems to be a systematic difference in wind direction (Fig. 2b) with COADS winds to the right of buoy winds by 5–15 degrees. The sign of this direction difference is consistent with wind rotation in a relatively shallow Ekman layer, albeit data scatter on Fig. 2b precludes more definite conclusions. As expected, there is more scatter in direction values at low wind speeds. Differences in wind speed are translated into differences in wind stress (not shown) that increase with wind speed, due to quadratic dependence on wind speed. Possible reasons for the differences in wind speed include: (a) effects of ship superstructure and instrument height on wind speeds from vessels that use anemometers, (b) tendency of some mariners to report higher wind speeds, either by overestimating wave heights (albeit the WMO Beaufort scale conversion may be underestimating wind speeds; see Isemer and Hasse 1992), or by reporting anemometer values that are closer to gust speeds, (c) underestimated buoy winds due to vector averaging over 10 minute samples (Heidorn 1993), (d) lower effective z due to sheltering of buoys by waves (Tseng et al. 1992; see Heidorn 1993 for a review), (e) larger z_0 for steep waves in coastal areas (see discussion in Smith 1988), (f) drift in some anemometer responses after long deployment, as can be seen by comparing data from two anemometers on the same buoy (not shown).

References

Heidorn, K.C., 1993. The influence of high waves on buoy-measured wind speeds. Unpublished report (obtainable from author, AXYS Environmental Consulting, P.O. Box 2219, Sidney, B.C. V8L 3S8).

Isemer, H.-J., and L. Hasse, 1992. The scientific Beaufort scale: effects on wind statistics and climatological air-sea flux estimates in the North Atlantic Ocean. Proceedings of the International COADS Workshop, Boulder, CO, 13-15 January 1992. U.S. Dept. of Commerce, pp 159–177.

Slutz, R.J., S.J. Lubker, J.D. Hiscox, S.D. Woodruff, R.L. Jenne, D.H. Joseph, P.M. Steurer, and J.D. Elms, 1985. Comprehensive Ocean-Atmosphere Data Data Set; Release 1. NOAA Environmental Research Laboratories, Climate Research Program, Boulder, Colo., 268 pp. (NTIS PB86-105723).

Smith, S.D., 1988. Coefficients for sea surface wind stress, heat flux, and wind profiles as a function of wind speed and temperature. J. Geophys. Res., **93**(C12): 15,467–15,472.

Tseng, R.-S., Y.-H. Hsu and J. Wu, 1992. Methods of measuring wind stress over a water surface — Discussions of displacement height and von Karman constant. Bound.-Layer Meteor., **58**: 51–68.

Wood, A.L. and G.E. Wells, 1988. The Canadian meteorological buoy network. Proceedings of Oceanology International '88, March 1988, Brighton, UK, Kluwer Academic Publications, pp 45–50.

Fig. 1. Monthly mean COADS (thin arrows) and weather buoy (thick arrows) winds for January (left) and July (right) 1992, with number of COADS observations given in the right-bottom corner of each 2×2 degrees box.

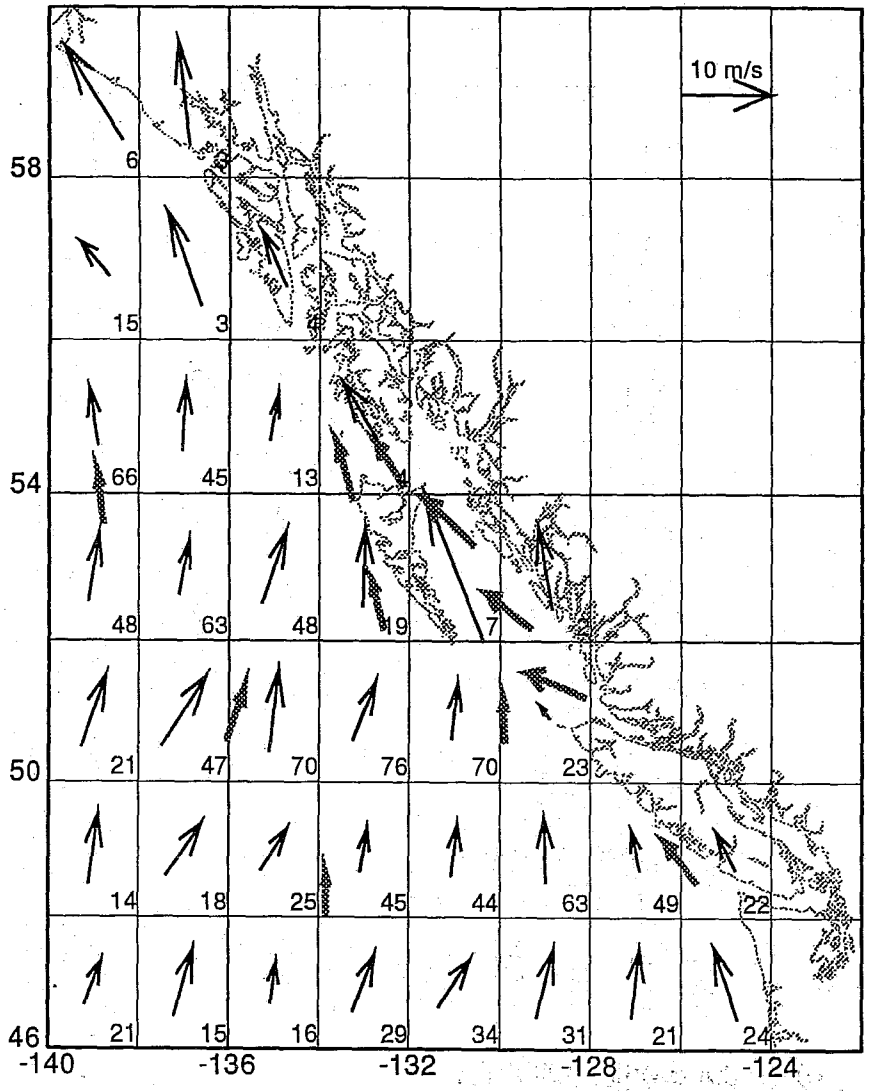

(COADS: Min= 1.80, Max=17.27, Mean= 7.19, StDev= 2.64)
(BUOYS: Min= 4.30, Max= 7.33, Mean= 5.84, StDev= 0.90)

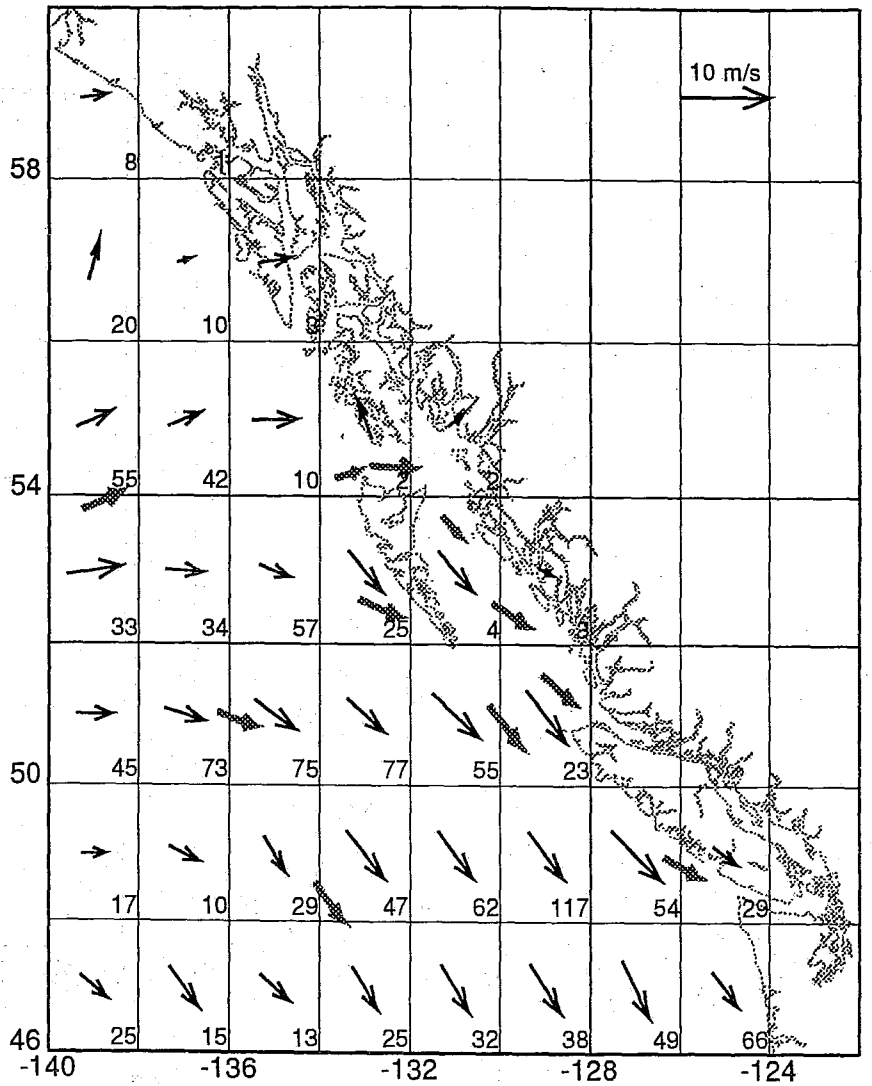

(COADS: Min= 1.55, Max= 7.47, Mean= 4.68, StDev= 1.50)
(BUOYS: Min= 2.59, Max= 5.38, Mean= 4.25, StDev= 0.83)

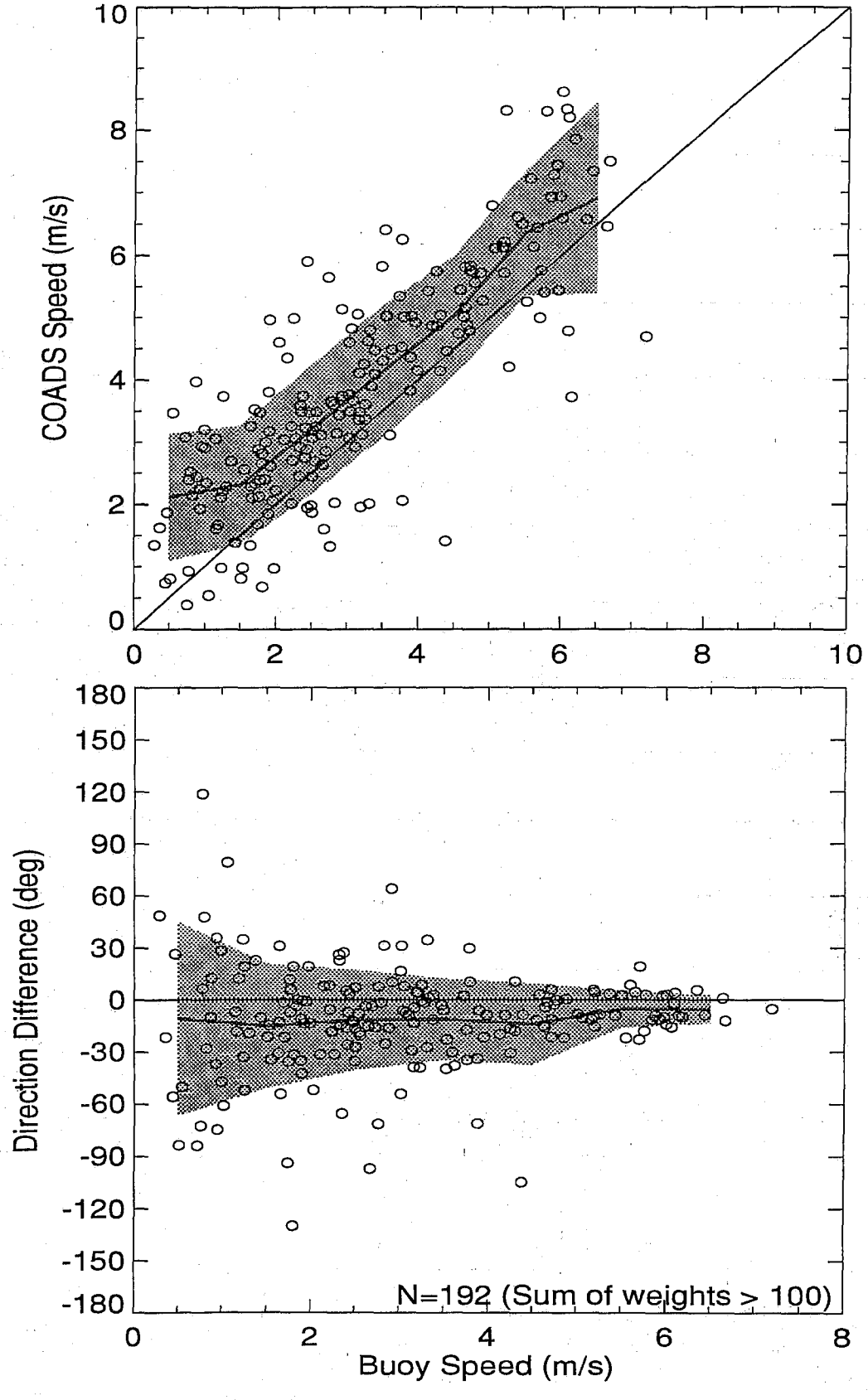

Fig. 2. (a) COADS wind speed and (b) COADS–buoy direction difference versus buoy wind speed, excluding COADS data with too few observations (see text). Thick line and shaded envelope show mean values ± 1 standard deviation for each $1\,\mathrm{m\,s^{-1}}$ buoy wind speed bin.

Model Simulations for Dixon Entrance and the North Coast of British Columbia

V.A. Ballantyne, M.G.G. Foreman, W.R. Crawford, and R. Jacques*

Institute of Ocean Sciences, Department of Fisheries and Oceans
P.O. Box 6000, Sidney, B.C., V8L 4B2, Canada

**Department of Oceanography, University of British Columbia*
Vancouver, B.C., V6T 1Z4, Canada

This paper describes two applications of a three-dimensional circulation model to the coastal seas of northern British Columbia. The first application is a simple extension of the *Foreman et al. (1993)* (henceforth FHWB) barotropic tidal model to three dimensions. The second application is a diagnostic baroclinic calculation of the sub-tidal circulation in Dixon Entrance. In this case, the forcing is derived from conductivity-temperature-depth (CTD) observations and both the bottom frictional and vertical viscous damping use velocities from the three-dimensional tidal model.

This study is part of a project funded by the Panel for Energy Research and Development (henceforth PERD) to study surface currents in Queen Charlotte Sound, Hecate Strait, and Dixon Entrance. Exploratory offshore drilling has indicated the possibility of hydrocarbons in the region and this project aims to establish a basic understanding of surface flows in the event of an oil spill.

The numerical technique used to calculate the three-dimensional tides is described in detail in *Foreman et al. (1995)*. It is virtually the same finite element, harmonic, wave equation method used in *Walters (1992)* and FHWB, and aside from the nonlinear expansions, is similar to the methods employed by *Lynch et al. (1992)* and *Lynch and Naimie (1993)*. In particular, the model solves the three-dimensional, shallow-water equations with conventional hydrostatic and Boussinesq assumptions, and viscosity closure in the vertical.

Following the *Naimie et al. (1994)* study for Georges Bank, we would like to have used seasonally averaged σ_t values to compute seasonal buoyancy flows for the entire north coast region. However our data sets were too sparse, both spatially and temporally, to make this feasible. The most complete CTD coverage was for Dixon Entrance and this was the area chosen for the diagnostic baroclinic modelling. Examination of historical records revealed six CTD surveys with extensive spatial coverage of Dixon Entrance. Three of these were for the summer, while one was available for each of the remaining seasons.

The numerical technique used for the diagnostic calculation of the three-dimensional density flows is essentially the same as for the tides. Whereas the tidal model is forced by specifying elevation amplitudes and phases for the constituents M_2, S_2, K_1, O_1, N_2, K_2, P_1, and Q_1 along the sea boundaries, the density model is forced with vertically-integrated horizontal density gradients that were calculated from objectively analysed CTD data.

Both 3D models employ 11 sigma surfaces in the vertical and a triangular grid in the horizontal. The north coast grid used for the tidal calculations has 5101 nodes, 8368 triangles, and a resolution that varies between 35km and 250m. It was created with TRIGRID (*Henry*

and Walters, 1993). The Dixon Entrance grid used for the baroclinic calculations has 1038 nodes, 1742 triangles and is simply a subset of the north coast grid.

Accuracy of the tidal model was assessed by comparing its results with the same historic tide gauge data that were used in FHWB. The RMS elevation differences were found to be virtually the same as for the 2D model. Similar comparisons were also done for the tidal currents (e.g., Figure 1) with the only notable difference between the 2D and 3D model results now being the inclusion of a bottom Ekman layer. In general, comparisons with the ellipses from observed tidal currents demonstrated that the model accuracy is very good except in regions of strong baroclinicity. Although the Figure 2 tidal residual currents show a closed Rose Spit Eddy (whereas the FHWB results did not), the magnitudes are weak compared to observations (*Crawford and Greisman, 1987*) and re-inforce the *Bowman et al., 1992* conjecture that this eddy does not arise solely from barotropic tidal rectification.

Figure 3 shows the diagnostically computed buoyancy currents corresponding to the spring 1984 CTD survey. Low-pass filtered current meter observations are also shown and are seen to be in reasonable agreement. The Rose Spit Eddy is now well defined and much stronger than when the forcing was solely due to barotropic tidal rectification.

Further details on the diagnostic calculation of buoyancy currents can be found in the *Jacques et al.* submission in this volume. A more complete description of the entire study can be found in *Ballantyne et al. (1995).*

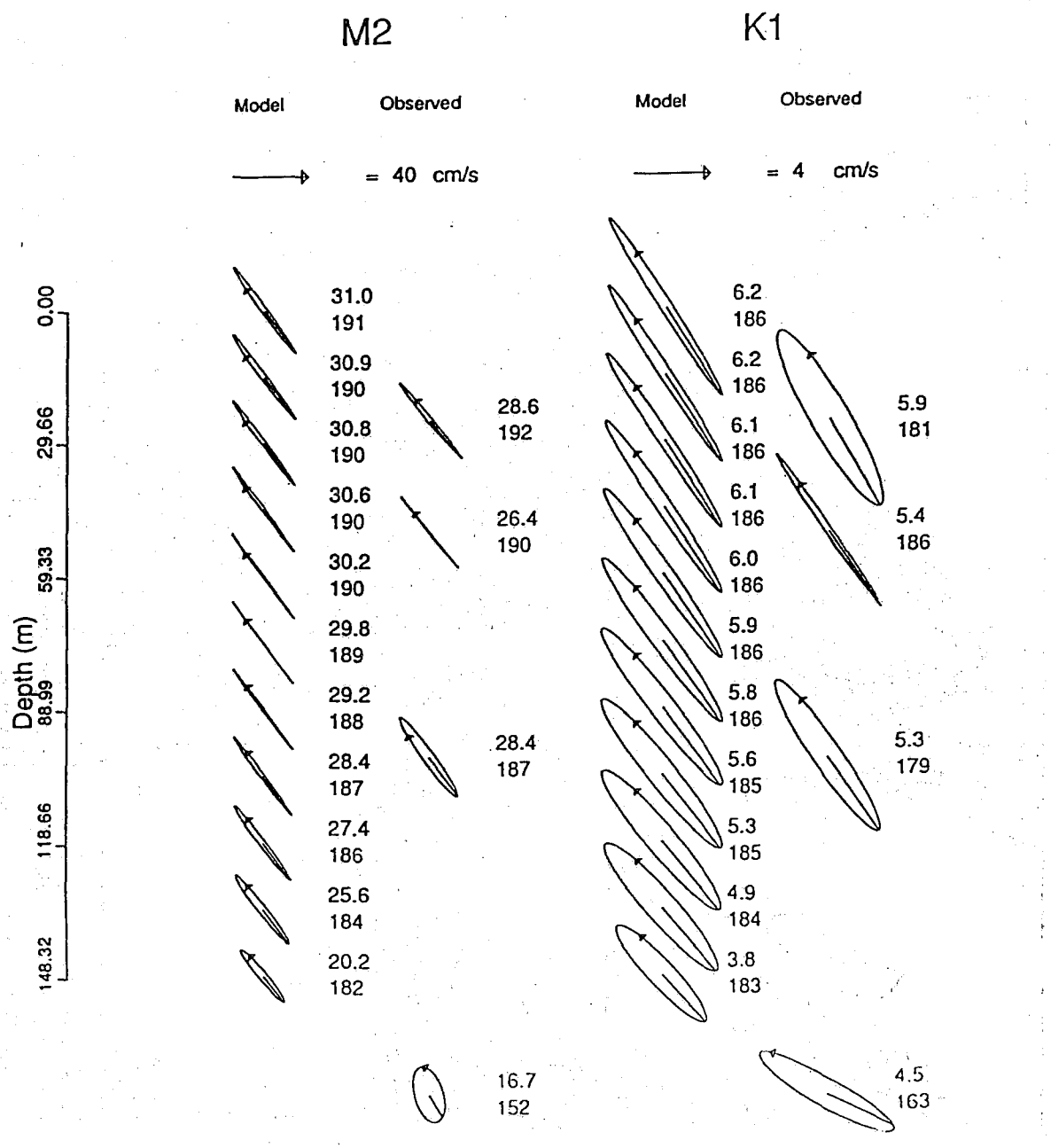

Figure 1: M_2 and K_1 current ellipses at site W02 in the center of eastern Hecate Strait. The line within each ellipse denotes G, the position of the current vector at the time of maximum tidal potential at Greenwich, and the arrow denotes the sense of rotation. The two numbers beside each ellipse are the major semi-axis (top, in cm/s) and G (bottom, in degrees, UT). Note the scaling difference for M_2 and K_1.

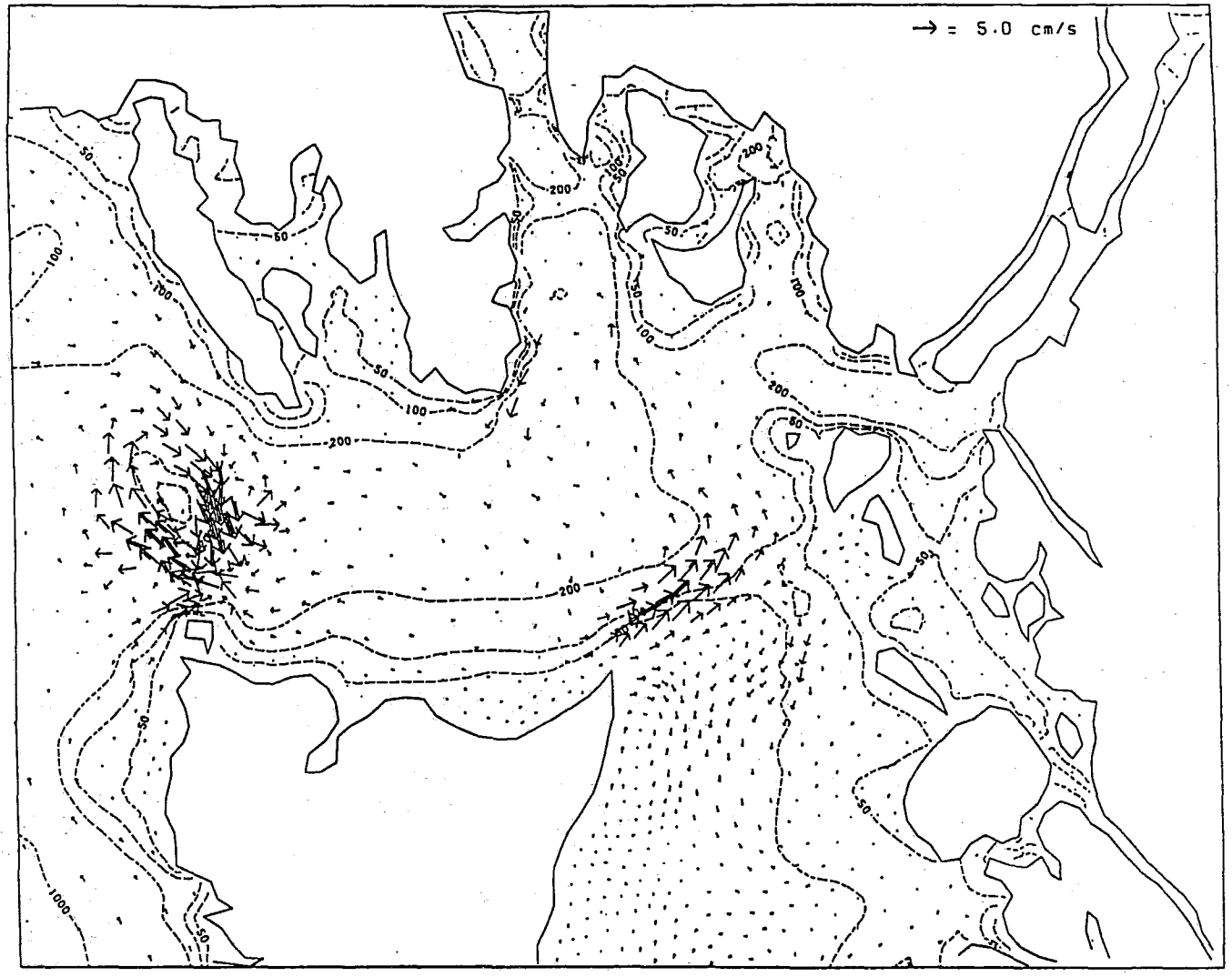

Figure 2: Diagnostically computed velocities at 50 m arising from tidal rectification and density forcing for the April 12–22, 1984 CTD survey. Observed currents are shown in bolder type with a small circle at their foot and the mooring name nearby. Single shafts in multi-shafted vectors represent 10 cm/s.

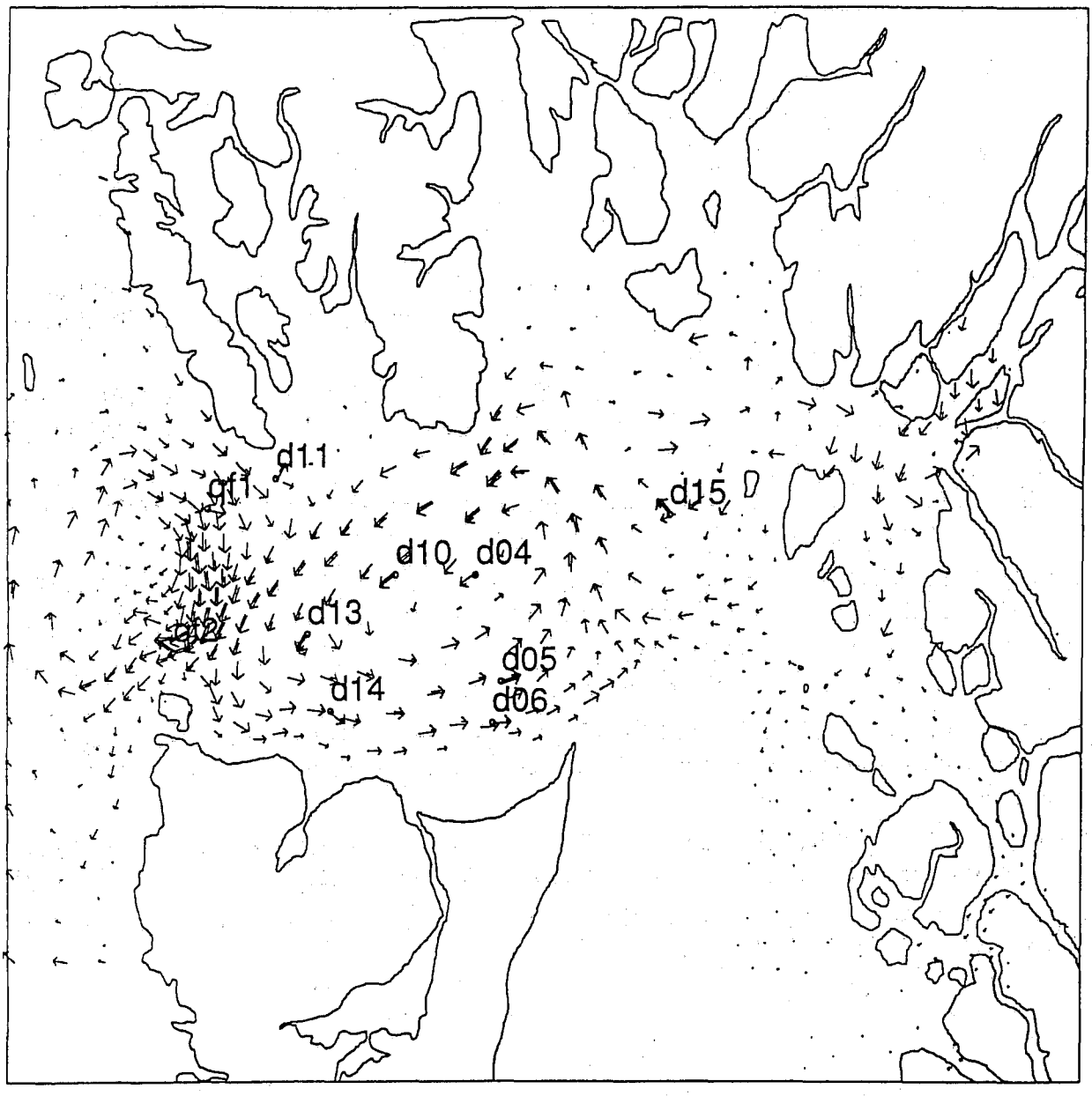

Figure 3: Tidal residual velocities in Dixon Entrance. Single shafts in multi-shafted vectors represent 5 cm/s.

References

BALLANTYNE, V.A., FOREMAN, M.G.G., CRAWFORD, W.R., and JACQUES, R. 1995. Three-dimensional model simulations for the north coast of British Columbia. Submitted to *Continental Shelf Research.*

BOWMAN, M.J., VISSER, A.W., and CRAWFORD, W.R. 1992, The Rose Spit Eddy in Dixon Entrance: Evidence for its existence and underlying dynamics, *ATMOS. OCEAN, 30(1), 70–93.*

CRAWFORD, W.R., and GREISMAN, P. 1987. Investigation of permanent eddies in Dixon Entrance, British Columbia. *Cont. Shelf Res.*, **7**, 851–870.

FOREMAN, M.G.G., HENRY, R.F., WALTERS, R.A., and BALLANTYNE, V.A. 1993. A finite element model for tides and resonance along the north coast of British Columbia. *J. Geophys. Res.*, **98, C2**, 2509–2531.

FOREMAN, M.G.G., WALTERS, R.A., HENRY, R.F., KELLER, C.P., and DOLLING, A.G. 1995. A tidal model for eastern Juan de Fuca Strait and the southern Strait of Georgia. *J. Geophys. Res.*, **100, C1**, 721–740.

HENRY, R.F., and WALTERS, R.A. 1993. Geometrically-based, automatic generator for irregular triangular networks. *Commun. Numer. Methods Eng.*, **9**, 555–566.

JACQUES, R., LEBLOND, P.H., FOREMAN, M.G.G., BALLANTYNE, V.A., and CRAWFORD, W.R. Modelling the mean water circulation in Dixon Entrance Region. This volume.

LYNCH, D.R., and NAIMIE, C.E. 1993. The M_2 tide and its residual on the outer banks of the Gulf of Maine. *J. Phys. Oceanogr.*, **23**, 2222–2253.

LYNCH, D.R., WERNER, F.E., GREENBERG, D.A., and LODER, J.W. 1992. Diagnostic model for baroclinic, wind-driven and tidal circulation in shallow seas. *Cont. Shelf Res.*, **12**, 37–64.

NAIMIE, C.E., LODER, J.W., and LYNCH, D.R. 1994. Seasonal variation of the three-dimensional residual circulation on Georges Bank. *J. Geophys. Res.*, **99, C8**, 15,967–15,989

WALTERS, R.A. 1992. A three-dimensional, finite element model for coastal and estuarine circulation. *Cont. Shelf Res.*, **12**, 83–102.

Modelling the Mean Water Circulation in Dixon Entrance Region

Renée Jacques and Paul H. LeBlond
Department of Oceanography, University of British Columbia, Vancouver, B.C., Canada V6T 1Z4
Michael G.G. Foreman, V. Anne Ballantyne, and William R. Crawford
Institute of Ocean Sciences, Department of Fisheries and Oceans, Sidney, B.C., Canada V8L 4B2

Introduction

This paper investigates the mean circulation of Dixon Entrance and surrounding waters using a finite element model. The model responds to buoyancy and tidal forcings as well as runoff. The main purpose of the study is to increase the understanding of the dynamics that controls the mean circulation of these waters and to develop a circulation model for the area.

The region is composed of Dixon Entrance, a east-west depression in the continental shelf bounded by mountains, Hecate Strait, a north-south narrow and shallow channel which widens and deepens to the south, and Chatham Sound, a body of water separated from the two previous regions by a chain of shoals and islands. The Skeena and Nass rivers (second and third most important rivers in British Columbia) flow into Chatham Sound. The waters of the study area are stratified all year round and the salinity of surface waters reaches a minimum in early summer, when snow on top of the mountains melts. The main topographic features of the region are a shallow bank (Learmonth Bank) at the seaward end of Dixon Entrance and an abrupt depth increase from Hecate Strait to Dixon Entrance. The surface water circulation includes a well-defined cyclonic eddy (Rose Spit Eddy) which fills the entire eastern end of Dixon Entrance and a less well-defined anticyclonic eddy around Learmonth Bank [*Bowman et al.*, 1992].

Circulation Model and Forcings

The mean water circulation is studied numerically with a finite element model described in *Ballantyne et al.* [this issue]. The model is three-dimensional, diagnostic, and nonlinear. The model grid is composed of horizontal linear triangular finite elements and a vertical sigma-coordinate system (with 11 levels). Extensive salinity and temperature measurements taken in 1985 and 1991 are used in combination with statistical interpolation [*Le Traon*, 1990] to calculate the tridimensional density field. The tides are obtained from the three-dimensional tidal model described in *Ballantyne et al.* [this issue]. Density field, tides, and river runoff data from Skeena and Nass rivers are used to drive the model.

Model Results and Evaluation

Linear model results were obtained from four density fields calculated from three summer cruises (30 June to 6 July 1985, 24 June to 7 July 1991, and 5 July to 18 August 1991) and one winter cruise (2 to 18 December 1991). All of them show the presence of the Rose Spit Eddy. Around Learmonth Bank, they all show a different flow pattern. Nonlinear model results were also obtained from the same density fields. In all cases the nonlinearity had the effect of amplifying the Rose Spit Eddy and complicating the flow around Learmonth Bank. The effect

of adding river discharge as a boundary condition had negligible effect on the mean circulation. This is due to the fact that runoff information is implicitly included in the density field. The mean surface currents obtained from the winter density field (figure 1) are stronger than the ones obtained from any summer density field (e.g. figure 2). This is probably due to the presence of strong winds in winter time. Even if wind stress was not here used to force the model, its effect is also implicitly included in the density field. It should also be noted that in winter the surface waters flow out of Chatham Sound almost exclusively through the northern channel (figure 1). In summer the waters flow out of the sound partially through that channel and through Brown Passage (figure 2).

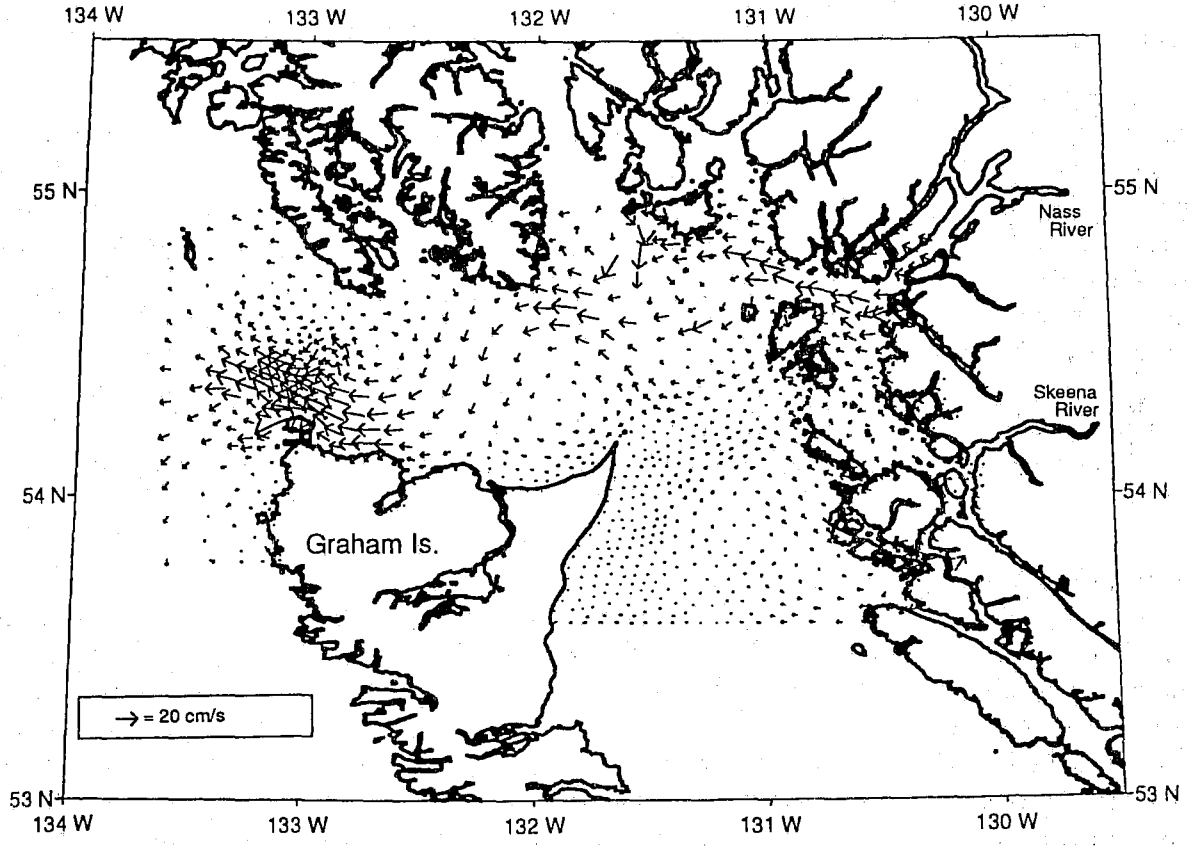

Figure 1: Mean winter surface circulation obtained from nonlinear model. The model was forced by the density field calculated from CTD data taken from 2 to 18 December 1991 and by the tides.

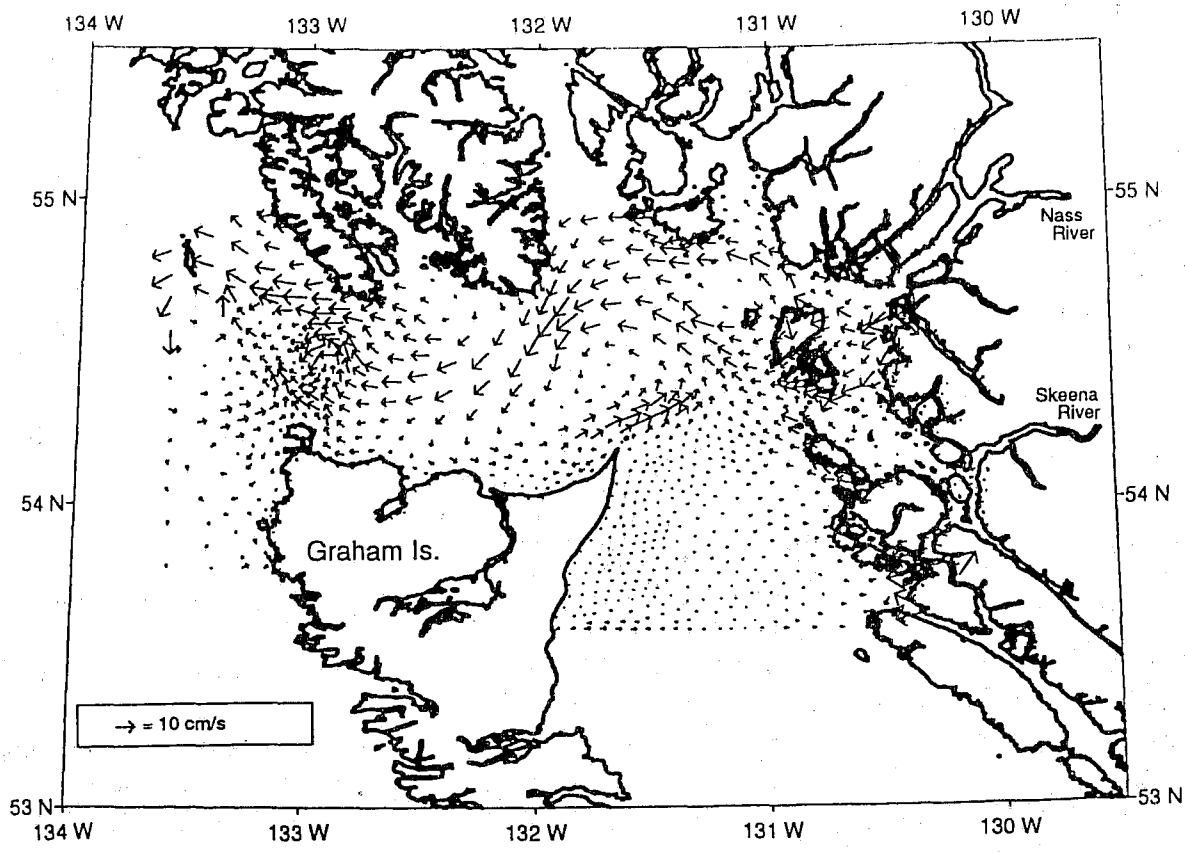

Figure 2: Mean summer surface circulation obtained from nonlinear model. The model was forced by the density field calculated from CTD data taken from 24 June to 7 July 1991, by the tides, and by river runoff.

The model evaluation was done by comparing model results with Eulerian (current meters) and Lagrangian (drifters) current measurements. Comparison with current meters is not obvious due to the lack of current meter measurements in areas of interest. Heavy fishing in the region restrains the possibility to deploy current meters and most of all to retrieve them intact. Comparison with existing current meter data, low-pass filtered and averaged over cruise period, shows a good agreement in Dixon Entrance but not in Chatham Sound where the flow is highly variable and in Hecate Strait where the wind has a strong influence. Drifter data are more complicated to compare with the model results which are Eulerian currents. Nevertheless, drifter tracks show a divergence zone around Learmonth Bank which emphasizes the complexity of the flow around it.

Summary and Future Work

This preliminary study shows satisfactory results. It is however essential to improve the model accuracy to get currents which are closer to the observations. There are many ways of improving the accuracy and it will first be achieved by increasing the horizontal accuracy trough mesh refinement. The forcings used to drive the model will also be improved through a better statistical interpolation and addition of the wind stress as a surface boundary condition.

The interpolation will be improved in order to avoid as much as possible creation of density inversions and by using a variable horizontal scale of correlation through the domain. The wind stress will be obtained using wind data from moored buoys [*Cherniawsky et al.*, this issue] and from lighthouse stations. As the data from moored buoys are available only for the last 4–5 years, a transfer function between wind data from lighthouse stations and buoys will be developed in order to build a longer oceanic wind time series.

Finally a prognostic model for long time steps (about a week) will be investigated in order to hindcast the water properties of the region and to study their variability.

Acknowledgments. We thanks R.A. Walters for providing the code for the finite element numerical model. This work was supported by an NSERC graduate fellowship.

References

Ballantyne, V.A., Foreman, M.G.G., Crawford, W.R., and R. Jacques, Model simulations for Dixon Entrance and the north coast of British Columbia, this issue.

Cherniawsky, J., Crawford, W.R., and R.M. Brown, Intercomparison of surface wind data off the BC Coast, this issue.

Bowman, M.J., A.W. Visser, and W.R. Crawford, The Rose Spit Eddy in Dixon Entrance: evidence for its existence and underlying dynamics. *Atmos.-Ocean*, 30(1), 70–93, 1992.

LeTraon, P.Y., A method for optimal analysis of fields with spatially variable mean, *J. Geophys. Res.*, 95 (C8),13,543–13,547, 1990.

Numerical Modeling and a Comparison to Observations of Flow around Canyons

S. E. Allen
Dept. of Oceanography, Univ. of British Columbia, Vancouver, B.C., V6T 1Z4
allen@ocgy.ubc.ca

Abstract. Canyons have recently attracted the attention of the numerical modeling community as a test site for an intercomparison of models (Haidvogel, 1995). However, as flow around and within canyons is not yet dynamically understood, we will consider the comparison between a simple, layered, numerical model and a set of observations. The most comprehensive set of observations with regards to low frequency phenomena are the 1983 observations over Astoria Canyon (Hickey, 1995).
In order to simulate the observations the timing of the forcing must be correctly incorporated. In contrast, sensitivity studies show that the flow is insensitive to changes in the geometry of the canyon, the density steps between the layers and the depths of the layers. Three layers are, however, incapable of reproducing the full variation in the vertical observed at Astoria.

1 Introduction

Observations of flow within canyons include Freeland and Denman (1982), Hickey *et al,* (1986), Kinsella *et al.* (1987), and more recently Hickey (1995). This latest set of data gives good spatial coverage with two lines of three moorings across the canyon.

Analytic models include Freeland and Denman (1982), Klinck (1988, 1989), Chen and Allen (1995) and Allen (1995). More recently numerical models have been used. Allen (1992), and Klinck (1994) used the SPEM model to look at continuously stratified flow over fairly smooth canyons. Whereas, Allen (1995). used a three layer model to simulate flow over a canyon with very sharp walls in good agreement with the actual shape of Astoria canyon. The results of this model will be compared to the data ofHickey (1995).

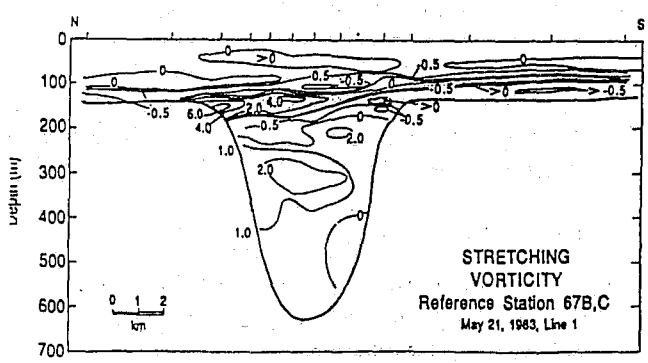

Figure 1: Figure showing the vorticity field within the canyon during upwelling. Shown is a vertical cross-section of the observations. From Hickey (1995).

2 Observations

The observations consist of measurements from a moored array as well as a CTD survey, made in May through August 1983 over Astoria Canyon which lies off the mouth of the Columbia river. The moorings captured three strong spring upwelling events and fortuitously, one of the CTD surveys was also conducted during one of these events.

During upwelling the strengthened, southwards flow was observed to cross the canyon with little deflection. As the shelf water flows over the north canyon wall, it is stretched as it drops down into the canyon. See Figure 1. This cyclonic vorticity is contained to the north side of the canyon with generally anticyclonic vorticity on the south side and over the south shelf. Within the canyon, water is upwelling, fed from the mouth of the canyon. These fluid columns are also stretched. Between these two cyclonic layers there is a thin layer, compressed by the rising waters below and descending waters above.

3 Model

The model is an explicit finite difference layered model which solves the nonlinear shallow water equations using the Arakawa and Lamb energy and enstrophy conserving Jacobian for the nonlinear terms. The model does not use a rigid lid.

To model Astoria canyon, a three layer model was used. The upper interface is the strongest and lies above the shelf. The lower interface is about ten times weaker and lies below the shelf, within the canyon and deep off-shelf water. The upper interface models the thermocline whereas the the lower interface is an ap-

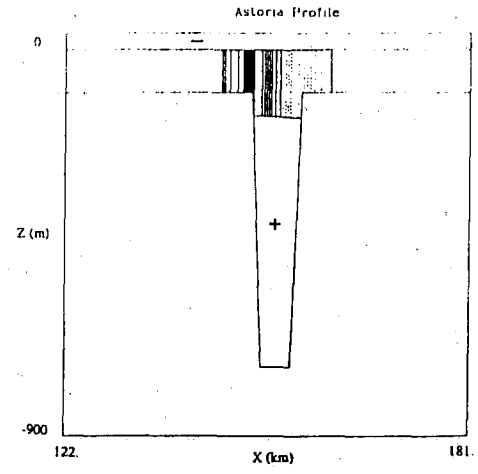

Figure 2: Figure showing the vorticity field within the canyon during upwelling. Shown is a vertical cross-section through the modelling results.

proximation to the continuous stratification expected at depth.

It is assumed that an upwelling favourable wind is blowing, moving fluid offshore in an upper Ekman layer. Thus, the model is forced by removal of fluid at the surface to imitate the water pumped into this, unmodelled, upper Ekman layer.

A vorticity cross-section is shown in Figure 2. The vertical block structure is due to the three-layer stratification of the model.

4 Comparison

Figure 1 shows the vorticity field at maximum upwelling across the canyon. Figure 2 shows the same field for the modelled case.

The model shows strong cyclonic vorticity on the north side of the canyon as fluid columns drop into the canyon, anticyclonic vorticity on the south side of the canyon, generally weak vorticity in the upper layer and cyclonic vorticity within the canyon all in agreement with the observations.

The major disagreement is the magnitude of the vorticity and the lack of an anticyclonic layer between the upwelled deep canyon water and the water crossing over and dipping into the canyon. The latter disagreement is expected as the model does not have enough vertical resolution to detail 4 different vertical responses. The former is partially due to lower flow speeds but is probably also mainly due to vertical stratification. In the model the amount of vorticity generated is given directly by the difference in, the predefined, layer depth over the canyon relative to that over the shelf. The observations of the nepheloid layer over the shelf (not shown, see Hickey (1995)) which crosses into the canyon, show a very thin layer which is stretched by a factor of five as it drops into the canyon.

5 Sensitivity

The horizontal flow is sensitive to the time history of the flow as the advection of potential vorticity determines its pattern. The flow is however, generally insensitive to variations in the reduced gravities across the two interfaces, the position of the forcing and the depths of the various layers.

6 Conclusions

The model does well in predicting the gross horizontal characteristics of upwelling over a canyon and lead to intuition regarding the origin of the various observed vorticities. Its ability to incorporate very steep topography enables it to capture much of the observed vorticity structure. However, the flow over the canyon has a more complicated and detailed vertical structure than expected and the three layer does not provide sufficient vertical resolution. The SPEM model as used by Klinck (1994) holds more promise for the full simulation of the observed flow.

Simply adding full vertical structure will not necessarily explain all the observations. Between upwelling events, Hickey (1995) reports the presence of a cyclone over the canyon which she attributes to a Taylor cap. Due the strong and steep topography, a second possible explanation is tidal rectification.

References

Allen, J. S. 1992: The effects of alongshore variations in bottom topography on coastal upwelling. In *EOS Trans., AGU Fall Mtg.* volume 73 Supp. 317.

Allen, S. E. 1995: Topographically generated, subinertial flows within a finite length canyon. Submitted to *J. Phys. Oceanogr.*

Chen, X. and S. E. Allen, 1995: Influence of canyons on shelf currents – a theoretical study. Submitted to *J. of Geophys. Res.*

Freeland, H. J. and K. L. Denman, 1982: A topographically controlled upwelling center off southern Vancouver Island. *J. Marine Res.* **40**, 1069–1093.

Haidvogel, D. B. 1995: Form stress and coastal ocean models. In *Flow-topography interactions.* 'Aha Huliko'a.

Hickey, B., E. Baker, and N. Kachel, 1986: Suspended particle movement in and around Quinault submarine canyon. *Marine Geol.* **71**, 35–83.

Hickey, B. M. 1995: Astoria Canyon. Submitted to the *J. Phys. Oceanogr..*

Kinsella, E. D., A. E. Hay, and W. W. Denner, 1987: Wind and topographic effects on the Labrador current at Carson canyon. *J. Geophys. Res.* **92**, 10,853–10,869.

Klinck, J. M. 1988: The influence of a narrow transverse canyon on initially geostrophic flow. *J. Geophys. Res.* **93C**, 509–515.

Klinck, J. M. 1989: Geostrophic adjustment over submarine canyons. *J. Geophys. Res.* **94C**, 6133–6144.

Klinck, J. M. 1994: Model study ofeffect of alongshore flow on circulation in submarine canyons. In *EOS Trans., AGU Fall Mtg.* volume 75 Supp 204.

bblt: A Model for Suspended Sediment Transport in the Benthic Boundary Layer

C. G. Hannah
Oceadyne Environmental Consultants, 373 Ridgevale Dr., Bedford, N.S., B4A 3M2

J. W. Loder, D. K. Muschenheim and Y. Shen
Department of Fisheries and Oceans, Bedford Institute of Oceanography, Dartmouth, N.S., B2Y 4A2

1 Introduction

We present exploratory results from a novel benthic boundary layer transport model, developed to evaluate the transport of suspended particulate drill waste in the benthic boundary layer on the continental shelf. The motivating application is the prediction of impact zones around exploration and production drilling platforms in regions where there is potential for adverse impacts on commercially important benthic organisms, such as sea scallops on Georges Bank (Gordon et al. 1993; Cranford and Gordon 1992; Muschenheim et al. 1995). The model is part of an impacts zone assessment model being developed through the PERD Task 6B Environmental Subprogram.

Our primary interest is the transient (time scales of days to weeks) loadings of drill waste in the near field surrounding a discharge site (where concentrations are expected to be greatest). Here we focus on the tidal and mean currents, which represent the dominant forcing during periods of light winds and on the shear dispersion arising from the interaction of vertical mixing and vertical shear in the horizontal velocity. Model applications are presented for a drilling site on Sable Island Bank and for the scallop grounds on Georges Bank, where shear dispersion is expected to be particularly important due to the strong M_2 tidal currents with large vertical shears in the lower water column.

2 Model

The model, `bblt`, was formulated to provide a reliable quantitative representation of the dominant physical processes in a simplified context so that parameter dependencies can be understood. The primary assumptions are: 1) the water depth and currents have small horizontal variations over the scale of the sediment patch and its transport; 2) the velocity profile is given (from observations or a numerical model) and allowed to vary with depth and time; 3) the suspended sediment transport problem can be divided into two phases: vertical redistribution and horizontal transport; 4) the vertical distribution can be parameterized in terms of an equilibrium concentration profile; 5) no interaction between sediment size classes; and 6) horizontal transport and vertical mixing can be represented by the movement of discrete pseudo-particles, or packets, which have different vertical movement properties than real sediment particles.

The details of the sediment resuspension processes and the small scale interactions of the sediment with the bottom are included in the parameterization of the vertical concentration profile. The sediment is partitioned into N discrete packets each of which represents a sediment mass m and has a specified settling velocity w_s. In the horizontal the packets are advected by the specified velocity field. In the vertical the location of the packets is parameterized using a specified concentration profile which in this paper is taken as a modified Rouse profile

$$c(z) = c_a(a/z)^p \tag{1}$$

where c_a is the concentration at the reference height, z the vertical coordinate ($z = 0$ at the bottom and is positive upwards), and $p = w_s/(\kappa u_*)$ where w_s is the fall velocity of the sediment, κ the von Karman constant and u_* the friction velocity (e.g. Dyer 1986 and van Rijn 1993). The reference height a is taken as the lower boundary of the suspended sediment load, with a typical value of 1 cm.

Table 1: Parameter values at the exploratory sites. The range of u_* over the tidal cycle is given.

site	depth (m)	peak surface speed (m s^{-1})	r (m s^{-1})	u_* (cm s^{-1})
Cohasset	38.6	0.25	0.83×10^{-3}	0.8 / 1.0
NEP 1	68.8	0.95	2.4×10^{-3}	2.3 / 3.6
NEP 2	73.7	1.06	1.8×10^{-3}	1.3 / 2.9

Table 2: Effective horizontal diffusivity as function of settling velocity. The range of $\bar{z}$ (mean packet height) over a tidal cycle is given. K' is computed along the axis of maximum variance.

w_s	$\bar{z}$	K' (m^2 s^{-1})		
(cm s^{-1})	(m)	$t_m = 1$ hr	$t_m = 3$ hr	$t_m = 10$ hr
Cohasset				
0.2	11/13	9.0	18.6	14.2
0.4	1.5/4.2	10.2	20.8	15.6
1.0	.02/.03	.038	.077	053
Northeast Peak 1				
0.2	30/32	43.7	89.2	62.8
1.0	5.2/17	137	275	192
2.0	0.5/1.4	54	111	79
Northeast Peak 2				
0.2	29/33	78	166	251
1.0	.16/13	140	284	240
2.0	.02/.28	8.9	19	19

The method for computing the vertical positions of the packets is described in Hannah et al. (1995a, 1995b). Vertical redistribution of the packets takes place through expansion and contraction of the profile and through the shuffling of the vertical positions of the packets. The modelling parameter t_m controls the rate at which the vertical positions of the packets are shuffled.

The model inputs are the velocity field, the number, mass and initial horizontal distribution of the packets, the settling velocity of the size class under consideration w_s, the advection time step Δt_a, the packet shuffling time scale t_m, the reference height a, the water depth h, and the functional form of the friction velocity u_*. Here we take u_* as $\sqrt{rU(1)}$, where r is a linear friction coefficient and $U(1)$ is the water speed 1 m above the bottom.

The effective horizontal diffusivity (K') with respect to the center of mass is used as a quantitative index of the model results. It is defined as the (time averaged) rate of change of the variance in the horizontal packet positions (computed without regard for the vertical coordinate).

Experiments with linear velocity profiles show that `bblt` is consistent with basic shear dispersion theory (e.g. Fischer et al. 1979). In particular for steady flow $K' \propto t_m$; and for periodic flow $K' \to 0$ for $T/t_m \ll 1$ (weak mixing) and $K' \to K_0$ for $T/t_m \gg 1$ (strong mixing) where T is the tidal period and K_0 the steady state result (for the particular value of t_m). For periodic flow we find that K' is maximum for $t_m \sim T/4$ (~ 3 hr for the M_2 tide). These results are reported in Hannah et al. (1995a, 1995b).

3 Exploratory Applications

We consider two contrasting areas: the oil production site Cohasset on Sable Island Bank, and the scallop grounds on the Northeast Peak of Georges Bank. Experiments with `bblt` were conducted using the M_2 tidal currents, the tidally rectified mean current, and the linearized bottom friction coefficient

taken from the nonlinear regional model of Lynch and Naimie (1993) and Naimie et al. (1994). There are three primary groups of experiments (Table 1) which represent moderate tidal currents (Cohasset), strong tidal currents (NEP 1) and strong tidal currents with a large residual current (NEP 2). All experiments consider the dispersion of a localized initial distribution of suspended material with the same number of packets.

The velocity as a function of depth and time is shown in Fig. 1 using the tidal ellipses at selected depths offset by the mean current: each ellipse is the loci of the heads of the velocity vector as a function of time. The vertical shear is due to both the change in the sizes of the ellipses and the phase differences. The mean currents at Cohasset and NEP 1 are small. The mean currents at NEP 2 are large enough (30 cm s^{-1} at the surface) to cause a substantial shifting of the tidal ellipses; there are reduced currents and shear on one phase of the tide and increased currents and shear on the opposite phase.

The currents and bottom friction are larger on the Northeast Peak than at Cohasset. As a result u_* is 2 to 4 times larger on the Northeast Peak (Table 1) and for fixed w_s, the mean height of the sediment concentration profile is much greater on the Northeast Peak than at Cohasset (Table 2). The greater range of $\bar{z}$, the vertical center of mass of the concentration profile, over a tidal cycle at NEP 2 compared with NEP 1 is a result of the mean current reducing the velocity and u_* at one phase of the tide.

Laboratory experiments with drill mud suggest that settling velocities on the order of 1 cm s^{-1} are expected for flocculated drill mud fines. Therefore we consider a range of settling velocities around $w_s \sim 1$ cm s^{-1}.

The model results for the various cases are summarized in Table 2, in terms of the effective horizontal diffusivity K'. For a particular settling velocity, there is a marked contrast in the Cohasset and Northeast Peak dispersion rates, with the latter being much larger because of the stronger currents and bottom stresses on Georges Bank. For the typical value of $w_s = 1$ cm s^{-1}, this contrast remains when the Cohasset stresses are quadrupled (Hannah et al. 1995b), even though such a change has a large effect on the vertical distribution and consequently the horizontal dispersion rate.

As a function of t_m, the maximum dispersion generally occurs for $t_m = 3$ hr reflecting the dominance of the M_2 tide. As a function of w_s and $\bar{z}$, the maximum dispersion generally occurs for an intermediate value of $\bar{z}$ rather than when the sediment is uniformly distributed. In both cases, the exception occurs for NEP 2 for $w_s = 0.2$ cm s^{-1}, where the maximum dispersion occurs for $t_m = 10$ hr, which reflects the influence of the mean-current shear in the upper water column associated with the baroclinic pressure gradients (Naimie et al. 1994). These results are consistent with the basic understanding of `bblt` and its representation of shear dispersion built up in Hannah et al. (1995a, 1995b)

The horizontal distribution of the packets after 3 tidal cycles (37.4 hr) with $w_s = 1$ cm s^{-1} and $t_m = 3$ hr are shown in Fig. 1. In the NEP 1 and NEP 2 cases the packet concentrations are much lower than in the less dispersive Cohasset case (note the change in horizontal scale) and the mean horizontal position drifts to the southeast at about 1.4 and 5 km d^{-1}, respectively. Notice that in all three cases the sediment spreads along the major axis of the velocity ellipses and that the shape of the distribution approximates the velocity ellipses.

4 Discussion

A novel model for the evaluation of the transport and dispersion of suspended particulate matter in the benthic boundary layer on the continental shelf has been developed. Application to Sable Island Bank and the Northeast Peak of Georges Bank has indicated that:

- For estimates of u_* representing tidal and mean flow influences, settling velocities in the range of 0.1 to 5 cm s^{-1} yield concentration profiles which range widely from uniformly distributed in the vertical to trapped near the bottom.
- There is a strong dependence of the horizontal dispersion on the bottom shear stress and the settling velocity for settling velocities on the order of 1 cm s^{-1}.

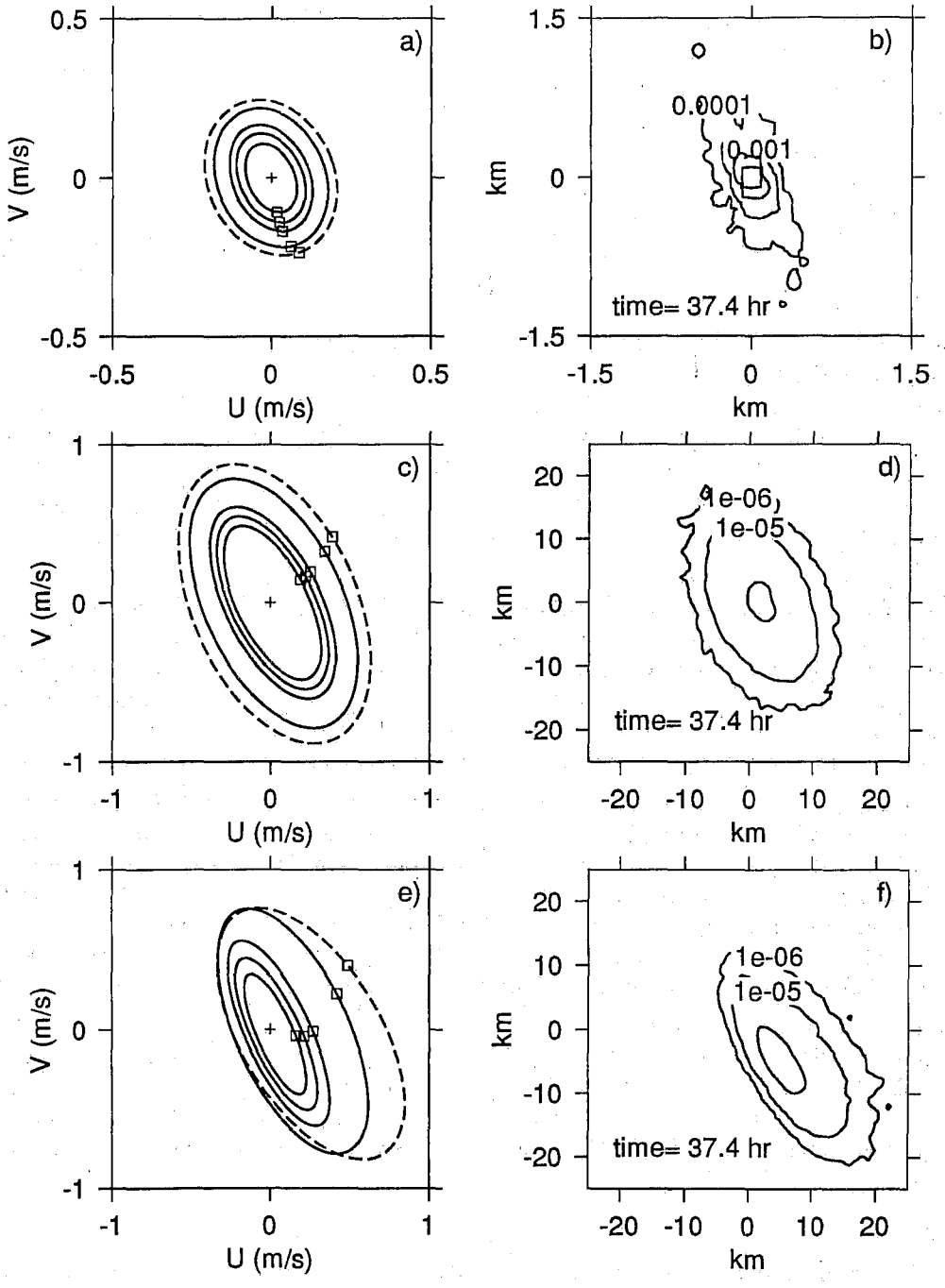

Figure 1: Velocity ellipses and horizontal distribution of the packets, after 3 tidal cycles with $w_s = 1$ cm s^{-1}, $t_m = 3$ hr, for Cohasset (a, b), NEP 1 (c, d) and NEP 2 (e, f). At each height the M_2 tidal ellipse has been offset by the mean current at that height. For a) the ellipses are at $z = 1, 5, 9, 19, 40$ m, for c) $z = 1, 6, 12, 34, 69$ m, and for e) $z = 1, 6, 12, 37, 74$ m. The surface ellipses are shown as dashed lines. The currents rotate in the clockwise direction and the ellipses are marked at a common phase. The isolines of packet concentrations have units of packets per m^2.

- The horizontal dispersion rate on the Northeast Peak of Georges Bank is generally about an order of magnitude greater than on Sable Island Bank. The dramatic differences are due to the order of magnitude differences in u_* and hence significant differences in p and $\bar{z}$. Note however that the addition of other flow and stress components at Cohasset (other tidal constituents and wind waves) may reduce the contrast.

- The magnitude of the horizontal dispersion found here ($10 - 100$ m^2 s^{-1}) supports the importance of tidal-flow shear dispersion as a major mechanism in the benthic boundary layer on Georges Bank and Sable Island Bank.

The examples presented here use simplified model forcings in order to illustrate the underlying mechanisms. Model applications with more realistic forcings (e.g. additional flow components) and improved representations of the vertical mixing and the near-bottom ($z < 1$ m) region are planned.

Acknowledgements We thank Chris Naimie for providing the 3-d circulation model solutions, and Don Gordon for encouragement and support. This work was supported by the (Canadian) Federal Panel on Energy, Research and Development.

References

Cranford, P. J., and D. C. Gordon Jr. The influence of dilute clay suspensions on sea scallop (placopecten magellanicus) feeding activity and tissue growth. *Netherlands Journal of Sea Research*, 30:107–120, 1992.

Dyer, K. R. *Coastal and Estuarine Sediment Dynamics.* Wiley and Sons, 1986.

Gordon, D. C., P. J. Cranford, D. K. Muschenheim, J. W. Loder, P. D. Keizer and K. Kranck. Predicting the environmental impacts of drillings wastes on Georges Bank scallop populations. In P. M. Ryan, editor, *Managing the Environmental Impact of Offshore Oil Production*, pages 139–147. Canadian Society of Environmental Biologists, 1993.

Hannah, C. G., J. W. Loder, and Y. Shen. Shear dispersion in the benthic boundary layer. *The Proceedings of the ASCE 4th International Conference on Estuarine and Coastal Modelling* (San Diego, 26-28 October 1995) (submitted), 1995a.

Hannah, C. G., Y. Shen, J. W. Loder, and D. K. Muschenheim. `bblt`: Formulation and exploratory applications of a benthic boundary layer transport model. Can. Tech. Rep. Hydrog. Ocean Sci. No. xxx, 1995b.

Lynch, D. R., and C. E. Naimie. The M_2 tide and its residual on the outer banks of the Gulf of Maine. *J. Physical Oceanography*, 23:2222–2252, 1993.

Muschenheim, D. K., T. G. Milligan, and D. C. Gordon. New technology and suggested methodologies for monitoring particulate wastes discharged from offshore oil and gas drilling platforms and their effects on benthic boundary layer environment. Can. Tech. Rep. Fish. Aquat. Sci. No. xxx, 1995.

Naimie, C. E., J. W. Loder, and D. R. Lynch. Seasonal variation of the three-dimensional residual circulation on Georges Bank. *J. Geophysical Research*, 99:15,967–15,989, 1994.

van Rijn, L. C. *Principles of Sediment Transport in Rivers, Estuaries and Coastal Seas.* Aqua Publications, Amsterdam, 1993.

A case study of wave-current interaction in a strong tidal current

Diane Masson
Institute of Ocean Sciences
Sidney, B.C., Canada V8L 4B2

(Abstract only)

Abstract

During August 1991, a field program was carried out in the vicinity of Cape St. James, off the British Columbia coast, where a strong tidally driven flow interacts with an active wave climate. Surface current maps were obtained from a CODAR type HF radar (Seasonde) over an area of about 350 km^2 around the Cape. A series of Loran-C drifters were also deployed during the experiment, and used as ground truthing for the radar. A comparison between the drifter and the radar surface currents indicates a reasonable agreement.

Wave information was acquired with three Waverider buoys deployed around the Cape. A significant modulation of the wave properties at the tidal period was observed for the buoy located in the area where the currents are maximum. The tidally induced changes in the wave field are modelled with a local wave–current interaction model based on wave action conservation and on a high frequency limiting spectral shape. The model is applied on a period of 11 days for which the wind was relatively steady. The magnitude of the modeled tidal modulation of the wave field is of the same order of magnitude as the measurements, but in general underestimates the measured tidally induced changes. However, during the first half of the period, the modulation of the total wave energy is significantly out of phase with the buoy data. The effect of refraction by the current on the waves is assessed using a backward ray tracing method and two-dimensional surface current maps. It is proposed that refraction effects are important during the first part of the study period, and are a plausible cause for the phase discrepancy between the measurements and the results of the local model.

Comprehensive Finite Element Model for Continental Shelf Circulation

D.R. Lynch
Dartmouth College, Hanover, NH 03755, U.S.A.
email: d_r_lynch@dartmouth.edu

(Abstract only)

Abstract

Design and application of a full-featured 3-D finite element shelf model will be described. The model is fully nonlinear and baroclinic, with prognostic evolution of temperature and salt fields. Vertical mixing is represented by the Mellor-Yamada level 2.5 turbulence closure, with the Galperin adjustments. Horizontal exchanges utilize Smagorinsky closure. Time-domain integration incorporates all nonlinearities.

A case study in the Gulf of Maine illustrates model performance. The geographic coverage includes the Gulf, the Bay of Fundy, Georges and Browns Banks, and the Scotian Shelf. Several important nonlinear shelf processes are demonstrated including tidal rectification, frontal circulation, wind-induced mixing and circulation, and the generation of a coastal current. The adaptation and testing of radiation boundary conditions for finite element models will also be addressed.

Particular emphasis is placed on the circulation on and around Georges Bank, which separates the Gulf from the Northwest Atlantic at the shelf break. The role of seasonal baroclinicity in modulating the large-scale (order 100 km) circulation around the bank will be presented in relation to transport and retention of larval fish. Several interesting mechanisms of shear dispersion will be shown to account for bank-wide dispersal of nutrients and zooplankton. Finally, the role of small-scale (order 10 km) topography in generating important tidally-rectified currents on the bank top will be discussed.

Weakly Nonlinear Oscillatory Flow Over An Isolated Seamount

Jennifer Shore and Susan Allen
Dept. of Oceanography, Univ. of British Columbia, Vancouver, B.C., V6T 1Z4
jshore@ocgy.ubc.ca

Abstract. Results of a comparison of Foreman and Walter's 1992 numerical tidal model to a weakly nonlinear barotropic analytical solution of flow over a tall axisymmetric isolated seamount are presented. This presentation focusses on comparison of the residual currents because the nature of these currents is to enhance closed circulations around the seamount.

1 Introduction

In 1990, Foreman and Walters presented a finite element tidal model which had been developed for the southwest coast of Vancouver Island (FOREMAN and WALTERS, 1990). Model results were compared to tide gauge and current meter observations, focussing on M_2 and K_1 tidal amplitudes and current velocities. A further study (FOREMAN *et al.*, 1992) examined tidal residuals in the same region with the same model and with Lagrangian particle tracking techniques.

The results of the 1992 paper led us to an attempt to apply their model to a tall axisymmetric isolated topographic feature to study relationships between topographic geometry and residual flows. The Foreman and Walters' model was not specifically developed for tall isolated topography and, as such, it was felt that comparison of an analytical solution to a numerical one would be useful.

There have been many studies of flow around finite height topography. Analytical solutions to the linear case of trapped waves have been examined (LONGUET-HIGGINS, 1970; HUTHNANCE, 1974; HUNKINS, 1986) and quasi-geostrophic effects have been looked at both analytically and in the laboratory (VERRON, 1986; BOYER *et al.*, 1991).

Early numerical studies investigated Taylor Column formation and these studies evolved to include time-varying boundary conditions (some examples are HUPPERT and BRYAN, 1976; SMITH, 1992; CHAPMAN and HAIDVOGEL, 1992). Later numerical studies have looked at tidally rectified flow over simple and realistic topographies (eg. LYNCH and NAIMIE, 1993; BECKMANN and HAIDVOGEL, 1993; NAIMIE *et al.*, 1994).

2 The Numerical and Analytical Models

The Foreman and Walters' finite element numerical technique uses systems of elliptical equations generated by a harmonic decomposition of the shallow water equations (WALTERS, 1986). The grid consists of triangular elements with linear basis functions and was created with Henry's (1988) grid generating program. The model is described in detail in FOREMAN and WALTERS, 1990.

For the analytical part, barotropic oscillatory flow over an axisymmetric seamount is formulated with a weakly nonlinear analytic solution. The topography (*see* Fig. 1) used to formulate this solution was derived from similar linear studies (LONGUET-HIGGINS, 1970; HUTHNANCE, 1974; HUNKINS, 1986; CHAPMAN, 1989; SHEN, 1992) and is also used in the numerical model.

The boundary condition (imposed at a given radius, r_b; *see* Fig. 1) was chosen to be a standing wave centered over the seamount which allows the problem to be collapsed to a series of ODE's. Other boundary conditions would require solution of the full PDE's.

Amplitude and velocity solutions were assumed to be in the form of first and second order components and having first order solutions that would satisfy the linearized equations. For example, the expansion in cylindrical-polar co-ordinates for azimuthal velocity is an generalization of the following simpler expansion

$$u_\theta(r,\theta,t) = \sum_{i=1}^{n} a_i(r)\varepsilon^{i-1}(\cos(\phi_1)+\cos(\phi_2))^i$$

with $\varepsilon \ll 1$ and the phases (ϕ_1, ϕ_2) independent of r. Thus, for this case, the weakly nonlinear method

assumes the time-independent (residual) component to be second order.

3 Results

First and second order results of current velocities from the analytical and numerical models were compared and the results showed relative errors less than 4% for the first order components.

Upon investigating this relative error, an equation from the analytical model that relates a discontinuity in the slope of the first order velocity solution ($\frac{du_0}{dr}$) to the discontinuity in the topographical slope ($\frac{dh}{dr}$) was derived. Using the notation Δx to represent the discontinuity in x we find

$$\Delta\frac{du_0}{dr} = -\frac{u_0}{h}\Delta\frac{dh}{dr}.$$

Using this relation, a jump discontinuity in any of the second order variables can be written in terms of the discontinuity in the topographical slope. Therefore, a difference between the analytical and numerical solutions may be due to a relative error in the calculation of this slope.

As an additional result, it is possible to derive, using the ODEs, an expression for the residual azimuthal velocity which shows that this velocity is proportional to the aspect ratio, $\frac{h_d}{r_d}$ (*see* Fig. 1). This evidence could indicate that wider seamounts have weaker residual velocities than thinner ones for situations which fall within the limits of the assumptions of the analytical formulation.

Finally, Fig. 2 shows a comparison of the residual velocity field calculated from both the analytical and numerical models. The curves plot azimuthal velocity along a radial line out from the center of the seamount (dashed line in top view). The arrow shows direction of the current at that point. This figure is consistent with the notion that tidal rectification is expected to enhance anti-cyclonic circulation.

4 Summary and Conclusions

The Foreman and Walters finite element numerical tidal model has been used to predict residual flows around a tall isolated axisymmetric seamount. A weakly nonlinear analytical solution for barotropic flow over this topography was formulated so that a comparison between numerical and analytical solutions could be made.

The solutions were found to show reasonable agreement within the confines of the analytical formulation. Relative errors were found to arise from differences in the calculation of a discontinuity in the topographical slope. Further, the numerical model predicts residual currents which were consistent with tidal rectification theory.

References

BECKMANN, A. and D. B. HAIDVOGEL, 1993: Numerical simulation of flow around a tall isolated seamount. Part I: Problem Formulation and Model Accuracy. *J. Phys. Oceanogr.* **23**:1736–1753.

BOYER, D. L., G. C. D'HIERES, H. DIDELLE, J. VERRON, R.-R. CHEN, and L. TAO, 1991: Laboratory Simulation of Tidal Rectification over Seamounts: Homogenous Model. *J. Phys. Oceanogr.* **21**:1559–1579.

CHAPMAN, D. C. 1989: Enhanced subinertial diurnal tides over isolated topographic features. *Deep-Sea Res.* **36**:815–824.

CHAPMAN, D. C. and D. B. HAIDVOGEL, 1992: Formation of Taylor Caps over a tall isolated seamount in a stratified ocean. *Geophys. Astrophys. Fluid Dynam.* **64**:31–65.

FOREMAN, M. G. G., A. M. BAPISTA, and R. A. WALTERS, 1992: Tidal model studies of particle trajectories around a shallow coastal bank. *Atmosphere-Ocean* **30**:43–69.

FOREMAN, M. G. G. and R. A. WALTERS, 1990: A finite-element tidal model for the southwest coast of Vancouver Island. *Atmosphere-Ocean* **28**:261–287.

HENRY, R. F. 1988: Interactive design of irregular triangular grids. *Developments in Water Sciences, 35. Computational Methods in Water Resources* pages 445–450.

HUNKINS, K. 1986: Anomalous diurnal tidal currents on the Yermak Plateau. *J. Marine Res.* **44**:51–69.

HUPPERT, H. E. and K. BRYAN, 1976: Topographically generated eddies. *Deep Sea Res.* **23**:655–679.

HUTHNANCE, J. M. 1974: On the diurnal tidal currents over Rockall Bank. *Deep Sea Research* **21**:23–35.

LONGUET-HIGGINS, M. S. 1970: Steady currents induced by oscillations round islands. *J. Fluid Mech.* **42**:701–720.

LYNCH, D. R. and C. E. NAIMIE, 1993: The M_2 Tide and Its Residual on the Outer Banks of the Gulf of Maine. *J. Phys. Oceanogr.* **23**:2222–2253.

NAIMIE, C. E., J. W. LODER, and D. R. LYNCH, 1994: Seasonal variation of the three-dimensional residual circulation on Georges Bank. *J. Geophys. Res.* **99**:15 967–15 989.

SHEN, Y. 1992: Nonlinear Periodic Flow over Isolated Topography: Eulerian and Lagrangian Perspectives. Master's thesis Dalhousie University.

SMITH, L. T. 1992: Numerical Simulations of Stratified Rotating Flow over Finite Amplitude Topography. *J. Phys. Oceanogr.* **22**:686–696.

VERRON, J. 1986: Topographic Eddies in Temporally Varying Oceanic Flows. *Geophys. Astrophys. Fluid Dyn.* **35**:257–276.

WALTERS, R. A. 1986: A finite element model for tidal and residual ciculation. *Commun. Appl. Numer. Methods* **2**:393–398.

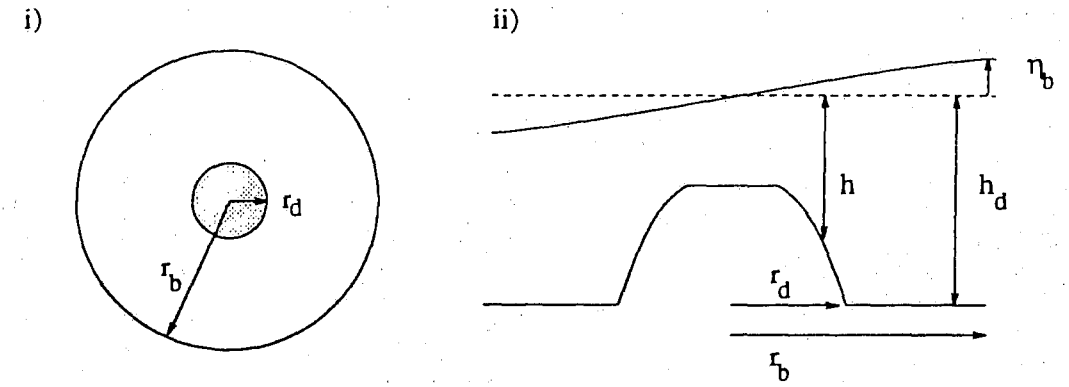

Figure 1: Topographical features used cylindrical-polar co-ordinates. i) Top view and ii) side view

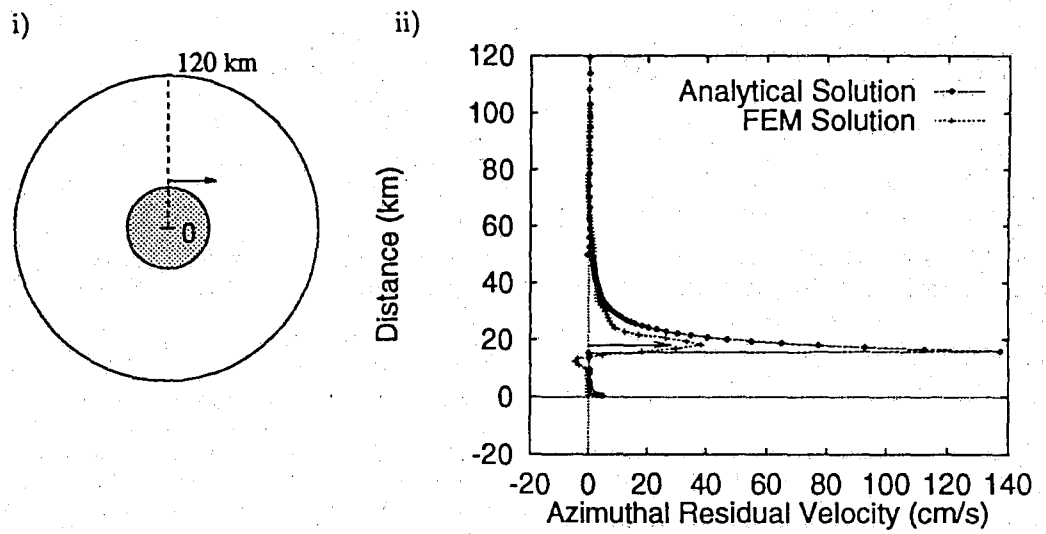

Figure 2: Azimuthal Residual Velocity. i) Top view of seamount. Dashed line indicates radius along which velocity results are plotted and the arrow indicates direction of flow. ii) Azimuthal velocity as it changes radially outwards from the center of the seamount (note radial distance is plotted along the y-axis and velocity magnitude along x). Predicted maximum velocity for the numerical model occurs at the same radius and in the same direction as the arrow.

A 3-D diagnostic model of the Labrador and Newfoundland shelves

Charles Tang, Quincy Gui and Ingrid Peterson
Bedford Institute of Oceanography
Ocean Sciences Division
Dartmouth, N.S., B2Y 4A2

A diagnostic model has been developed to study the mean circulation, wind driven currents, topographic waves and ice motion over the Labrador and Newfoundland shelves. The model domain is a rectangle encompassing the Labrador Sea and the Grand Bank. A Cartesian coordinate system with a grid size of 20 km is used in the computation. The density field is the seasonal mean density with a resolution of 1/6 degree compiled by DeYoung et al. (1994). The currents are forced by wind, atmospheric pressure and sea surface elevation at the northern and eastern boundaries.

To obtain the mean circulation, the northern sea surface elevation is tuned to produce a total southward transport (shelf, the Labrador Current and open ocean) of 35 Sv transport across the Hamilton Bank section. The results (fig.1) include many desired features of the shelf circulation, i.e., a strong Labrador Current, splitting of the the Labrador Current northeast of the Grand Banks, and a weak inshore branch of the Labrador Current, and give a transport of 12 Sv for the Labrador Current in agreement with previous estimates based on observations. The transport of the Labrador Current varies along the shelf edge. At the eastern side the the Hamilton Bank, a portion of the Labrador Current moves offshore into the central Labrador Sea, resulting in a decrease of the transport and velocity. It is shown that the variation of the transport of the Labrador Current is closely related to the density field and topography. A direct calculation of the JEBAR (joint effect of baroclinicity and relief) term of the momentum equation indicates that cross f/H transports of a spatial scale of 400 km appear along the Labrador Current. An onshore (offshore) transport gives an increased (a decreased) transport of the Labrador Current.

The seasonal change of the circulation is investigated using different seasonal density fields in the model calculations. In comparison with the summer circulation, the winter circulation is more barotropic, and follows the f/H contours more closely. The total southward transport across the Hamilton Bank section in winter is 20 Sv higher than that in summer. The large transport is attributed to the weak stratification and strong winds in winter.

To study the effects of density on the current structure, the currents are separated into a barotropic and a baroclinic component. The components across several east-west sections were calculated. The results show that the contribution of the barotropic/baroclinic currents to the total current differ from section to section. In the northern Labrador Sea, the current structure is characterized by a basin scale barotropic cyclonic gyre in the open ocean and a mixed barotropic-baroclinic coastal and Labrador Current over the shelf. In the southern Labrador Sea and the N.E. Newfoundland Shelf, the baroclinic and barotropic currents are equally important in the open ocean.

Several-day scale variability of the ocean current is primarily caused by winds. The model simulates both Ekman currents and gradient currents. The Ekman currents do not depend sensitively on the water depth and the distance to the coast. On the other hand, the gradient currents and the associated sea surface elevation are inversely proportional to the water depth and are enhanced in the coastal regions. Model runs were made using 6-hourly meteorological data (10 m wind and sea level barometric pressure) from the European Centre for Middle-range Weather Forecast. Fig.2 shows the 10 m wind (left panel), the barotropic current (middle panel) and the surface current (right panel) during a storm. A comparison of fig.2 with fig.1 shows that strong coastal currents are developed in the southern Labrador coast. Accompanying the coastal currents is a rise in the adjusted sea surface elevation (not shown).

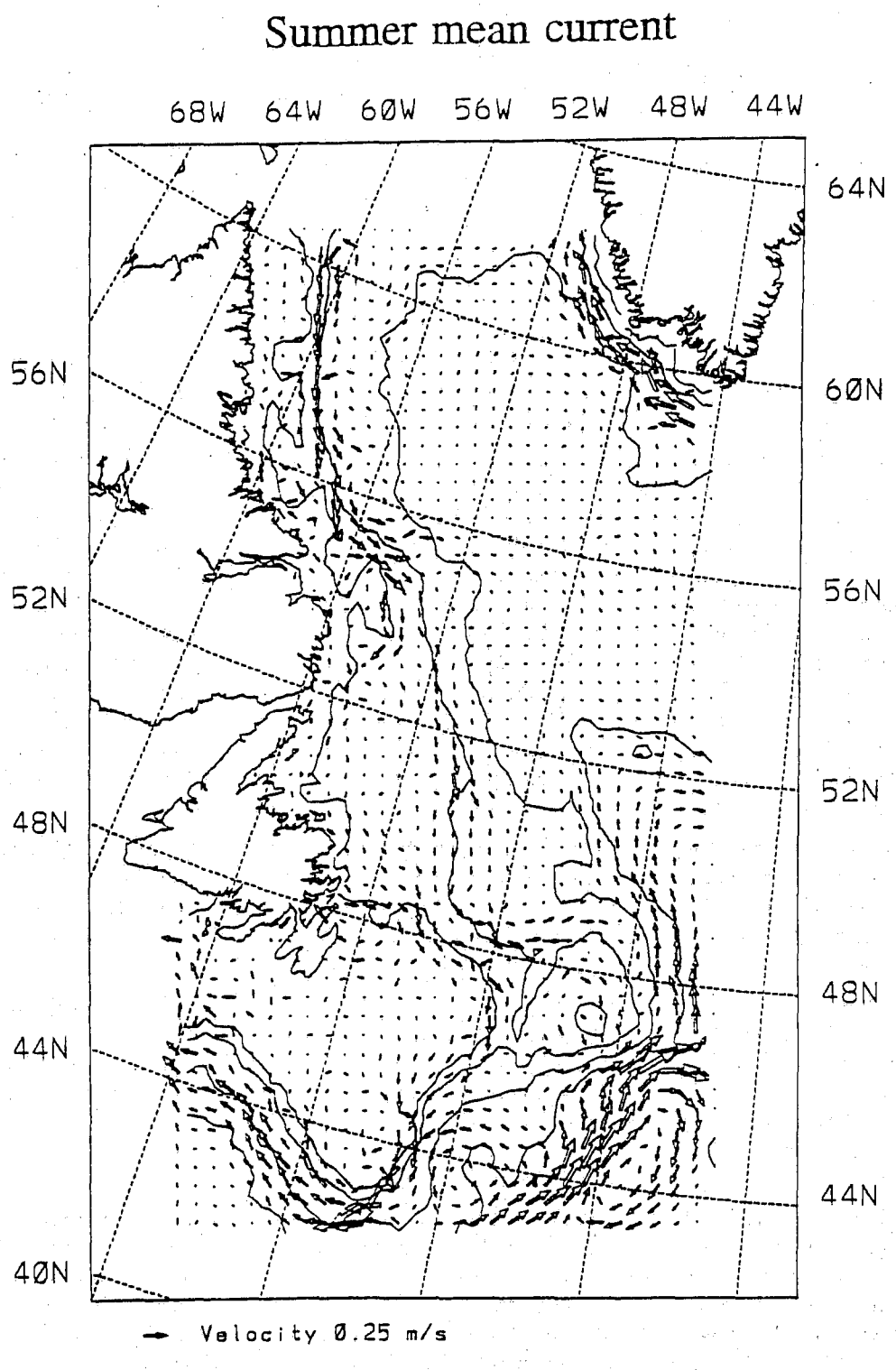

Figure 1: Mean barotropic currents for summer. The solid lines are 200 m, 1000 m and 3000 m isobaths.

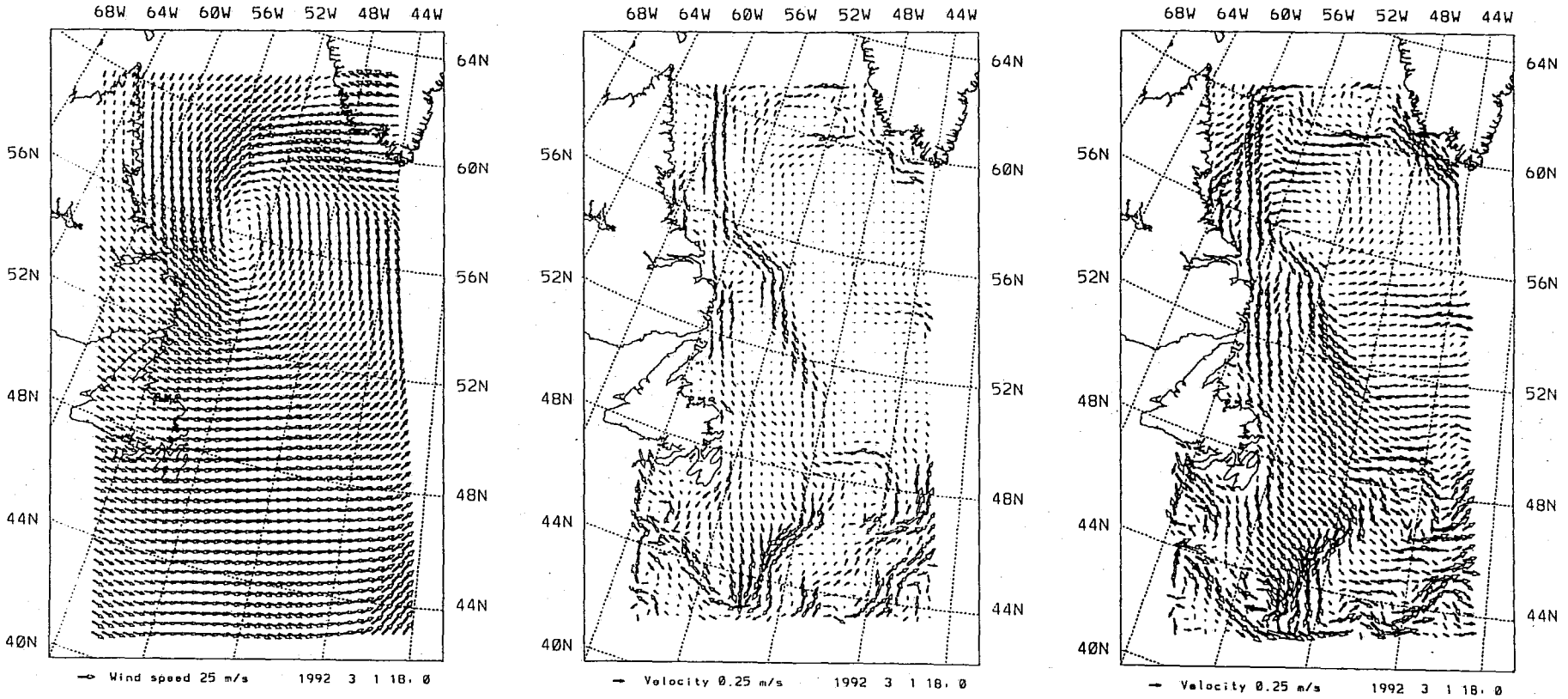

Figure 2: 10 m wind (left panel), barotropic circulation (middle panel), surface current (right panel) for 1800 UTC, 1 March, 1992.

The surface currents reflect the pattern of the wind field (note the centre of a surface eddy at (56N, 53W) corresponding to the centre of the storm). The influence of the permanent Labrador Current, the topography and the enhanced coastal currents on the surface currents is also evident. When the wind is in the offshore direction, the coastal effects are small and the dominant current is the Ekman current.

By calculating the individual terms of the momentum equation, the contributions due to the different forces can be compared. At the shelf edge, the dominate forces are the pressure gradient and the Coriolis force. In the shelf interior, the buoyancy effect and the wind stress are also important. The results suggest that correlation between winds and currents at the shelf edge is expected to be small although the variability is caused solely by the wind. In the shelf interior, a larger part of the currents are directly correlated to the wind stress.

Seasonal Baroclinic Circulation in the Scotia-Maine and Grand Bank Regions

Charles G. Hannah[1], David A. Greenberg[2], John W. Loder[2] and Zhigang Xu[2]

[1] Oceadyne Environmental, 373 Ridgevale Dr., Bedford, N.S., Canada B3A 4M2

[2] Department of Fisheries and Oceans, Bedford Institute of Oceanography, Dartmouth, N.S., Canada B2Y 4A2

1 INTRODUCTION

Three-dimensional numerical models for the climatological seasonal circulation in the Georges, Sable Island and Grand Bank regions are being implemented as part of the PERD Task 6B Environment Subprogram. Initial focus has been on the Georges Bank region as part of a coordinated set of physical, biological and sedimentological projects to aid the interpretation of field observations (e.g. Loder et al. 1993) and to assess the potential environmental impacts of hydrocarbon activity (Gordon et al. 1993; Hannah et al. 1995). The upstream Gulf of Maine and Scotian Shelf have been included in the model domain, both to represent important influences of the larger-scale shelf hydrodynamic regime and to support PERD-funded studies of drilling discharge distributions at the Cohasset-Panuke oil production site on Sable Island Bank (Muschenheim et al. 1995). An exploratory application of the model to the Grand Bank has also been initiated, with focus on baroclinic circulation in the Hibernia region.

The models, developed by and being implemented in association with U.S.A. collaborators at Dartmouth College and the University of North Carolina (e.g. Lynch et al. 1992; Lynch and Naimie 1993; Naimie and Lynch 1993; Lynch et al. 1995), use a triangular finite-element mesh which provides high spatial resolution in the bank areas of focus while including ambient regions at coarser scale. The models are being used both to obtain increased understanding of the circulation associated with tidal, wind, density and upstream forcing, and to provide composite seasonal-mean flow fields on realistic geometry for addressing applied issues. This presentation will highlight studies of the large-scale seasonal baroclinic circulation using historical density data and the harmonic diagnostic model of Naimie and Lynch (1993). These complement other flow-component studies such as those of tidal- and wind-driven circulation in the Gulf of Maine region (Lynch and Naimie 1993, Greenberg et al. 1995), and the more detailed studies of the seasonal variation in the composite circulation on Georges Bank (Naimie et al. 1994; Naimie 1995). These process-oriented studies provide important background to various model applications, such as the PERD environmental impacts issues and larval drift questions investigated as part of the Global Ocean Ecosystems Dynamics (GLOBEC) program (e.g. Werner et al. 1993; Tremblay et al. 1994; Lough et al. 1994).

2 METHODOLOGY

The baroclinic circulation studies are based on a historical database of concurrent temperature and salinity observations ("bottle" and CTD) from the Northwest Atlantic, assembled at the Bedford Institute from national archives and recent cruises. Climatological-mean density fields for selected seasons were estimated from the database using four-dimensional (x,y,z,t) optimal linear interpolation, with spatially-varying correlation scales chosen to represent topographically-induced anisotropy in the density fields (e.g. Loder et al. 1995). The winter and summer Scotia-Maine fields used here (Figure 1) were estimated on a mesh (gb3) extending along the shelf from Cabot Strait to Long Island, and about 100 km offshore from the shelf edge with a deep-ocean false bottom at about 1000 m (Hannah and Loder 1995). The summer Grand Bank field was estimated on a mesh (ns2) extending from Cape Bonavista to the Burin Peninsula, and about 100 km offshore from the shelf edge with a full-depth deep ocean (Figure 2), with similar correlation scales to those in Hannah and Loder (1995).

The three-dimensional baroclinic circulation driven by these fields was obtained using the linear harmonic diagnostic model of Naimie and Lynch (1993), with 21 variably-spaced vertical nodes pro-

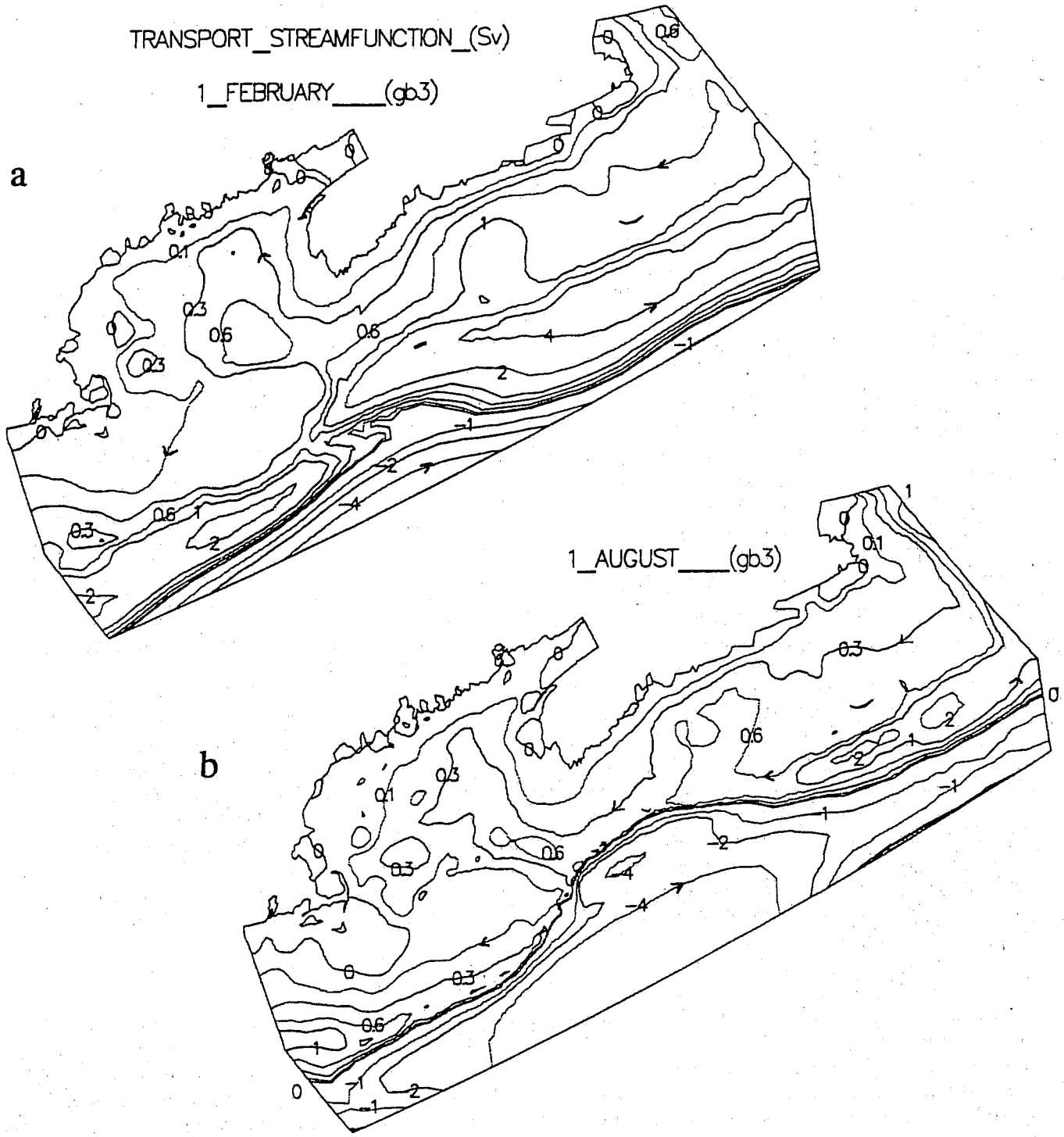

Figure 1: Transport streamlines for the depth-integrated baroclinic circulation in the Scotia-Maine region in a) winter and b) summer (from Hannah and Loder 1995). The streamline value at the coast is zero.

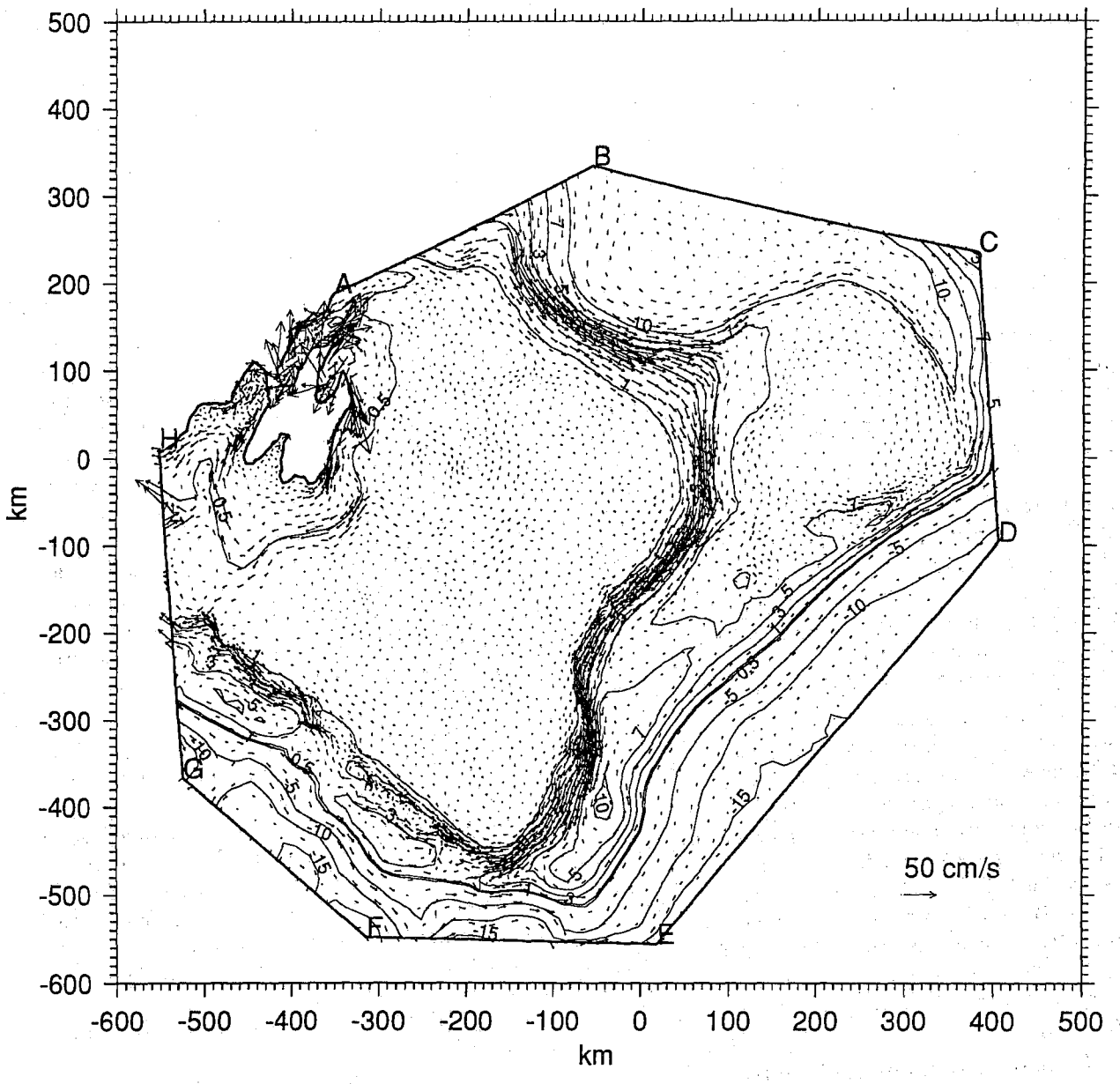

Figure 2: Depth-averaged currents and transport streamlines (in Sv) for the summer circulation in the Grand Banks region associated with the baroclinic pressure field and barotropic (Labrador Current) inflow across the northern boundary. The streamline value at the coast is zero.

viding resolution of surface and bottom Ekman layers. Baroclinic pressure gradients computed from the estimated density fields were specified as model forcings, together with elevations specified on open boundaries except for the use of a geostrophic flow condition on downstream (in the sense of coastal-trapped wave propagation) boundaries. In the Scotia-Maine solutions, the boundary elevations were specified to provide zero geostrophic flow at the seafloor, thereby excluding barotropic inflow from upstream. In the Grand Bank solution, the same boundary elevation strategy was used, except that an additional setup was specified on the northern upstream boundary based on moored current measurements, corresponding to a transport of 11.8 Sv for the barotropic component of the Labrador Current over the shelf and upper/mid slope.

3 EXAMPLE RESULTS

The primary features of the climatological seasonal baroclinic circulation in the Scotia-Maine region are illustrated by the depth-integrated transport streamlines (Figure 1) from the model solutions for winter and summer. The model solutions for all seasons have the broad-scale features of southwestward flow over the shelf, northeastward flow near the offshore boundary where there are Gulf Stream influences, and cyclonic circulation over the continental slope, but with substantial variations with season (see Hannah and Loder 1995 and Loder et al. 1995 for more detail). The along-shelf flow is strongest in winter, with magnitude and seasonal changes similar to transport estimates from moored current measurements. The slope circulation is more variable, and its reliability less clear in view of the sparser off-shelf density data. There are pronounced topographic influences superimposed on the large-scale throughflow on the shelf, with cyclonic flow tendencies around deep basins, and anticyclonic circulation tendencies around major banks such as Sable Island and Georges. These flow components together with other forcings such as tidal rectification on Georges Bank are major factors to the occurrence of bank-scale gyres, and hence emphasize the importance of proper representation of the broader-scale shelf regime in developing bank circulation models for various applications.

Model solutions for the Grand Bank region show qualitative similarity to those for the Scotia-Maine region in having equatorward shelf flow and generally northeastward flow offshore, but there are notable differences. The equatorward transports are generally larger (5-10 Sv) and concentrated near the shelf edge, include a significant barotropic component as specified here through the upstream boundary elevation, and have a smaller relative variation with season. The flow pattern is illustrated by the summer solution (Figure 2) which shows the shelf-edge "traditional" Labrador Current being "turned" offshore by the baroclinic pressure field, particularly north and south of Flemish Cap, and near the Tail of the Grand Bank. This pattern shows encouraging agreement with moored and surface drifter data, and indicates that the historical density database in this region, too, is adequate for useful diagnostic model studies of the circulation. Furthermore, the fine model mesh and anisotropic density-field correlation scales used here result in a realistic representation of the strong and narrow Labrador Current along the shelf edge.

These solutions illustrate both the significance of the baroclinic flow component to seasonal circulation on the northwestern Atlantic shelf, and the potential of the historical hydrographic database and high-resolution numerical models for obtaining realistic representations of the flow fields. The present diagnostic solutions also include smaller-scale flow features of uncertain reliability, probably associated with inadequate local density data. These point to the need for prognostic numerical models (e.g. Lynch et al. 1995; Naimie 1995) to refine the density and flow fields into full dynamic consistency as a next step in the development of reliable shelf circulation models for PERD applications.

Acknowledgements We are grateful to colleagues in our PERD and GLOBEC studies, and others at the Bedford Institute for providing models, data and other input, and to the PERD and US GLOBEC programs for support.

REFERENCES

Gordon, D. C., P. J. Cranford, D. K. Muschenheim, J. W. Loder, P. D. Keizer and K. Kranck. Predicting the environmental impacts of drillings wastes on Georges Bank scallop populations. In P. M. Ryan, editor, *Managing the Environmental Impact of Offshore Oil Production*, pages 139–147. Canadian Society of Environmental Biologists, 1993.

Greenberg, D. A., J. W. Loder, Y. Shen and D. R. Lynch. Spatial and temporal structure of the barotropic response of the Scotian Shelf and Gulf of Maine to surface wind stress. *J. Geophysical Research* (submitted), 1995.

Hannah, C. G., and J. W. Loder. Seasonal Variation of the Baroclinic Circulation in the Scotia-Maine Region. *Proceedings of the 7th Biennial Conference on the Physics of Estuaries and Coastal Seas* (Woods Hole, Mass.; 28-30 November 1994) (submitted), 1995.

Hannah, C. G., Y. Shen, J. W. Loder, and D. K. Muschenheim. `bblt`: Formulation and exploratory applications of a benthic boundary layer transport model. Can. Tech. Rep. Hydrog. Ocean Sci. No. xxx, 1995.

Loder, J. W., K. F. Drinkwater, N. S. Oakey and E. P. W. Horne. Circulation, hydrographic structure and mixing at tidal fronts: the view from Georges Bank. *Phil. Trans. R. Soc. Lond., Ser. A 343*, 447–460, 1993.

Loder, J. W., G. Han, C. G. Hannah, D. A. Greenberg, and P. C. Smith. Hydrography and baroclinic circulation in the Scotian Shelf region: summer and winter. *Can. J. Fish. Aquat. Sci. Suppl.* (submitted), 1995.

Lough, R. G., W. G. Smith, F. E. Werner, J. W. Loder, F. H. Page, C. G. Hannah, C. E. Naimie, R. I. Perry, M. Sinclair, and D. R. Lynch. The influence of wind-driven advection on the interannual variability in cod egg and larval distributions on Georges Bank: 1982 vs 1985, *ICES Mar. Sci. Symp., (1993 Symposium on Cod and Climate Change)*, 198, 356–378, 1994.

Lynch, D. R., J. T. C. Ip, C. E. Naimie, and F. E. Werner. Comprehensive coastal circulation model with application to the Gulf of Maine, *Continental Shelf Res.* (in press), 1995.

Lynch, D. R., and C. E. Naimie. The M_2 tide and its residual on the outer banks of the Gulf of Maine. *J. Physical Oceanography, 23*, 2222–2252, 1993.

Lynch, D. R., F. E. Werner, D. A. Greenberg, and J. W. Loder, Diagnostic model for baroclinic, wind-driven and tidal circulation in shallow seas, *Continental Shelf Res., 12*, 37–64, 1992.

Muschenheim, D. K., T. G. Milligan, and D. C. Gordon. New technology and suggested methodologies for monitoring particulate wastes discharged from offshore oil and gas drilling platforms and their effects on benthic boundary layer environment. Can. Tech. Rep. Fish. Aquat. Sci. No. xxx, 1995.

Naimie, C. E. Georges Bank residual circulation during weak and strong stratification periods – prognostic numerical model results, *J. Geophysical Research* (submitted), 1995.

Naimie, C. E., J. W. Loder, and D. R. Lynch. Seasonal variation of the three-dimensional residual circulation on Georges Bank. *J. Geophysical Research, 99*, 15,967–15,989, 1994.

Naimie, C. E., and D. R. Lynch. Fundy5 Users' Manual, Numerical Methods Laboratory, Dartmouth College, Hanover, N.H., 1993.

Tremblay, M. J., J. W. Loder, F. E. Werner, C. E. Naimie, F. H. Page, and M. M. Sinclair. Drift of sea scallop larvae *placopecten magellanicus* on Georges Bank: a model study of the roles of mean advection, larval behaviour and larval origin, *Deep-Sea Research II, 41*, 7–49, 1994.

Werner, F. E., F. H. Page, D. R. Lynch, J. W. Loder, R. G. Lough, R. I. Perry, D. A. Greenberg, and M. M. Sinclair. Influences of mean advection and simple behavior on the distribution of cod and haddock early life stages on Georges Bank, *Fisheries Oceanography, 2*, 43–64, 1993.